Joint atmospheric-terrestrial water cycle and land-atmosphere interactions in complex terrain: Fully coupled modeling for the Heihe River Basin, China

Dissertation zur Erlangung des Doktorgrades an der
Fakultät für Angewandte Informatik der
Universität Augsburg

vorgelegt von

M.Sc. Zhenyu Zhang

2019

Erstes Gutachten:	Prof. Dr. Harald Kunstmann
Zweites Gutachten:	Prof. Dr. Wolfgang Buermann

Tag der mündlichen Prüfung: 27.10.2020

Acknowledgements

First and foremost, I would like to express my gratitude to my supervisor Prof. Dr. Harald Kunstmann for his expert guidance and support throughout this Ph.D. work. I deeply appreciate all the encouragement, discussions and opportunities he provided, which have expanded my knowledge and skills, and are quite promoting to my future research. I feel very grateful to Dr. Joël Arnault, who gave me generous advice and help. I really appreciate that he was always available for discussing and answering my questions. I wish to express my special gratefulness to Dr. Patrick Laux and Dr. Sven Wagner for their kindness. They have always been supportive and advised me with many valuable suggestions.

I would like to thank Prof. Dr. Wolfgang Buermann and Prof. Dr. Peter Fiener for their kind agreement to be the second and third referees in my dissertation committee.

Many thanks to the bunch of colleagues in the working group: Drs. Jianhui Wei, Ganquan Mao, Diarra Dieng, Thinh Dang, Noah Kerandi, Benjamin Fersch, Thomas Rummler, Mohsen Soltan, Cornelius Hald, Tanja Portele, Julius Polz, Maurus Borne, Verena Wedler and all the other friends in KIT/IMK-IFU for their generous help.

Furthermore, I am grateful for the computer technical advice and support from Dr. Dominikus Heinzeller and Frank Neidl.

This Ph.D. study is financially supported by the China Scholarship Council and KIT Fellowship. The simulations were conducted at SuperMUC in Leibniz Supercomputing Center (LRZ) and the High-Performance Computer in KIT/IMK-IFU.

Last but not least, I would like to thank my family for their endless support, especially my wife Yang for her understanding and patience over these years.

Abstract

Regional climate modeling integrating the water, energy and mass exchange at and between the subsurface, land surface and atmosphere provides a useful tool to investigate the regional water cycle and land-atmosphere interactions. Current regional climate modeling frameworks focus on the description of sophisticated terrestrial hydrological processes, such as lateral terrestrial water flow. However, the effect of the complexity of terrestrial hydrological processes to atmospheric modeling is not fully understood in all its details yet. This dissertation contributes to the improved understanding of the joint terrestrial and atmospheric water balance and land-atmosphere interactions in mountainous areas.

The application region is the Heihe River basin (HRB), an endorheic basin located in northwest China, which is characterized with complex terrain and heterogeneous natural features. The human activities in this area suffer from water-stress related issues, which requires the proper knowledge of the regional water balance. For this purpose, the Weather Research and Forecasting (WRF) model and its hydrological modeling extension package WRF-Hydro are applied for the case of the HRB. The atmospheric modeling is configured at convection permitting scale 3 km, and the additional lateral terrestrial water processes with WRF-Hydro are resolved at 300 m fine hydrological sub-grid. The effect of lateral terrestrial water flow on regional climate modeling is investigated by comparing the model simulations results with and without this hydrological extension coupling for the period 2008-2010, and is quantified with a joint atmospheric-terrestrial water budget analysis, a regional precipitation recycling analysis and a fully three-dimensional atmospheric moisture tracing method (evaporation tagging). The coupled modeling system WRF-Hydro simulates near-surface hydrometeorological variability similar to the standard WRF model and demonstrates, in addition, its ability to reproduce daily streamflow. In the fully coupled mode, as a consequence of lateral terrestrial water flow description, the redistribution of infiltration excesses in the mountainous area produces higher soil moisture content in the root zone, increases the terrestrial water storage and evapotranspiration and decreases the total runoff. The resulting wetting and cooling in the near-surface affect the regional climate by changing the regional water vapor transports and water vapor content, while, in turn, inducing precipitation differences. Overall, the fully coupled modeling increases the recycling rate, indicating that lateral terrestrial water flow influences regional climate in the study area.

Zusammenfassung

Die regionale Klimamodellierung, die den Wasser-, Energie- und Stoffaustausch an und zwischen dem Untergrund, der Landoberfläche und der Atmosphäre umfasst, ist ein zentrales Instrument, um die Wechselwirkungen zwischen Land und Atmosphäre zu untersuchen. Die regionale Klimamodellierung konzentriert sich aktuell auf die verbesserte Beschreibung hydrologischer Prozesse, wie z.B. des lateralen terrestrischen Wasserflusses. Die Auswirkung der Komplexität terrestrischer hydrologischer Prozesse auf die atmosphärische Modellierung ist jedoch noch nicht in allen Details vollständig verstanden. Diese Dissertation trägt zum besseren Verständnis des gemeinsamen terrestrischen und atmosphärischen Wasserhaushalts und der Wechselwirkungen zwischen Land und Atmosphäre, insbesondere in Berggebieten bei.

Anwendungsgebiet ist das Heihe-Flussbecken (HRB), ein endorheisches Becken im Nordwesten Chinas, das sich durch komplexes Gelände und heterogene Landoberflächenmerkmale auszeichnet. Die menschlichen Aktivitäten sind dort aufgrund der geringen Wasserverfügbarkeit limitiert, was ein besseres Verständnis des regionalen Wasserhaushalts unabdinglich macht. Zu diesem Zweck wird das regionale Klimamodell Weather Research and Forecasting (WRF) verwendet, sowie das hydrologisches Erweiterungspaket WRF-Hydro. Die Atmosphäre ist mit 3 km horizontaler Gitterauflösung konvektionsauflösend gerechnet, die zusätzlichen lateralen terrestrischen Wasserprozesse mit WRF-Hydro sind mit 300 m Auflösung beschrieben. Der Einfluss des lateralen terrestrischen Wasserflusses auf die regionale Klimamodellierung wird durch den Vergleich der Modellsimulationsergebnisse mit und ohne hydrologische Kopplung für den Zeitraum 2008-2010 analysiert und mit einer gemeinsamen atmosphärisch-terrestrischen Wasserhaushaltsbilanzierung, einer Analyse des regionalen Niederschlagsrecyclings, und einer vollständig dreidimensionalen Luftfeuchteverfolgungsmethode (Evaporation Tagging) quantifiziert. Das gekoppelte Modellsystem WRF-Hydro simuliert oberflächennahe hydrometeorologische Variabilität, ähnlich dem Standard-WRF-Modell, und demonstriert darüber hinaus die wichtige Fähigkeit, den täglichen Abfluss im Gerinne zu reproduzieren. Im voll-gekoppelten Modus führt die Umverteilung von Infiltrationsüberschüssen in den Berggebieten infolge der verbesserten Beschreibung der lateralen terrestrischen Wasserflüsse zu einem höheren Bodenfeuchtegehalt in der Wurzelzone, erhöht die terrestrische Wasserspeicherung und Evapotranspiration und verringert den

Gesamtabfluss. Die daraus resultierende Benetzung und Abkühlung im oberflächennahen Bereich beeinflusst das regionale Klima, indem sie den regionalen Wasserdampftransport und den Wasserdampfgehalt verändert und damit Niederschlagsunterschiede hervorruft. Insgesamt erhöht die vollständig gekoppelte Modellierung die Recyclingrate und zeigt, dass die lateralen terrestrischen Wasserflüsse das regionale Klima im Untersuchungsgebiet beeinflussen.

Contents

List of Figures

List of Tables

List of Abbreviations

ACM2	Asymmetric Convective Model version 2
ARW	Advanced research dynamics WRF
AWB	Atmospheric water balance
CCI	Climate Change Initiative
CMA	China Meteorological Administration
CMFD	China Meteorological Forcing Dataset
COSMO	Consortium for Small-Scale Modeling
DHSVM	Distributed hydrology-soil-vegetation model
ECMWF	European Centre for Medium-Range Weather Forecasts
EC	Eddy-covariance
ESA	European Space Agency
GCM	General Circulation Model
GLEAM	Global Land Evaporation: Amsterdam Model dataset
HRB	Heihe River Basin
HRLDAS	High Resolution Land Data Assimilation System
HMS	Hydrologic Model System
HWSD	Harmonized World Soil Database
KGE	Kling-Gupta efficiency
LSM	Land Surface Model
MM5	The Fifth-Generation NCAR Mesoscale Model
MTE	Model tree ensemble
MYJ	Mellor-Yamada-Janjic scheme
NASA	National Aeronautics and Space Administration
NCAR	National Center for for Atmospheric Research
NCEP	National Centers for Environmental Prediction
Noah-LSM	Noah Land Surface Model
NSE	Nash-Sutcliffe efficiency
NWP	Numerical Weather Prediction

PBIAS	Percent bias
PBL	Planetary Boundary Layer
RCM	Regional Climate Model
RMSE	Root mean square error
RRTM	Rapid radiative transfer model
SWC	Soil water content
TRMM	Tropical Rainfall Measuring Mission data
TWB	Terrestrial water balance
TWS	Terrestrial water storage
WRF	Weather Research and Forecasting modeling system
WSM6	WRF Single-Moment 6-class
YSU	Yonsei University scheme

List of Symbols

ET	[mm]	total evapotranspiration
ET_{tag}	[mm]	tagged evapotranspiration
G	[$W \cdot m^{-2}$]	ground heat flux
H	[$W \cdot m^{-2}$]	sensible heat flux
P	[mm]	total precipitation
P_{tag}	[mm]	tagged precipitation
Q_{in}	[mm]	lateral inflow of atmospheric moisture
Q_{out}	[mm]	lateral outflow of atmospheric moisture
R	[mm]	total runoff
Rn	[$W \cdot m^{-2}$]	net radiation flux
S	[mm]	terrestrial water storage
T	[°C]	temperature
W	[mm]	atmospheric water storage
$q_{v/c/i/r/s/g}$	[$kg \cdot kg^{-1}$]	mixing ratio of water vapor, cloud water, ice, rain, snow and graupel
$q_{n,tag}$	[$kg \cdot kg^{-1}$]	tagged mixing ratio of moisture species
t	[$s/h/d$]	time
$\mathbf{v}$	[$m \cdot s^{-1}$]	three dimensional vector velocity
z	[m]	vertical coordinate / depth
$-\nabla \cdot \vec{Q}$	[mm]	atmospheric moisture convergence
β	[-]	precipitation recycling rate
θ	[$m^3 \cdot m^{-3}$]	soil water content
λE	[$W \cdot m^{-2}$]	latent heat flux
ν	[$m^2 \cdot s^{-1}$]	kinematic molecular viscosity
$\rho_{d/v/H}$	[$kg \cdot m^{-3}$]	density of dry air, water vapor and hydrometeors
χ	[-]	precipitation efficiency

1 Introduction

1.1 Background and motivation

1.1.1 Fully coupled atmospheric-hydrological modeling

Understanding the hydrological cycle between the atmosphere and the land surface in a mesoscale river basin is essential for the local environmental conditions and human development (Milly et al., 2005; Yeh and Famiglietti, 2008). Since land surface models (LSMs) and hydrological models are flawed by insufficient observational meteorological driving data, regional climate models (RCMs) are increasingly used for conducting regional hydrological studies (Graham et al., 2007; Powers et al., 2017). It is beneficial that RCMs not only allow to describe the state of the atmosphere at a higher temporal-spatial resolution, but also consider the moisture feedback from the surface soil layer to the atmospheric layer, which could affect atmospheric boundary layer dynamics through thermal exchanges. With the direct two-way interactions between the underlying land surface and the atmosphere, a large body of studies examined the impact of different land surface parameterization schemes for weather forecasting and climate modeling, including the evaluation of land use change drivers such as urbanization, deforestation, and anthropogenic water use intervention such as irrigation and water transfer projects (Cao et al., 2015; Chen and Xie, 2010; Pei et al., 2016). A large body of studies also focused on distinguishing the impacts of these land surface changes on the water balance from local to regional scales (Deng et al., 2015; Erlandsen et al., 2017).

More and more studies have indicated that the physical processes and parameterizations in the land surface have a noticeable influence on the lower atmosphere such as near-surface soil moisture, temperature, and could thus further affect the atmospheric modeling (Fan et al., 2007; Gao et al., 2008; Santanello et al., 2013). This shows that land surface processes impact on the regional hydrological cycle in both terrestrial and

atmospheric compartments. Besides, with the increase of computational resources in high-resolution Earth System Models, the role of land surface spatial variability on modeling results is more and more emphasized (Buermann et al., 2001; Clark et al., 2015; Gao et al., 2008). Current RCMs, describing only the vertical hydrological processes in the land surface and subsurface and even rarely groundwater dynamics (Barlage et al., 2015; Yuan et al., 2008), have a limited capability in representing the terrestrial water dynamics and cycle. Neglecting lateral water movement and the subsequent re-infiltration and exfiltration processes may lead to errors in the representation of the surface hydrologic conditions and spatial variability in RCMs, in particular for complex terrain and moisture gradient featured areas (Senatore et al., 2015). Therefore, increasing the complexity of hydrological modeling options within atmospheric models, as well as improving our understanding of the impacts of these hydrological processes, is highly relevant for the Earth System Model community.

Several studies have considered lateral terrestrial water processes with atmospheric modeling at regional scale. In an early attempt, the water flow concentration scheme in the distributed hydrology-soil-vegetation model (DHSVM) was introduced in the Mesoscale Model version 5 (MM5) by Gao et al. (2004). Later on, Gao et al. (2006) further took into account the pond water evaporation and reinfiltration, as well as surface and subsurface routing processes in the Noah land surface scheme within the MM5 atmospheric model. Both applications were performed in the upper reaches of the Heihe River Basin (HRB) for two summer rainfall events. Terrestrial water flow concentration processes could redistribute the grid surface runoff amount according to the description of slope direction (Gao et al., 2004). Gao et al. (2006) further indicated that a large extent of atmospheric fields was influenced by laterally moved terrestrial water. Subsequently, Maxwell et al. (2007) coupled the parallel hydrology model ParFlow to the Advanced Regional Prediction System (Xue et al., 2000) in a series of idealized cases with different soil moisture initialization. They found that the fully coupled model maintained a realistic topographically-driven soil moisture distribution that could not be obtained with the stand-alone atmospheric model. Later, Maxwell et al. (2011) combined ParFlow and the Weather Research and Forecasting (WRF) model (Skamarock and Klemp, 2008), and demonstrated that the coupled model could explicitly simulate the water storage and runoff. Recently, Shrestha et al. (2014) presented a modular and scale-consistent Terrestrial Systems Modeling Platform (TerrSysMP), which consists of the Consortium for Small-Scale Modeling (COSMO) atmospheric model (Baldauf et al., 2011), the National Center

for Atmospheric Research (NCAR) Community Land Model (Oleson et al., 2008) and the ParFlow model. Within a one-week simulation carried for the Rur catchment in Germany, Shrestha et al. (2014) found a strong sensitivity of the model results to the initial soil moisture conditions, and showed that the coupled model slightly improves the predictions of surface fluxes. Butts et al. (2014) and Larsen et al. (2016) dynamically linked the HIRHAM RCM with the hydrological model MIKE-SHE, and applied it to the Skjern River catchment in Denmark, focusing on data transfer interval between the atmosphere and hydrological models. They suggested that coupled modeling had a potential for improving climate projections. In a larger scale, Wagner et al. (2016) coupled WRF and the Hydrologic Model System (HMS) (Yu et al., 2006) for an 8-year fully coupled simulation in the Poyang Lake region in southeast China, and showed that the groundwater dynamics had a significant impact on the regional water balance.

A hydrological enhancement system called WRF-Hydro (Gochis et al., 2015), developed as an extension package for WRF, has been used in fully coupled atmosphere-hydrology studies. Senatore et al. (2015) used the coupled WRF-Hydro model over the Crati River basin in southern Italy, and found that the resolved lateral flow changed the precipitation modestly, while increasing the soil moisture and drainage and decreased surface runoff. Contrarily, using a joint atmospheric-terrestrial water balance analysis for the upper Tana River basin of East Africa, Kerandi et al. (2018) reported that the coupled WRF-Hydro slightly reduced soil water storage, evapotranspiration and precipitation, but increased the runoff. Rummler et al. (2019) implemented the coupled WRF-Hydro over a wetter region covering Southern Germany and Eastern Alps in the summer time, and found that the lateral terrestrial water flow increased evapotranspiration and decreased the percolation and total runoff. In West Africa, Arnault et al. (2016b) found that the impact of overland lateral flow and runoff-infiltration partitioning on precipitation was reduced when increasing the size of the analyzed area. In addition, Givati et al. (2016) used the coupled WRF-Hydro model in central Israel for flood prediction and suggested that the fully coupled model has the potential to improve precipitation and early flood warning forecasting.

All above studies showed that considering the lateral terrestrial water flow in atmospheric models has an impact on simulated precipitation and other hydrological variables, and that it allows to reproduce observed streamflow with different levels of skills. However, the impact of lateral terrestrial water flow in the above regions were

not fully consistent. In order to better understand the variety of lateral terrestrial water flow effects, the fully coupled atmospheric-hydrological modeling systems still needs to be extensively experimented for regions with various climatic and hydrological conditions.

Northwestern China is one of the most water-deficient areas in the world. Located in the center of this arid area, the Heihe River Basin (HRB) is the second-largest inland watershed of China. Influenced by complex topography, diversified landscape, and atmospheric circulation, the HRB is characterized by significant spatiotemporal heterogeneity of precipitation and evapotranspiration, and especially suffers from water shortage challenges for agricultural production, economic development and ecosystem sustainability (Cheng et al., 2014). For these reasons, water-stress-related studies, as well as the associated atmospheric, hydrological and ecosystem studies have been extensively carried on in this representative basin (Li et al., 2013). Recent modeling studies have shown that RCMs are able to simulate reasonably well the spatial patterns of precipitation and precipitation-elevation gradients among the mountainous areas of the HRB (Li et al., 2018a; Pan et al., 2014; Wang et al., 2017). Some researches confirmed that different land surface parameterizations in the HRB have an impact on modeled atmospheric variables. For example, Gao et al. (2008) and Meng et al. (2009) found that improvement in land surface information data could further improve the simulation of near-surface fields by the use of MM5 in combination with Noah-LSM. Deng et al. (2015) found that land use and land cover changes can induce a remarkable change on the surface energy and regional water balance in WRF. With regard to the warm bias over the plain area in HRB in RCMs, Zhang et al. (2017) coupled an anthropogenic irrigation scheme with WRF. They showed a cooling and wetting effect over the irrigation area, and concluded that the irrigation-related increase of water vapor may induce moisture convergence change and enhance the precipitation remotely.

When addressing the improved representation of the water cycle at the regional scale, it is relevant to see how hydrologically-enhanced atmospheric models can simulate the water budget in a water-limited and hydrologically heterogeneous inland river basin such as the HRB. It is the fully coupled modeling approach that allows to study the impact of lateral terrestrial water flow description on land surface and land-atmosphere interactions. In this study, the effect of the lateral terrestrial water flow on the regional water cycle and land-atmosphere interactions in a complex terrain

and water-limited region is assessed. For this purpose, the fully coupled hydrological-atmospheric modeling system WRF-Hydro model is selected and applied to the HRB for a 3-year simulation period, and the simulation results are compared with those from the stand-alone WRF model. The focus is on the analysis of the water cycle differences between coupled WRF-Hydro and WRF with a joint atmospheric-terrestrial water budget, especially in the upper HRB where most of the water is produced. Differences in land-atmosphere interactions between WRF and WRF-Hydro are further quantified with both a bulk type precipitation recycling analysis (e.g., Eltahir and Bras, 1996; Van Der Ent and Savenije, 2011) and a fully three-dimensional atmospheric moisture tracing method (e.g., Arnault et al., 2016a, 2019; Wei et al., 2015).

1.1.2 Climatic and hydrological characteristics of Heihe River Basin in Northwest China

The Heihe River Basin (HRB) covers a 143,200 km^2 area in the northwest of China and it stretches from the Qilian Mountains in the south, as part of the Tibetan Plateau, to the Gobi Desert between China and Mongolia in the north, with an elevation ranging from approx. 5,500 m to 1,000 m (Li et al., 2013). The HRB stretches from 37.7° N to 42.7° N and from 97.1° E to 102.0° E, and it is situated at the edge of the continental monsoon climate zone (Figure 1.1). Accordingly, the precipitation varies among the seasons, and more than 80% of annual precipitation occurs during the wet season spanning from May to September (Pan et al., 2014). Based on the terrain and landscape characteristics, HRB is featured by heterogeneous natural conditions and hydrological states. The upper reaches of HRB are dominated by high mountains and deep gorges, with the landscape of frozen soil, alpine meadow and forest. The annual temperature is between -3 and 3 ℃ and precipitation between 200 and 600 mm, with high spatial and seasonal variabilities. The middle reaches of HRB are comparably flat, with a mean temperature between 6 and 8 ℃ and annual precipitation between 100 and 250 mm. Streamflow and groundwater in this area are largely used for irrigation of oasis agriculture. The Heihe river ends at Juyan Lake in lower reaches, where most of the land is covered by sand and gravel deserts, with small numbers of riparian wetlands. The ecological environment in the lower reaches is very fragile, and climate is extremely dry, less than 50 mm precipitation and more than 3000 mm potential evaporation per year.

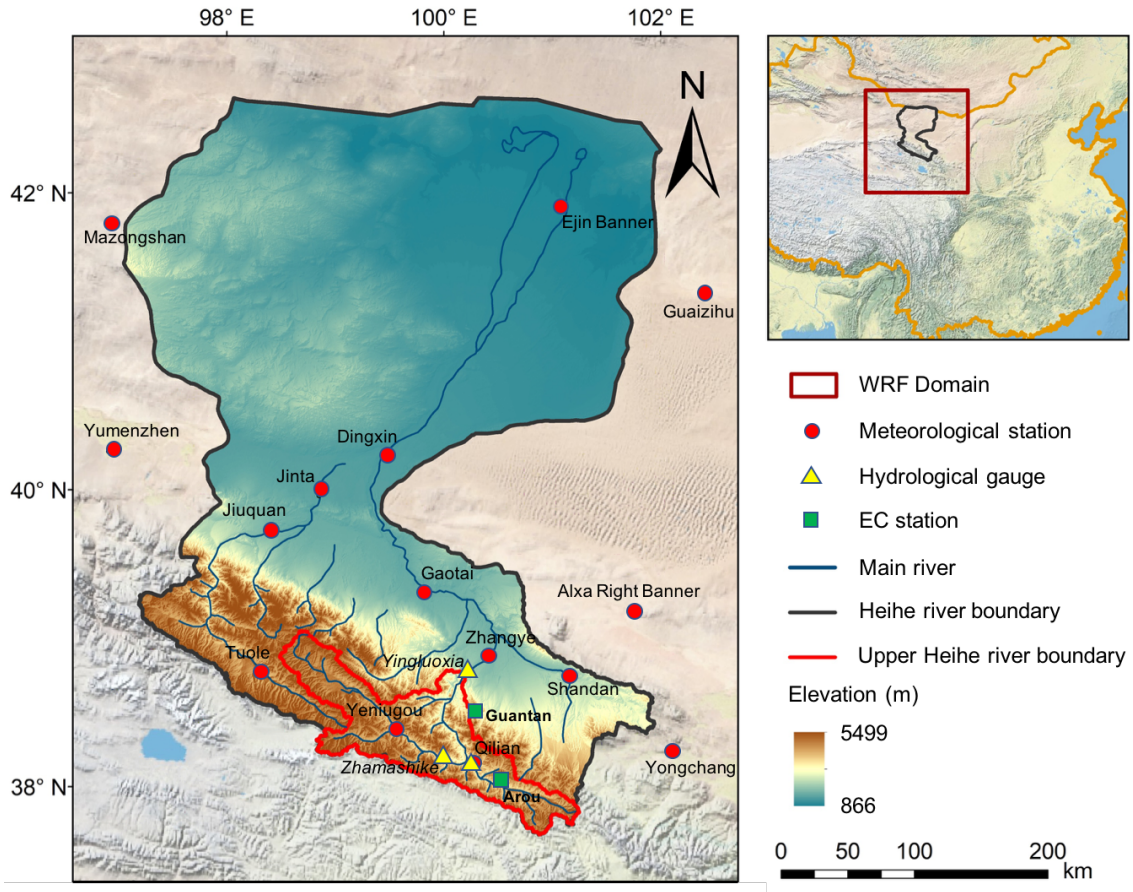

Figure 1.1: Topography and river stream network of the drainage of Heihe rive basin with the location of nearby meteorological sites and hydrological gauges in the upper reach (left figure). The location of the Heihe river basin and the WRF domain (top right figure).

In this study, it is particularly focused on the upstream of HRB (upper HRB), which outlets at the Yingluoxia hydrological gauge, with a drainage area of 10,009 km^2 (Figure 1.1). The upper HRB generates nearly 70% of total river runoff of the whole HRB (Yang et al., 2015). After Yingluoxia gauge, the river runoff is used for supplying the agriculture irrigation and social economic development in the middle reaches. In the upper HRB, the Heihe River is comprised by two major rivers from the east and the west, whose streamflow are measured by Qilian and Zhamashike hydrological gauges, respectively (Figure 1.1). The upper HRB is entirely situated in the Qilian mountains with a high alpine and complex terrain, with elevations ranging from 2,100 to 5,200 m.

1.2 Research objectives and questions

This study aims to address two central questions concerning integrated Earth system modeling:

- How good is the performance of coupled atmospheric-hydrological modeling in a poorly gauged, arid and complex terrain region such as Heihe River Basin?
- How and to what extent does the lateral terrestrial hydrological parameterization affect the regional water cycle and land-atmosphere interactions, with respect to standard atmosphere modeling?

From these two main questions, the specific objectives are derived as following:

- Evaluating the performance of the fully coupled WRF-Hydro modeling in simulating hydrometeorological variables.
- Investigating the impact of resolved lateral terrestrial water flow on the joint atmospheric-terrestrial water cycle and land-atmosphere interactions in a regional climate modeling system.
- Exploring precipitation recycling features in the high alpine and complex terrain region Heihe River Basin.

1.3 Innovation

The innovation in this Ph.D. dissertation consists of:

- Further development and application of the WRF and WRF-Hydro model systems, allowing to resolve lateral terrestrial water flow to decipher the complex interactions of land-atmosphere processes.
- High resolution fully coupled atmospheric-hydrological modeling in convection permitting mode.
- Application of the coupled modeling to the water-limited, high alpine, cold and complex terrain region Heihe River Basin for a relatively long period of 3 years.
- Implementation and application of the state-of-the-art online diagnostic tools, atmospheric moisture budget analysis (Arnault, 2013; Arnault et al., 2016b) and three-dimensional atmospheric moisture tracing method (e.g. Knoche and Kunstmann, 2013; Arnault et al., 2016b; Insua-Costa and Miguez-Macho, 2018), to analyze the atmospheric water budget and land-atmosphere interactions.
- Assessment of the diurnal cycle of surface energy budget and the sensitivity of planetary boundary layer (PBL) parameterization in coupled modeling.

It is noted that this dissertation includes material from the following peer-reviewed article:

- Zhang, Z., Arnault, J., Wagner, S., Laux, P., Kunstmann, H. (2019). Impact of lateral terrestrial water flow on land-atmosphere interactions in the Heihe river basin in China: Fully coupled modeling and precipitation recycling analysis. Journal of Geophysical Research: Atmospheres, 124(15), 8401–8423. doi:10.1029/2018JD030174.

Besides, the author of the thesis has contributed to the following WRF and coupled WRF-Hydro studies conducted in Europe during the Ph.D. period. However, as these studies are not directly related to the main topic and the study region of this dissertation, they are not elaborated in the thesis:

- Arnault, J., Rummler, T., Baur, F., Lerch, S., Wagner, S., Fersch, B., Zhang, Z., Kerandi, N., Keil, C., Kunstmann, H. (2018). Precipitation sensitivity to the uncertainty of terrestrial water flow in WRF-Hydro: An ensemble

analysis for central Europe. Journal of Hydrometeorology, 19(6), 1007–1025. doi:10.1175/JHM-D-17-0042.1.

- Arnault, J., Wei, J., Rummler, T., Fersch, B., Zhang, Z., Jung, G., Wagner, S., Kunstmann, H. (2019). A Joint Soil-Vegetation-Atmospheric Water Tagging Procedure With WRF-Hydro: Implementation and Application to the Case of Precipitation Partitioning in the Upper Danube River Basin. Water Resources Research, 55(7), 6217–6243. doi:10.1029/2019WR024780.

1.4 Outline of the thesis

This thesis consists of 7 chapters with respect to the scope of the study. After the general introduction of specific research objectives of this study and the basis of study region in this chapter, Chapter 2 gives the description of the WRF and WRF-Hydro modeling framework, methodology and the reference data sets. Chapter 3 presents the experimental design of the modeling approach and the evaluation of simulated hydrometeorological fields, and Chapter 4 elaborates the analysis of joint atmospheric-terrestrial water budget and precipitation recycling. Parts of Chapter 3 and Chapter 4 are published in Zhang et al. (2019). The diurnal cycle of the surface energy balance is analyzed in Chapter 5. Furthermore, regarding the uncertainties existed in numerical climate modeling, Chapter 6 investigates the sensitivity of land-atmosphere interactions with respect to varying PBL parameterizations. Lastly, main conclusions and perspectives are summarized in the Chapter 7.

2 Methods and data

In this thesis, numerical simulation results are based on the WRF atmospheric model, the Noah land surface model and the hydrological enhanced WRF-Hydro model. The brief theoretical overview of these models, the quantification methodology and the evaluation data sets including in-situ observations and gridded data are described in this section.

2.1 WRF and Noah land surface modeling system

The Weather Research and Forecasting (WRF) modeling system is used for addressing the research objectives in this study. The WRF model is a fully compressible, non-hydrostatic and mesoscale meteorological model system designed for atmospheric research and operational forecasting applications (Skamarock and Klemp, 2008). It is applied for a wide range of meteorological application across multi-scale from tens of meters to thousands of kilometers and it is widely-used for numerical weather prediction and climate modeling (Powers et al., 2017). The WRF model features two dynamical solvers, a data assimilation system and a software architecture which supports parallel computation and system extensibility. Two variants of the WRF dynamic solver are known as Advanced Research version of WRF and WRF-NMM (non-hydrostatic mesoscale model), which are respective released by NCAR Mesoscale and Microscale Meteorology Division and National Centers for Environmental Prediction (NCEP). The WRF-NMM intends for weather forecasting and hurricane forecasting. In this study, the Advanced Research version of WRF is used as it focuses on both research and operational numerical weather prediction (NWP) applications, regional climate downscaling, and other earth system model coupling.

The WRF model uses a terrain-following hydrostatic pressure coordinate system (σ coordinate) for vertical grid stretching (Laprise, 1992). The compressible non-hydrostatic Euler equations with integration of moisture are implemented in a model

dynamics solver. A staggered Arakawa-C horizontal grid is used for model spatial discretization, and the third-order Runge–Kutta integration scheme is used for temporal discretization. The velocity vectors u, v, w are calculated at the centers of the left/right, front/back, bottom/top grid cell-face, and the other variables are calculated as mass point at the center of each grid cell box. A detail design of the WRF model system is introduced in Skamarock and Klemp (2008).

The basic WRF model for a real-data application consists of terrestrial static conditions setting, the transient boundary conditions and model physics parameterizations. Stationary fields including terrain elevation, land use and soil texture categories, land-sea mask, annual mean deep soil temperature, monthly vegetation fraction, monthly albedo are considered as static conditions for setting up a WRF simulation. 3-D meteorological specified fields of horizontal wind, temperature, pressure, geopotential height and moisture are used as meteorological lateral boundary conditions, and the spatially distributed 2-D fields of sea-ice, sea-surface temperature, physical snow depth, albedo and vegetation fraction are used as lower boundary conditions. These specific boundary conditions are frequently updated (e.g. every 6 hours) through the whole simulation time, and can be generally obtained from a General Circulation Model (GCM) output or from parent simulation of regional climate simulation output. Since the WRF model only explicits the atmospheric processes that are larger than its grid space, physical parameterizations and empirical laws are needed for taking into account the heat, momentum, and moisture processes in the sub-grid resolution. The physics parameterizations for the WRF model include of:

- Radiation scheme: external solar forcing including absorption, reflection and scattering in the atmosphere and the land surface; infrared and thermal radiation absorbed and emitted by atmospheric gases and surface
- Cloud microphysics: water phase mixing and conversion, grid-scale precipitation
- Planetary boundary layer: sub-grid scale fluxes due to eddy transports
- Cumulus parametrization: sub-grid scale precipitation due to clouds and shallow and deep convection
- Land surface physics: moisture and heat flux exchange in land surface layer with respect to the radiation, wind, temperature, humidity and precipitation forcing

- Surface layer: interface between land surface and atmosphere, where friction velocities and exchange coefficients are defined

Figure 2.1 presents the schematic overview of the physical parameterizations in WRF and their interactions (Dudhia, 2014). Several different parameterization schemes are available in the current WRF model version (NCAR, 2015). These are detailed in Skamarock et al. (2008) and can be simply chosen for each simulation from the WRF configuration file (WRFV3/run/namelist.input).

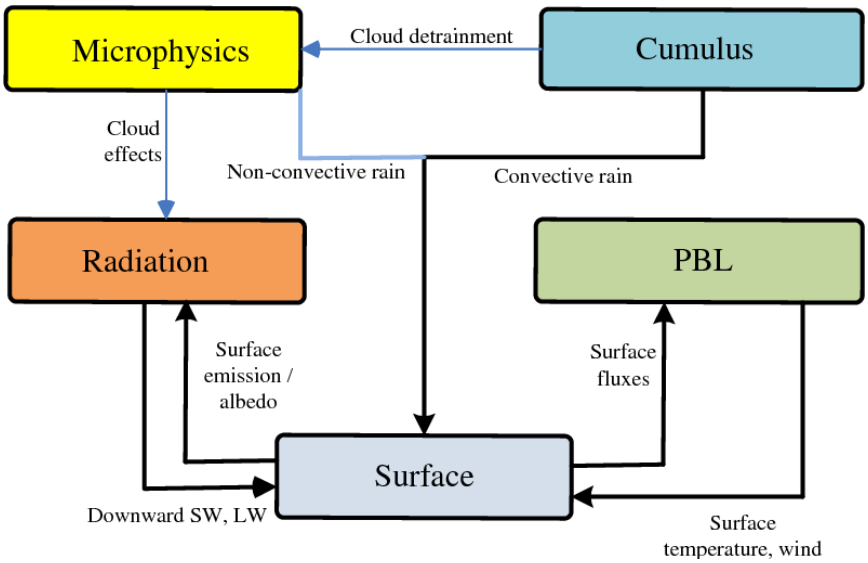

Figure 2.1: Schematic of the interactions of WRF physics parameterizations, by Dudhia (2014).

Land surface models (LSMs) provide the lower boundary interactions in the form of moisture and heat exchanges at the land-atmosphere interface (Figure 2.1). As a commonly used LSM, the Noah-LSM in the standard WRF modeling is used in this study and it is further enhanced with multiple lateral hydrological processes.

The Noah-LSM, originated from the Oregon State University LSM (Chen and Dudhia, 2001; Ek et al., 2003), is designed for moderate complexity and computational efficiency without considering the sub-grid spatial variability. It is now extensively used by the climate modeling community (e.g. WRF model) and NASA's Land Data Assimilation Systems (e.g. Rodell et al., 2004; Mitchell et al., 2004; Xia et al., 2012a,b). The schematic of the Noah-LSM structure in the WRF model is given in Figure 2.2. Its structure is based on coupling of the diurnally dependent Penman potential evaporation scheme of Mahrt and Ek (1984), the multi-layer soil model of Mahrt and Pan (1984) and the primitive canopy model of Pan and Mahrt (1987).

The modestly time-dependent canopy resistance scheme of Chen et al. (1996) is extended in the model for simulating latent heat fluxes. A simple water balance model of Schaake et al. (1996) is used for simulating the surface runoff, and the physics of Koren et al. (1999) are used for snow-pack and frozen ground parameterizations. The Noah-LSM has a single canopy layer and calculates prognostic variables including soil moisture and temperature in soil layers, water retained on the canopy, and ground snow storage. It uses the diffusive form of Richards' equation and thermal diffusion equation for simulating the vertical water and heat transport in a 2 m depth, with 4-layer homogeneous column of thicknesses 0.1, 0.3, 0.6, and 1.0 m from soil surface toward the bottom. The lower 1.0 m soil layer plays a role as a reservoir with gravity drainage at the bottom. The further description of model physics is given in Chen and Dudhia (2001).

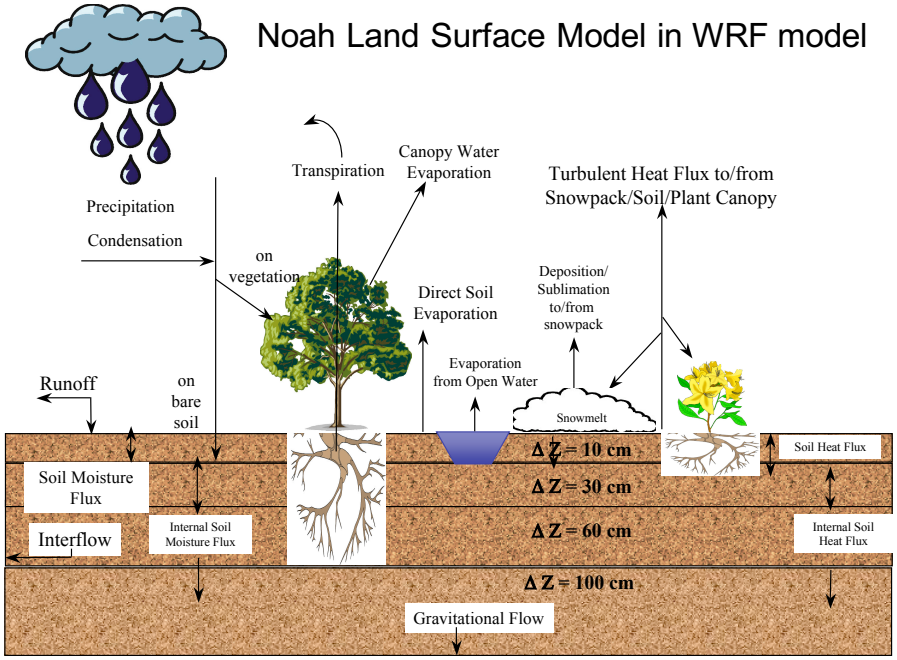

Figure 2.2: Schematic of the Noah-LSM in WRF model. Adapted from `https://ral.ucar.edu/solutions/products/unified-noah-lsm.php`.

2.2 WRF-Hydro model and its coupling system

The hydrological extension system WRF-Hydro, developed by NCAR, is chosen for the coupled atmospheric-hydrological modeling approach. The WRF-Hydro model is designed to facilitate the coupling architecture for the hydrological modeling components to atmospheric model and other Earth System Model framework. It is increasingly used by both atmospheric and hydrological communities for land-atmosphere interactions analysis (e.g. Arnault et al., 2016b; Xiang et al., 2018), water budget studies (e.g. Senatore et al., 2015; Kerandi et al., 2018; Li et al., 2017a; Rummler et al., 2019; Lin et al., 2018), and hydrological prediction (e.g. Yucel et al., 2015; Givati et al., 2016; Salas et al., 2018; Maidment, 2017). Some essential details of WRF-Hydro model physics and its coupling system are provided below, and the complete description of the WRF-Hydro system is available in Gochis et al. (2015).

The enhanced hydrological processes provided in WRF-Hydro are two-way interactive with the Noah-LSM. Comparing with the Noah-LSM which only simulates the vertical water fluxes, WRF-Hydro improves the description of terrestrial hydrological processes by considering the lateral transport of water flow at the land surface and subsurface, also with river streamflow confluence. Specifically, the fundamental enhancement by WRF-Hydro is that the infiltration capacity excess water as well as the exfiltrated water from supersaturated soil are allowed to be ponded, laterally moved and re-infiltrated at land surface, rather than be simply removed as in 1-Dimensional LSMs such as the Noah-LSM.

2.2.1 Subsurface and surface lateral flow routing

A detailed representation of the dominant local landscape gradient is necessary for resolving the lateral terrestrial moisture processes, although the estimation of those gradient features is scale dependent. Hydrological processes are usually described at a hyper grid resolution from meters to hundreds meters, whereas atmospheric modeling is generally simulated at km-scale resolution. WRF-Hydro employs a subgrid disaggregation-aggregation procedure for transporting the hydrological variables between the hydrological routing processes and main Noah-LSM processes. By the means of this procedure, the subsurface and surface lateral flow routing is two-way processed with Noah-LSM and WRF modeling. Succeeding every Noah-LSM loop,

the specific hydrological state variables, including soil moisture, maximum soil moisture content and lateral saturated conductivity for each layer, as well as the calculated infiltration excess, ponded water depth, are disaggregated by a time-step weighted method (Gochis et al., 2015), according to a predefined integer aggregation factor (the ratio between Noah-LSM grid and WRF-Hydro sub-grid). To preserve the spatial variability of the soil moisture content on the sub-grid from one model time-step to the next, linear sub-grid weighting factors are assigned. These values provide the fraction of the total Noah-LSM grid value that is partitioned to each sub-grid pixel (Gochis et al., 2015).

After disaggregation of hydrological variables, the lateral terrestrial water flow is successively performed with subsurface lateral flow and surface overland flow routing. This allows the exfiltration from fully saturated soil columns to contribute to the infiltration excesses from the land surface modeling. The method used to calculate lateral flow of saturated soil moisture is that of Wigmosta and Lettenmaier (1999), implemented in the Distributed Hydrology Soil Vegetation Model (DHSVM). It calculates the quasi-three-dimensional moisture transport which considers the effects of topography, saturated soil depth, and depth-varying saturated hydraulic conductivity values.

The surface overland flow routing is described by the steepest descent ("D8") method, implemented in an fully unsteady, spatially explicit, finite-difference, diffusive wave formulation similar to that of Julien et al. (1995) and Ogden (1997). The overland flow is routed when the ponded water depth in a grid cell exceeds a specific retention depth. The ponded water depth which belows retention depth contributes to direct evaporation and infiltration. The backwater effects which allow the water flow on adverse slopes (Ogden, 1997) are also accounted. The lateral overland flow roughness is mapped spatially, based on the land cover classifications. Lastly, the overland flow reaching the channel grid cell is considered as river streamflow and is routed in the channel routing processes.

2.2.2 Channel, reservoir/lake routing and baseflow model

The channel flow routing, reservoir/lake routing, and a simple baseflow model are one-way processed in the WRF-Hydro model. The surface overland flow which reaches the defined channel grid cell is considered as channel inflow. The channel flow is routed

pixel by pixel using an explicit and variable time diffusive wave formulation in the predefined channel grid, and a first-order Newton-Raphson solver is used to integrate the diffusive wave flow formulations. The channel network is defined with trapezoidal geometry, and its shape parameters (bottom width, side slope) and channel roughness coefficients are prescribed as functions of Strahler stream order. Currently, channel flow is only received from overland flow in a one-way manner, meaning that neither channel water depletion, overbank flow nor regional water transportation are simulated.

WRF-Hydro provides a simple mass balance, level-pool reservoir/lake routing scheme for estimating the impact of reservoirs or lakes on hydrological response. A set of reservoirs/lakes objects can be identified and intersected with the channel network. The water storage of reservoirs/lakes and the outflow are estimated using a level-pool routing method (Chow et al., 1988). Fluxes from reservoirs/lakes are considered only through the channel network, meaning that its exchange interaction with atmosphere (i.e. precipitation, evaporation) and with land surface (i.e. recharge, drainage) are not represented.

The deep drainage from the 2-m bottom soil column (percolation) of Noah-LSM is considered as the baseflow (groundwater recharge). By specifying several groundwater sub-basins in the watershed, WRF-Hydro uses either a so-called "pass-through" option or a simple bucket model for roughly estimating the baseflow portion for each sub-basins. For each of them, the percolated water is directly considered as output baseflow by the choice of the "pass-through" option, or is operated into an "exponential bucket" which uses an exponential function and a conceptual bucket depth to achieve the baseflow recharge. It is noted that both two conceptual options do not resolve deep groundwater feedback to the bottom soil layer of Noah-LSM and do not simulate the saturated groundwater lateral transport.

Following above routing and baseflow routines, the hydrologic status variables (soil moisture at each layer, the depth of ponded water) in the fine sub-grid are aggregated back to the native Noah-LSM grid with a simple linear average. In the meantime, spatial weighting factors are updated based on redistributed sub-grid soil moisture and ponded water depth, and then assigned for the next disaggregation of native Noah-LSM values. These lateral redistributed soil conditions within 2-m soil column modify the spatial distribution of moisture fluxes and eventually feed back to atmospheric processes, as they are used in the next iteration of the land surface modeling

scheme.

2.2.3 Offline modeling and coupled modeling

The WRF-Hydro model is designed to enable an improved simulation of hydrological processes at the land surface using a variety of physics-based and conceptual approaches (section 2.2.1 and 2.2.2). It provides two coupling interfaces to achieve integration of land surface processes and atmosphere input, namely offline (one-way coupling) mode and fully coupled mode, as shown in Figure 2.3.

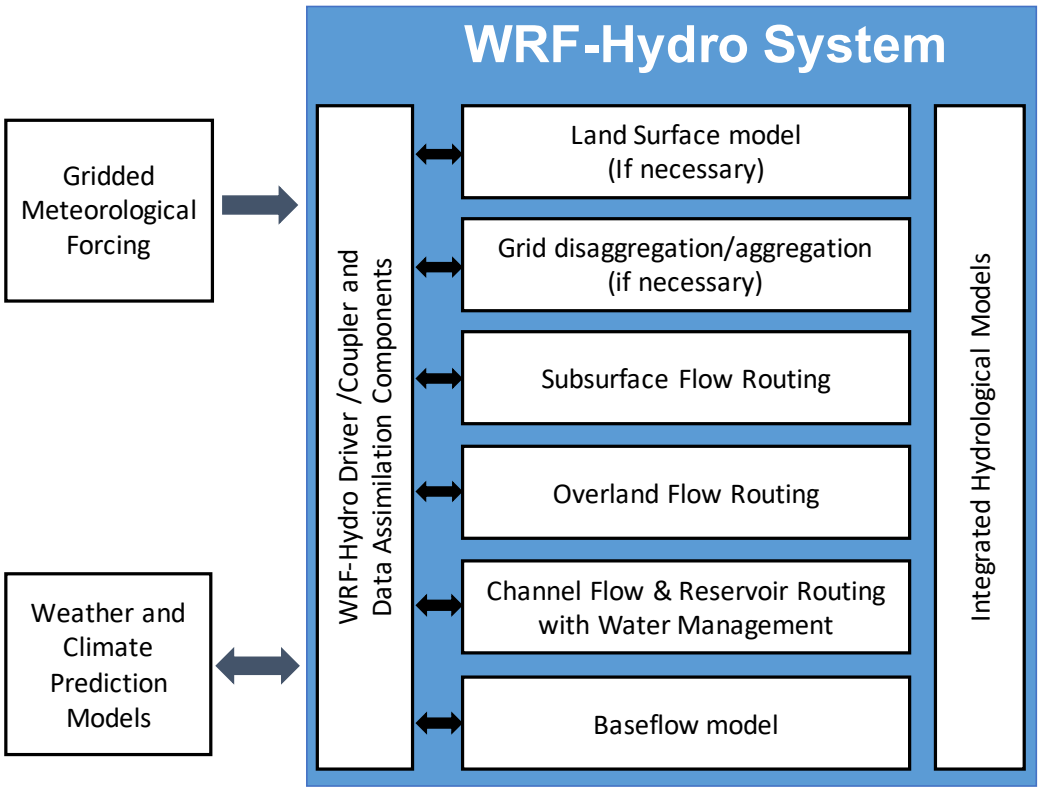

Figure 2.3: Sketch of WRF-Hydro model architecture and its coupling system. Adapted from Gochis et al. (2015)

In its offline mode, WRF-Hydro is a physical-based and fully distributed land surface-hydrological model driven by gridded meteorological forcing. The required forcing variables include downward shortwave and longwave radiation, air temperature, air humidity, pressure, wind speed and precipitation rate, which can be obtained from either meteorological observation or climate operational data set (i.e. analysis, re-analysis, nowcast, forecast). In its fully coupled mode, the hydrological processes in

WRF-Hydro is two-way interacting with atmospheric processes though the coupling interface, which means that the hydrological module is driven by WRF meteorological variables and the updated land surface states feedback to atmospheric processes at each model time-step.

2.3 Methodology

2.3.1 Implementation and evaluation of fully coupled atmospheric-hydrological modeling

As a preliminary step, the WRF-Hydro model is executed in its offline mode, driven by spatial observational data, for the purpose of assessment of this hydrological extension reliability and calibration of hydrological parameters. The observational forcing data has been introduced in section 2.4, and the offline simulation results will be discussed in section 3.2. The offline model evaluation with respect to streamflow simulation is quantitatively assessed by Pearson correlation coefficient (r), percent bias (PBIAS), Nash-Sutcliffe efficiency (NSE; Nash and Sutcliffe, 1970) and Kling-Gupta efficiency (KGE; Gupta et al., 2009). A description of these statistical measures is provided in Appendix A. The offline calibrated parameters are used to implement the fully coupled WRF-Hydro simulation.

Specific aims of the study include to see how a fully coupled atmospheric-hydrological model can simulate the hydrometeorological variables, and to assess the impact of resolved lateral terrestrial water flow on regional water cycle. For this purpose, this study intercompares the simulation results of both the WRF and the coupled WRF-Hydro models, against available observational data sets. The water budget components differences between WRF and coupled WRF-Hydro are used to explain the effects of lateral terrestrial water flow on regional climate. The simulated streamflow from fully coupled WRF-Hydro is compared and discussed with gauge observation records and offline WRF-Hydro results.

2.3.2 Joint atmospheric-terrestrial water balance

Describing the joint atmospheric-terrestrial water balance for a specific region is commonly used for quantitative evaluating the interactions between the atmospheric and terrestrial components of regional water cycle at the land-atmosphere interface. Water balance analysis is performed in the upper HRB, since the anthropic irrigation and the channel water consuming in the middle and lower reaches of HRB are not represented in the current modeling approach. Considering that there is no runoff inflow in the upper HRB, the terrestrial water balance in the upper HRB can be written as:

$$\frac{dS}{dt} = P - ET - R \tag{2.1}$$

where dS/dt $[mm]$ is the terrestrial water storage change in the region, and P $[mm]$, ET $[mm]$ and R $[mm]$ are the regional precipitation, evapotranspiration and total runoff, respectively.

The equation of the regional atmospheric water balance is written as follows:

$$\frac{dW}{dt} = -\nabla \cdot \vec{Q} + ET - P \tag{2.2}$$

with

$$-\nabla \cdot \vec{Q} = Q_{in} - Q_{out} \tag{2.3}$$

dW/dt $[mm]$ indicates the integrated moisture amount change in the atmosphere, and Q $[mm]$ indicates the atmospheric moisture flux. $-\nabla \cdot \vec{Q}$ $[mm]$ denotes the convergence or net balance of integrated water moisture across the atmospheric lateral boundaries of the specified region, and it can be calculated as the difference between lateral inflow moisture Q_{in} $[mm]$ and lateral outflow moisture Q_{out} $[mm]$.

In the atmospheric moisture calculation, considering the moisture fluxes computation from model outputs often produces imbalance errors (e.g. Schär et al., 1999; Roberts and Snelgrove, 2015; Kerandi et al., 2018). Using the approach of Arnault et al. (2016a), the entire atmospheric moisture budget is counted by summing up online the atmospheric moisture tendencies in every modeling time-step and in vertical, which allows grid-scale closure. This online budget method also decomposes the grid-resolved horizontal transport water terms into the west, east, south and north

flux vectors, in order to calculate Q_{in} and Q_{out}. The description of this online budget method and the computation of water budget for a irregular domain are provided in Appendix B.

2.3.3 Land-atmosphere interactions quantification

To identify the effect of the enhanced hydrological processes on atmospheric modeling, the bulk recycling method and a three-dimensional evaporated moisture tracing method are used for quantifying feedback between the land surface and the atmosphere.

Bulk precipitation recycling and efficiency: Based on the joint atmosphere-terrestrial water budget analysis in Section 2.3.2, two bulk indices are applied as quantifying measures of the water recycling and land-atmosphere interactions in numerical regional climate models, that are the recycling rate β and precipitation efficiency χ (Schär et al., 1999). Assuming the well-mixing of the water molecules originating from evapotranspiration within and outside of the analysis domain and neglecting the return flow contribution (e.g. Schär et al., 1999; Arnault et al., 2016a), two bulk indices are deduced as:

$$\beta = \frac{ET}{Q_{in} + ET} \tag{2.4}$$

$$\chi = \frac{P}{Q_{in} + ET} \tag{2.5}$$

The recycling rate β is defined as the ratio of precipitation in a certain region that originates from the evapotranspiration within the same region, so that a higher β corresponds to a higher contribution of local evaporated water to the local precipitation (Kunstmann and Jung, 2007). The precipitation efficiency χ describes the fraction of water entering a certain region, either by evapotranspiration or the atmospheric transport, that subsequently falls as precipitation within the same region.

Evaporation tagging: In order to account for moisture distribution characteristics inside the region which are neglected in the bulk method (e.g. Burde and Zangvil, 2001; Arnault et al., 2016a), the evaporated water tracing method, known as

E-tagging, is additional used. The E-tagging method is an online diagnostic method which quantitatively measures the evaporated moisture from the land surface until it falls as precipitation (e.g., Sodemann et al., 2009; Knoche and Kunstmann, 2013; Wei et al., 2015; Arnault et al., 2016a; Insua-Costa and Miguez-Macho, 2018). It has the advantage to relax the vertical mixing assumption of the above-mentioned bulk precipitation recycling by considering the three-dimensional nature of the atmospheric flow. Furthermore, the E-tagging method allows to know the final spatial distribution of the precipitation originating from surface evapotranspiration originating from a given area. The E-tagging method has been elaborated by Knoche and Kunstmann (2013) in the MM5 model and then recently implemented in the WRF model (Arnault et al., 2016a; Insua-Costa and Miguez-Macho, 2018). As the evaporated moisture tracing approach is the diagnostic tool which pure resolved in atmospheric physics, the E-tagging method is directly implemented in the coupled WRF-Hydro modeling based on the study of Arnault et al. (2016a).

The implementation of E-tagging in atmospheric modeling is done according to the following procedure: (1) initializing a source region of traced evaporated vapor and tag it as ET_{tag} $[mm]$, (2) additionally applying the WRF advection scheme on the tagged water species, (3) computing the tagged water phases changes in the microphysics scheme by introducing the fraction of the tagged mass (q_{tag}/q_{total}) to each moisture species, (4) tracing the ET_{tag} until it falls as precipitation, written as P_{tag} $[mm]$. Appendix C gives a more detailed description of the E-tagging algorithm as implemented in the WRF and the coupled WRF-Hydro model. In this case study, the upper HRB is initialized as the source region for the moisture tracing, so that all the evapotranspiration from the upper HRB including the valleys and the mountains is tagged accordingly.

2.4 Data sets

The simulated atmospheric and hydrological characteristics of the HRB and its surrounding area are compared with reference data sets, including available observations and observational based gridded data sets. The used reference data sets in this thesis are introduced in below.

Daily observed precipitation and mean temperature records available from 15 national meteorological stations within and surrounding the study basin, are obtained

from the National Meteorological Information Center of China (http://data.cma.gov.cn/). Daily observed streamflow data of three hydrological gauges named Qilian, Zhamashike and Yingluoxia in the upper HRB are collected from the Hydrological Bureau of Gansu Province. All meteorological and streamflow data sets are of high quality. The missing meteorological data ($\sim$ 1%) is interpolated by the linear relationship between the nearby stations, and the streamflow records of Yingluoxia gauge which is influenced by dam operations in the dry seasons are restored by liner-line fit with 2 upstream records from Zhamashike and Qilian gauges. Two hydro-meteorological observation-strengthened stations, namely Arou station and Guantan station, which are established within the Heihe Watershed Allied Telemetry Experimental Research project (Li et al., 2013) and collected from the West Data center of China (http://card.westgis.ac.cn), are used for further validating simulated precipitation, soil moisture and heat fluxes. The Arou station is located in upper HRB with an elevation of 3,033 m, with underlying surface of flat natural pasture. The Guantan station is located at an elevation of 2,835 m in a forest ecosystem, and measures the fluxes between the canopy and the atmosphere. The location of above station observations is shown in Figure 1.1.

The China Meteorological Forcing Dataset (CMFD) from the Institute of Tibetan Plateau Research, Chinese Academy of Science (available at http://dam.itpcas.ac.cn/data/User_Guide_for_China_Meteorological_Forcing_Dataset.htm) provides a long-term gridded meteorological data over China at 0.1° × 0.1° spatial resolution and 3 hourly temporal resolution. This data set is produced by fusing the 740 operational stations of the China Meteorological Administration (CMA) with various global data sources (He and Yang, 2011; Yang et al., 2010), and its performance has been validated for precipitation patterns in HRB (Pan et al., 2014; Yang et al., 2017b). Besides its use for model validation, the data set of CMFD is also used for the offline WRF-Hydro model calibration (see section 3.2).

The Climate Change Initiative at European Space Agency (ESA) provides the daily soil moisture content data set (Θ_{CCI}, available at http://www.esa-soilmoisture-cci.org) at a spatial resolution of 0.25° and is used for validating the simulated surface soil water content. The Θ_{CCI} data set merges the soil moisture data retrieved from multiple active and passive microwave sensors, and shows an acceptable performance for the grassland in China (An et al., 2016).

The evapotranspiration data set of FLUXNET model tree ensembles (MTE, available

at https://www.bgc-jena.mpg.de/geodb/projects/Home.php) and Global Land Evaporation: Amsterdam Methodology (GLEAM) data set version 3 (available at https://www.gleam.eu) are both used for the evaluation of simulated evapotranspiration. The FLUXNET MTE data set is derived by empirical upscaling of eddy covariance measurements from global flux towers network and it provides the monthly gridded evapotranspiration at 0.5° × 0.5°spatial resolution (Jung et al., 2011). The GLEAM data set separately estimates the components of land evapotranspiration (bare-soil evaporation, transpiration, interception loss, open-water evaporation and sublimation) base on satellite-base observation and provides daily data set with spatial resolution of 0.25°(Martens et al., 2017). Although uncertainties exist in these gridded evapotranspiration data sets, they both show a certain capability in representing monthly variations in this study area (Liu et al., 2016; Yang et al., 2017a).

In order to facilitate the comparison to model results, the station observations are compared with the nearest model grid points, and the spatial reference data sets are interpolated to the model grid with the nearest neighbor interpolation method.

3 Experimental design and simulation performance

In this chapter, the experimental design and the model configuration of this study are introduced. WRF-Hydro simulations in offline mode are subsequently performed in order to calibrate the hydrological parameters and to evaluate the hydrological components in the modeling approach. For the model assessment, the analyzed variables of air temperature, precipitation, soil moisture and evapotranspiration from modeling results are spatially and temporally compared with observational reference data sets. Finally, the simulated streamflow from the coupled WRF-Hydro simulation is validated and discussed in section 3.5.

3.1 Experimental design

Two experiments are carried out based on WRF-ARM version 3.7. The first experiment uses the standard WRF model, hereafter referring as WRF-S, and the other experiment uses WRF coupled with the WRF-Hydro model version 3.0 (Gochis et al., 2015), hereafter referring as WRF-H. It is noted that two experiments use the same atmospheric setting and they only differ on the description of lateral terrestrial water flow.

A single downscaled model domain is used to capture most of the atmospheric and land surface features. The model domain has a high horizontal resolution of 3 km with 350×350 grid points with a total area of $1{,}050 \times 1{,}050$ km^2, covering the whole HRB and centered at the upper HRB (Figure 1.1). The vertical grid is set to 40 levels with the model top at 20 hPa. The lateral atmospheric boundary condition is provided by the operational analysis from the European Center for Medium-Range Weather Forecasts (ECMWF), which has a resolution of 0.125° and 6-hourly temporal intervals.

Based on a series of physical parameterization tests, the main physical parameterizations are the Asymmetric Convection Model Version 2 (ACM2) planetary boundary layer scheme (Pleim, 2007), the WRF single-moment 6-class (WSM6) microphysics (Hong and Lim, 2006), the Rapid Radiative Transfer Model (RRTM) longwave radiation scheme (Mlawer et al., 1997), the Dudhia shortwave scheme (Dudhia, 1989) and the Noah-LSM scheme (Chen and Dudhia, 2001). The cumulus scheme is not activated considering that horizontal resolution of 3 km is in a convection permitting scale, that the deep moisture convection can be explicitly simulated by the WRF model(e.g. Weisman et al., 1997; Prein et al., 2015).

Acknowledging the land surface information represents a notable effect on atmospheric modeling in HRB (Gao et al., 2008; Wen et al., 2012), the static land cover and soil texture are replaced by the more accurate data sets (shown in Figure 3.1). The land cover map is derived from the Multi-source Integrated Chinese Land Cover Map (MICLCover; available from `http://westdc.westgis.ac.cn/data/a4262c8a-1543-49c3-9d12-47722f3395f4`) which combines multiple sources of land use maps in China at 1 km spatial resolution. The soil texture map is generated by the Chinese 1:1,000,000 scale Soil Map from Harmonized World Soil Database (HWSD V1.2).

As described in section 2.2.1, a hydrological routing sub-grid for representing the local landscape gradients and resolving the lateral terrestrial water processes, needs to be additional provided in the coupled WRF-Hydro modeling. In the WRF-H experiment, the sub-grid data set has a finer horizontal resolution of 300 m, including the high resolution topography, flow direction, channel grid, Strahler stream order, and groundwater basin mask. It is derived from Hydrological data and maps based on Shuttle Elevation Derivatives at multiple Scales (HydroSHEDS, available at `http://hydrosheds.cr.usgs.gov`) data set (Lehner et al., 2008) and prepared with the ArcGIS pre-processing tools. Figure 3.2 shows the hydrological sub-grid topography and the predefined river channels for the upper HRB. In the WRF-H experiment, the overland flow routing, subsurface flow routing, channel flow routing and the baseflow bucket model are considered.

The two modeling experiments are performed from 2008 to 2010. A 3-year period is chosen for evaluating the interannual variability of the water budgets and the effects of lateral hydrological processes. Initial soil moisture is provided by a 2-year WRF spin-up simulation, in order to develop relative equilibrium states of soil moisture. Above experiments settings are summarized in Table 3.1.

TABLE 3.1: Experiments setup and physical parameterizations.

Subject	WRF-S	WRF-H
Common atmospheric setup		
Driving data	ECMWF operational analyses	
Boundary update	6 hours	
Horizontal resolution	3 km	
Horizontal grid number	300 × 300	
Vertical discretization	40 levels	
Model time-step	20 s	
Output frequency	hourly	
Simulation period	2-year spin-up, 2008–2010 for evaluation	
Microphysics	WSM6 (Hong and Lim, 2006)	
Cumulus parameterization	None	
Planetary boundary layer scheme	ACM2 (Pleim, 2007)	
Longwave radiation	RRTM (Mlawer et al., 1997)	
Shortwave radiation	Dudhia (Dudhia, 1989)	
Hydrological setup		
Land surface model	Noah-LSM	Noah-LSM with WRF-Hydro
Sub-grid Δx, Δy	None	300 m
Routing options	None	overland flow, subsurface flow, channel flow, bucket baseflow

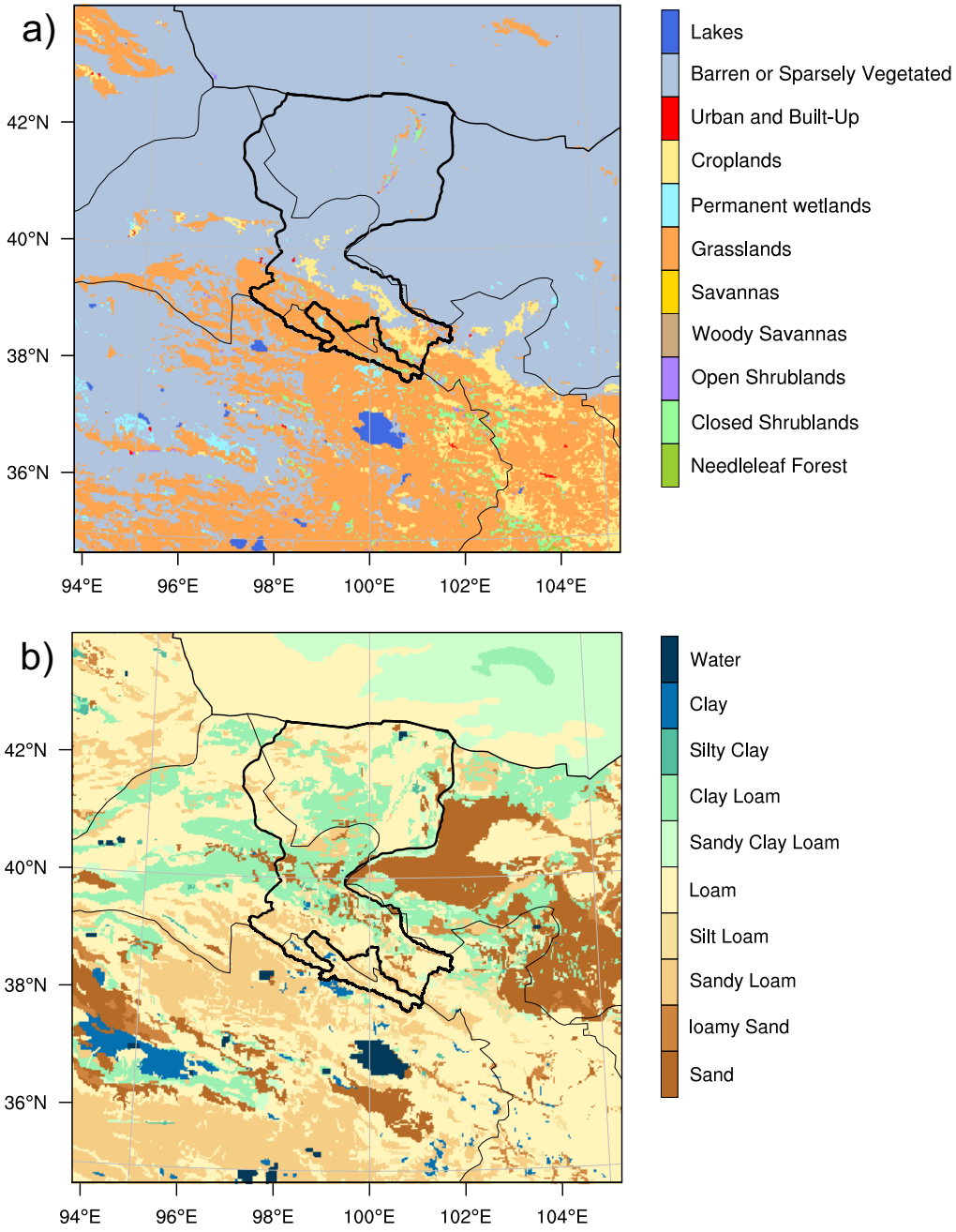

Figure 3.1: Land cover distribution from MICLCover (a) and top layer soil texture from HWSD (b) used in the WRF model domain. The Heihe river basin is contoured in black.

3.2 Offline WRF-Hydro evaluation

Offline WRF-Hydro runs are performed in the upper HRB for the purpose of hydrological parameters calibration and hydrological extension assessment. The CMFD

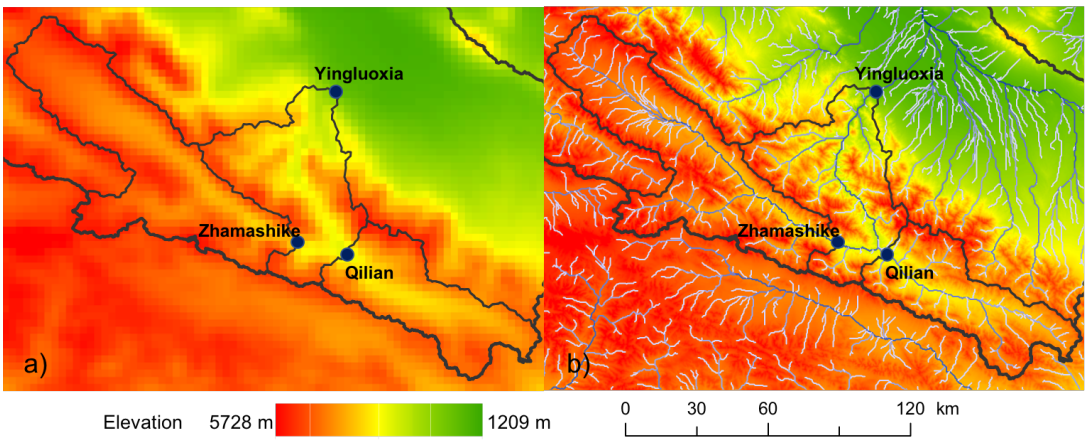

Figure 3.2: Zoom of the topography and stream channels with hydrological gauges in upper Heihe river basin. a) 3 km resolution WRF model grid, b) 300 m high-resolution WRF-Hydro routing sub-grid with channels/orders.

data set(described in section 2.4) is used as forcing meteorological input since some researches confirmed its reliability for regional hydrological studies within and nearby the study area (Pan et al., 2014; Zheng et al., 2016; Yang et al., 2017b). All the required meteorological variables (described in section 2.2.3) are interpolated to the model grid by the distance-weighted average method. After 1.5-year for modeling warm-up, the offline WRF-Hydro is calibrated for the period from June to December in 2008 based on daily streamflow records in Yingluoxia gauge. The gauge records of Yingluoxia in 2009 as well as two upstream Qilian and Zhamashike gauges from June 2008 to December 2009 are used for validation.

Related to the parametrization of hydrological models, plenty of variables can be broadly involved in the model optimization depending on different demands (Boyle et al., 2000). For minimizing modeling computational time, the stepwise manual approach is used on offline WRF-Hydro calibration (e.g. Boyle et al., 2000; Yucel et al., 2015; Givati et al., 2016; Kerandi et al., 2018; Li et al., 2017a). The most relevant tunable parameters, including the coefficient of the deep drainage, the scaling factors of infiltration partitioning, surface retention depth, overland flow roughness are stepwise calibrated for reproducing equivalent streamflow amount. The channel grid Manning's roughness coefficient, and the maximum depth and exponent in baseflow bucket model are calibrated afterwards as these are one-way processed in the WRF-Hydro. The detailed calibration procedure and the effects of these parameters on the

streamflow are elaborated in Gochis et al. (2015), Yucel et al. (2015) and Kerandi (2018).

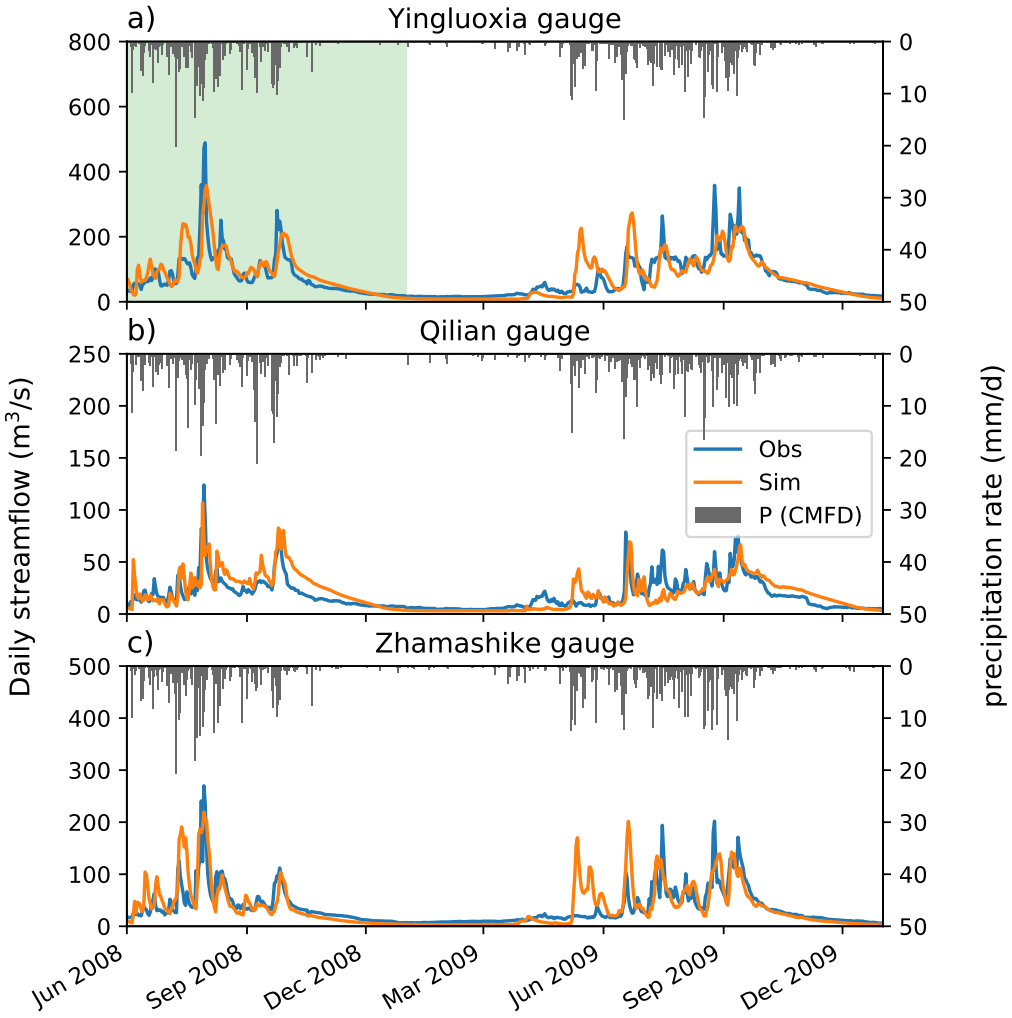

Figure 3.3: Daily time series of simulated hydrographs from the offline WRF-Hydro model for the calibration period (span with green), and for the validation period, at the gauges a) Yingluoxia, b) Qilian, and c) Zhamashike.

The simulated hydrographs from the offline WRF-Hydro are shown in Figure 3.3, and the statistical metrics is presented in Table 3.2. Overall, simulated streamflow is reasonably matched with observations at three gauges. The NSE coefficient of the calibration and validation period at Yingluoxia gauge are 0.60 and 0.57 respectively, and the KGE coefficient reaches the value of 0.79. Validating the model at two upper gauges Qilian and Zhamashike, the simulated streamflow shows the negative percent bias of total streamflow volume of -6.9% and -4.7%, with NSE coefficients of 0.54 and 0.56, and KGE coefficients of 0.73 and 0.71, respectively. However, the calibrated

TABLE 3.2: Statistical metrics of simulated streamflow from offline WRF-Hydro modeling for calibration period and validation period.

	Gauge station	NSE	KGE	PBIAS	r
Calibration	Yingluoxia	0.60	0.79	3.5	0.80
Validation	Yingluoxia	0.57	0.78	-6.7	0.80
	Qilian	0.54	0.73	-6.9	0.76
	Zhamashike	0.56	0.71	-4.7	0.76

streamflow generally underestimates the low flow during the dry seasons and underestimates the main peak flow in the summertime, and presents some unrealistic peak flows during the onset of wet seasons. This suggests that the fast surface flow in the model is well simulated in the study area while the baseflow is oversimplified. The streamflow underestimation in the dry period may also be due to the lack of a glacier module in the current version of WRF-Hydro (Li et al., 2017a). In addition, the unrealistic features in the calibration results, especially during the onset of wet seasons, may come from the uncertainty of the forcing precipitation, which only merges limited meteorological stations in this high mountainous area (see Figure 1.1). Nevertheless, the offline WRF-Hydro clearly shows the ability to produce realistic hydrological regimes in the upper HRB. The calibrated parameters from offline WRF-Hydro are used in the WRF-H experiment.

3.3 Performance of temperature and precipitation simulations

Air temperature Figure 3.4 shows the spatial pattern of the downscaled annual mean 2-m air temperature and precipitation from the CMFD reference data set and the two experiments, as well as the station observations. The spatial variation of the annual averaged air temperature depicted in the reference data set is well simulated by both experiments, with higher temperatures in the flat desert region and lower temperatures in the mountains. The simulated annual mean temperature is relatively higher in comparison to the reference data. Averaged over the whole HRB, the mean temperature is 6.13 ℃ for the reference and 7.79 ℃ and 7.78 ℃ for the

WRF-S and WRF-H, respectively. In the upper HRB, the mean temperature from the reference, WRF-S, and WRF-H is -3.92 ℃, -3.01 ℃ and -3.09 ℃, respectively. The temperature biases for the upper HRB (∼ +0.9 ℃) are smaller than for the whole HRB (∼ +1.6 ℃).

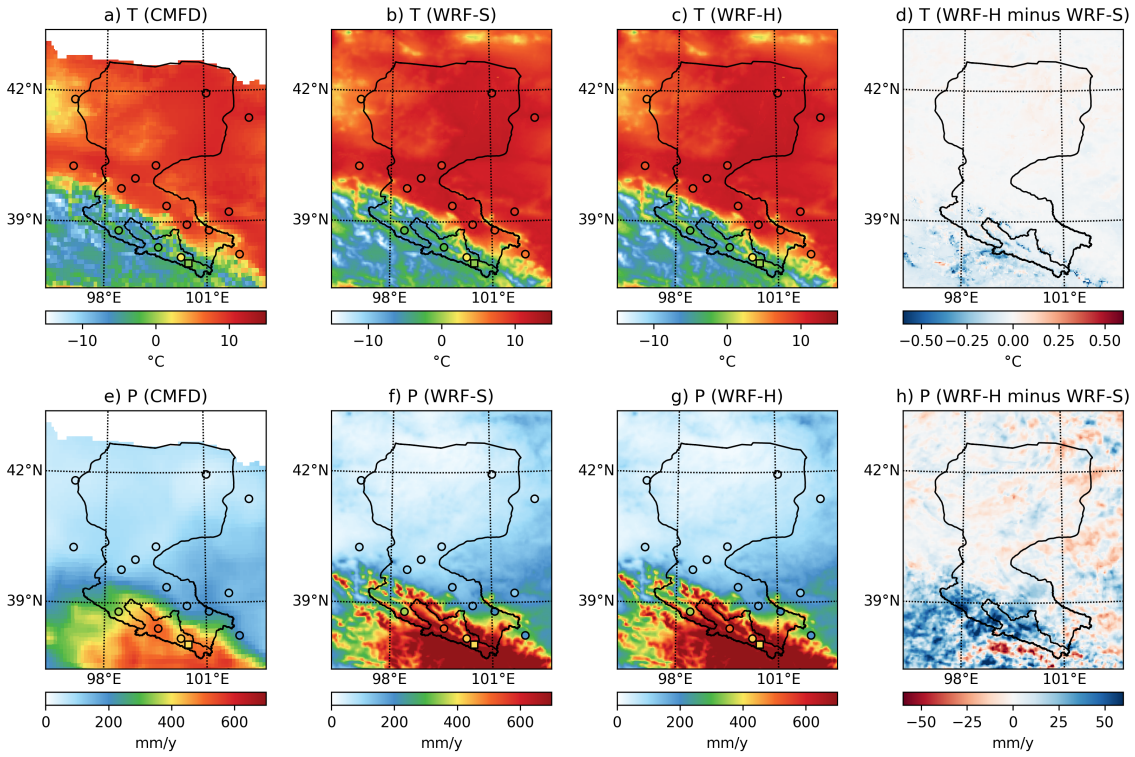

Figure 3.4: Annual mean 2-m air temperature map from a) CMFD reference, b) WRF-S, c) WRF-H, and d) WRF-H minus WRF-S. (e–h) Same as (a–d), but for annual accumulated precipitation.

Figure 3.5a–b display the time series of monthly averaged air temperature in the HRB and the upper HRB, showing that the seasonal variation of the temperature is well reproduced by the two experiments. Temperature biases are mainly due to the fact that the models simulate higher temperatures in the winter period. According to the mean annual temperature maps from WRF-H and WRF-S experiment, WRF-H is slightly colder in the mountainous area, up to -0.4 ℃ for the mountain tops (Figure 3.4d).

Precipitation Since most of the moisture from the East Asian monsoon is blocked by the Tibetan Plateau, the precipitation belt is located at the eastern Qilian mountain at the southeastern HRB, meanwhile the northern parts of HRB are

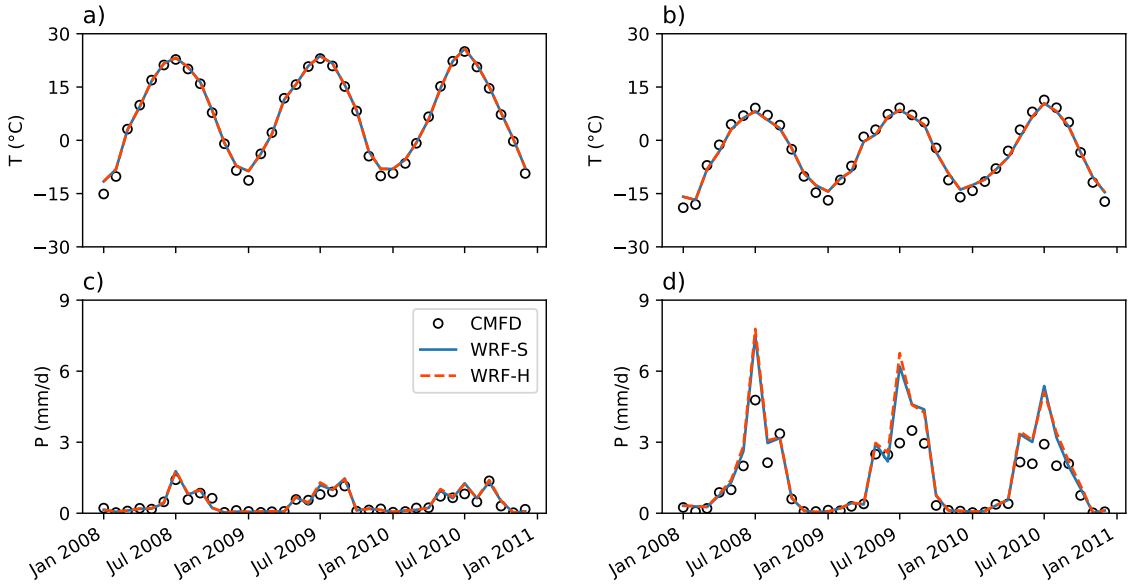

Figure 3.5: Monthly time series of 2-m air temperature (a–b) and precipitation (c–d) from WRF-S, WRF-H, and CMFD reference, spatially averaged for the HRB (a, c), and the upper HRB (b, d).

extremely dry. The spatial variability of annual precipitation is well simulated by the two experiments, highly agreeing with the reference (Figure 3.4e–g). This heterogeneous distribution of precipitation in relation with topography is highlighted at this 3 km high-resolution grid. As shown in Figure 3.5c–d, the two experiments simulate monthly variation of precipitation with comparable wet-dry periods over the study area in good agreement with the CMFD reference. The precipitation in the upper HRB overestimates the CMFD reference by about 200 mm/year. However, with regards to the gridded references, this overestimation from the dynamic downscaling is comparable with many RCMs simulations in this area (e.g., Pan et al., 2014; Wang et al., 2017; Xiong and Yan, 2013; Zhang et al., 2018). This disparity may be due to the fact that the CMA stations used in the data fusing (He and Yang, 2011) in this area are quantitatively insufficient (Figure 1.1), and that all the stations are distributed below the 3500m altitude (Table 3.3), so that the CMFD reference has some uncertainties in representing the high-altitude precipitation (Pan et al., 2014; Yang et al., 2017b).

Table 3.3 further compares the simulated precipitation with station observations, gathering the statistics of the mean annual error (MAE) and monthly Root Mean Square Error (RMSE). With respect to the station observations, the model results

show a wet bias in the mountains and a mixed bias in the flat arid areas. The MAE at the Arou station is significantly higher (more than 220 mm/year) than at the three nearby national meteorological stations Tuole, Yeniugou and Qilian in the high mountains, which is suspected to be due to the lack of snowfall observations in the case of Arou (Wang et al., 2017). Monthly RMSEs with respect to station observations also show higher values at the mountain stations, and 10 out of 16 stations indicate that the WRF-H experiment is slightly better than the WRF-S experiment. In Figure 3.4h, the precipitation difference map shows that the precipitation pattern in WRF-H is slightly shifted in comparison to WRF-S. Some enhanced and reduced clusters of WRF-H precipitation, with respect to WRF-S, are distributed both at the flat area and high mountainous area, and no clear tendency of precipitation spatial differences is detected. Specific to this study area, the WRF-H simulates 5 mm/year and 24 mm/year more precipitation than the WRF-S experiment for the HRB and the upper HRB, respectively.

Table 3.3: Annual precipitation (mm) and the MAE (mm) and RMSE (mm·month^{-1}) of WRF-S and WRF-H comparing with the gauge observations.

			WRF-S			**WRF-H**		
Station Name	Elevation (m)	P-Obs	P-Sim	MAE	RMSE	P-Sim	MAE	RMSE
Ejin Banner	940	32.5	47.1	14.6	9.2	38.1	5.6	8.8
Mazongshan	1,770	52.5	43.6	-8.9	5	39.8	-12.7	4.1
Guaizihu	102	54.1	84.1	30	8.4	86.7	32.6	8.4
Yumengzhen	97	75.1	55.8	-19.3	4.9	59.2	-15.9	5.5
Dingxin	1,177	69.4	67.4	-2	4.7	67.1	-2.3	4.1
Jinta	1,270	81.7	73.1	-8.6	4.2	72.6	-9.1	4.3
Jiuquan	1,477	101.2	101.8	0.6	6.9	100.2	-1	6.1
Gaotai	1,332	137.2	131.5	-5.7	11.1	146.3	9.1	10.8
Alxa Right Banner	1,510	118.6	196.7	78.1	14.9	197.2	78.6	14.7
Tuole	3,367	350.9	365.3	14.4	15.1	375.1	24.2	14.8
Yeniugou	3,320	507.3	477.9	-29.4	17.5	510.9	3.6	19.3
Zhangye	1,482	151.5	172.2	20.7	9.1	181.6	30.1	9.5
Qilian	2,787	425.8	487.4	61.6	22.1	512.3	86.5	21.5
Shandan	1,764	208.7	283.3	74.6	21.4	275.0	66.3	19.7
Yongchang	1,977	195.2	298.6	103.4	20.3	295.4	100.2	20
Arou	3,033	409.6	634	224.4	29.9	654	244.4	33.2

3.4 Performance of soil moisture and evapotranspiration simulations

Soil moisture Figure 3.6 shows the areal daily averaged θ_{CCI} and soil water content (SWC) from the two experiments at the top soil layer (0–10cm), namely θ_{WRF-S} and θ_{WRF-H} for the upper HRB. Due to missing data of θ_{CCI} in high mountains for the reason of ice and snow coverage, the available θ_{CCI} which covers more than half of the area is extracted for counting in this case. As θ_{CCI} describes the soil depth at 0.5–2 cm (Dorigo et al., 2015), the values from θ_{CCI} are generally lower than from the models in the summertime due to the evaporation effect. However, the values of θ_{WRF-S}, θ_{WRF-H} and θ_{CCI} are quite close after the summertime in September and October. θ_{WRF-S} and θ_{WRF-H} values show a similar temporal variability as in θ_{CCI} and WRF-H simulates some higher values which better correspond to the θ_{CCI} reference. Furthermore, Figure 3.7a–d show modeled and observed SWC in two soil layers at the site of Arou and Guantan stations. Both experiments reproduce reasonably well the observed variability of SWC, such as the lower values in the winter time and the dramatic decreasing tendency during the rainy and dry seasons. However, the impressive increase of water content in April is not well represented, as it is generally underestimated with respect to the observation records and the θ_{CCI} reference. This suggests a limited ability of the Noah-LSM in simulating the soil thaw state and related-processes in high mountains (Zheng et al., 2017).

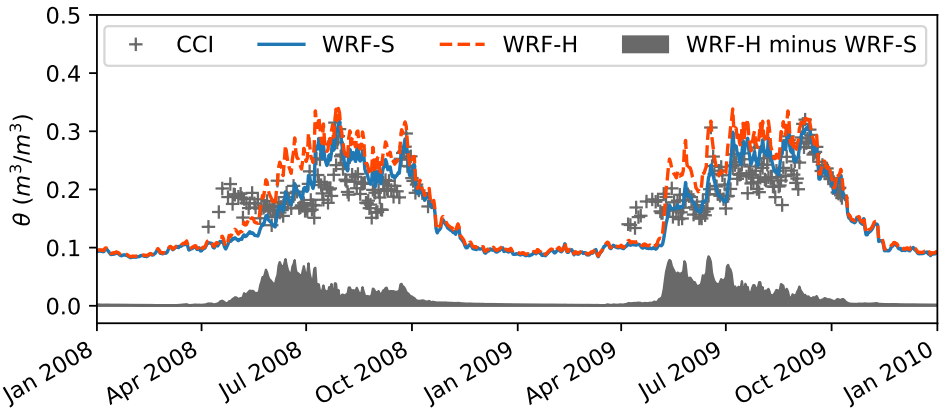

Figure 3.6: Areal averaged daily soil water content (SWC) in the upper HRB area from WRF and WRF-H (from 0 to 10 cm), and from CCI (from 0.5 to 2 cm) for the period from 2008 to 2009.

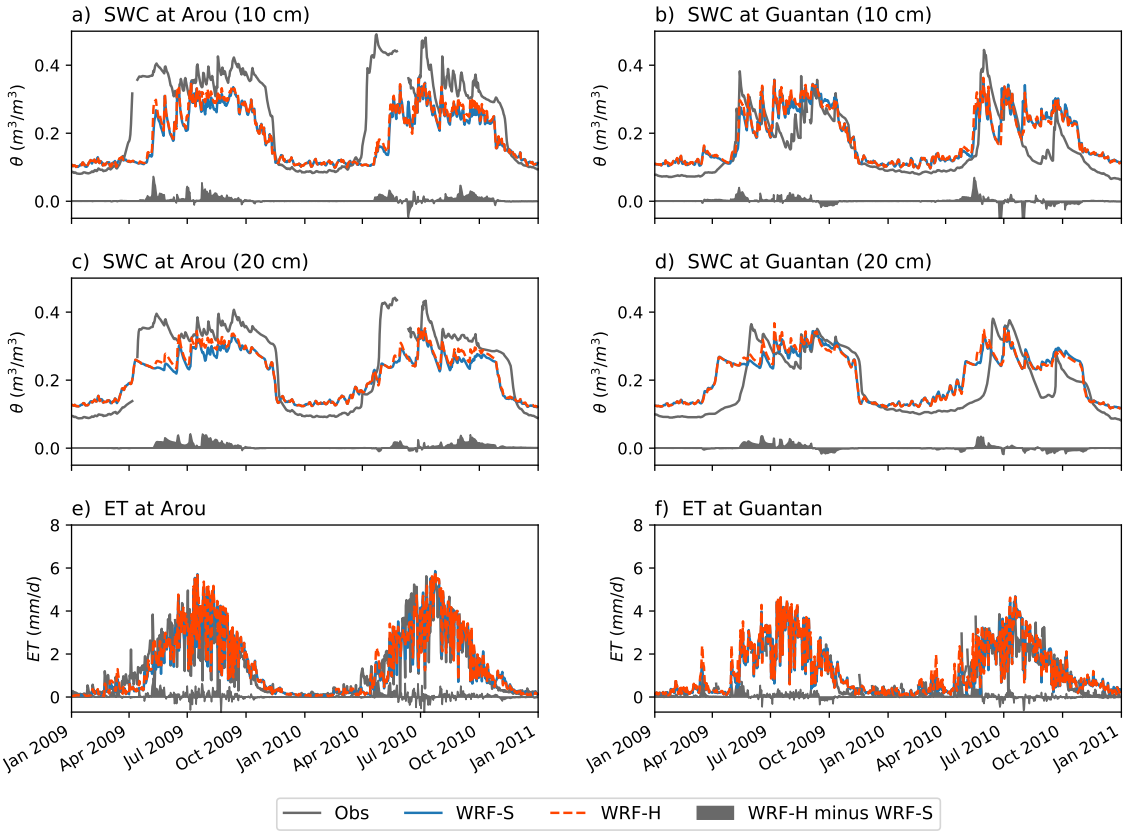

Figure 3.7: Daily time series of soil water content (SWC) results at 0–10 cm depth (a–b), at 10–40 cm depth (c–d), and evapotranspiration (ET) (e–f) from WRF-S, WRF-H, and observation at the locations of Arou station (a, c, e) and Guantan station (b, d, f).

Evapotranspiration Modeled and reference evapotranspiration are shown in Figure 3.8 as maps and areal monthly time series. The simulated evapotranspiration displays spatial features corresponding to the detailed static land conditions. Generally, the simulated evapotranspiration does not show noticeable divergence of distribution with respect to the GLEAM reference. Areal monthly averaged evapotranspiration shows a good agreement in terms of seasonal variability between model results and the two references. Model results are closer to the GLEAM than the FLUXNET-MTE data set. The correlation coefficients of monthly evapotranspiration between WRF-S/WRF-H and GLEAM are 0.85/0.87 and 0.9/0.93 for the HRB and the upper HRB, respectively. Figure 3.7e and 3.7f also show that the two experiments are able to capture the observed daily evapotranspiration magnitudes and variabilities at the sites of the two stations.

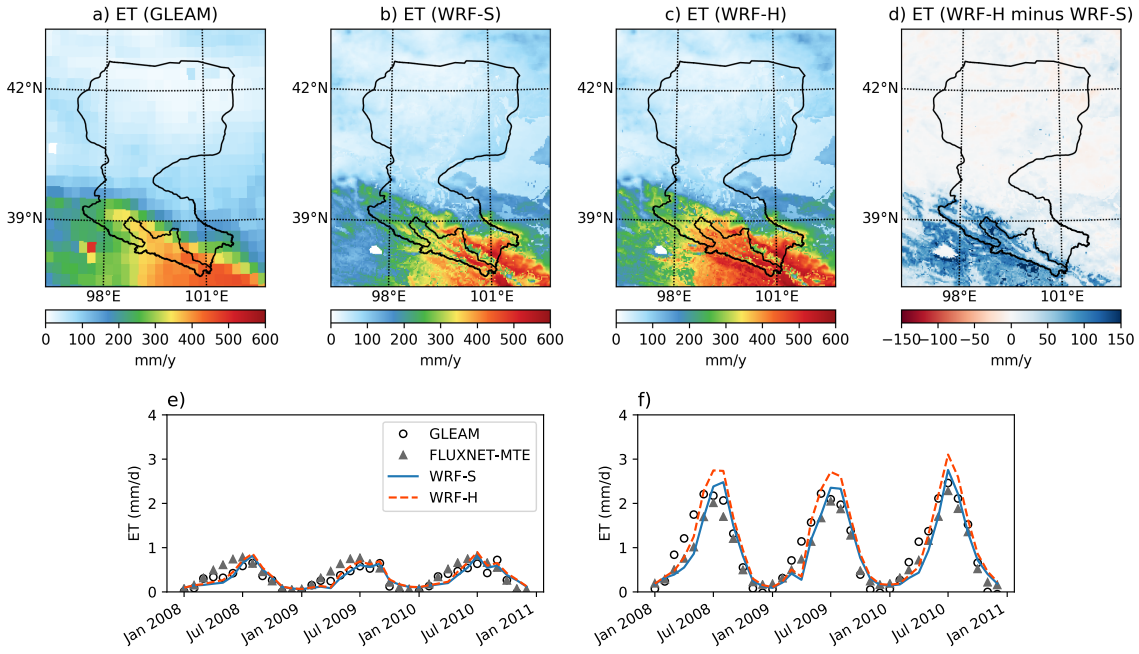

Figure 3.8: Annual mean evapotranspiration (ET) map from a) GLEAM reference, b) WRF-S, c) WRF-H and d) WRF-H minus WRF-S; and areal averaged monthly ET from GLEAM, FLUXNET-MTE, WRF-S, WRF-H for the regions of e) the HRB and f) the upper HRB.

The differences between the two experiments show that the SWC in WRF-H is generally higher than in WRF-S. In the upper HRB, areal averaged differences up to 0.08 m^3/m^3 occur at the beginning of the rainy season, slowly decreasing afterwards until the SWC in the two experiments become identical in the dry period (Figure 3.6). Accordingly, 70 mm/year more evapotranspiration is simulated by WRF-H. This indicates that the laterally moved and re-infiltrated surface runoff induces a longer soil water memory in WRF-H in the upper HRB, in comparison to WRF-S. At the two station sites, WRF-S and WRF-H also show similar differences in behavior of SWC and evapotranspiration, but not as large as for the areal averaged values for the upper HRB. This suggests a reduced influence of overland flowing and re-infiltration in the relatively flat area where the two stations have been installed. The spatial and temporal distribution of these effects are presented in the next chapter.

3.5 Simulated streamflow by coupled WRF-Hydro

The modeled streamflow from the WRF-H experiment is not relying on any direct meteorological observations. It is therefore of utmost relevance to assess the performance of the WRF-H streamflow with respect to the observations.

Figure 3.9 shows the simulated and observed hydrographs at all three gauges as well as the corresponding precipitation rates from the coupled WRF-H. Considering the entire period, the simulated daily streamflow is fairly comparable with the observations. The runoff coefficient, namely the ratio between runoff and precipitation, is 0.42 for the upper HRB according to the observation, and 0.38 according to WRF-H. Statistical matrices are shown in Table 3.4. Moderate but statistically significant (tested at α=0.01) correlation coefficients of 0.74, 0.72, 0.75 are reached between modeled and observed streamflow at Yingluoxia, Qilian, Zhamashike gauges, respectively. In addition, the summer peak flow occurrences and the streamflow recessions after the rainy periods are well simulated, indicating the good response of streamflow to intensive precipitation. However, calculated NSE coefficients are apparently lower, between -1.4 and -0.3, and the KGE coefficients are ranging from 0 to 0.2. These low values are mainly caused by the oversimulation of the main hydrograph peaks and the total streamflow amounts, in relation with the overestimated precipitation in the atmospheric modeling, and potential channel loss neglected in the WRF-Hydro module. Consequently, accumulated streamflow at Yingluoxia outlet reaches a value of 6.91×10^9 m^3, approximately 20% more than the observed streamflow 5.74×10^9 m^3. The streamflow during the dry period is also underestimated, probably in relation with the lack of glacier modeling and oversimplified baseflow modeling. In this case, the modeled baseflow only contributes to 12% of the total simulated streamflow amount.

Table 3.4: Statistical metrics of simulated streamflow from the coupled WRF-Hydro modeling.

Gauge station	NSE	KGE	PBIAS	r
Yingluoxia	-0.3	0.11	20.3	0.74
Qilian	-1.4	0.02	31.6	0.72
Zhamashike	-0.4	0.20	27.1	0.75

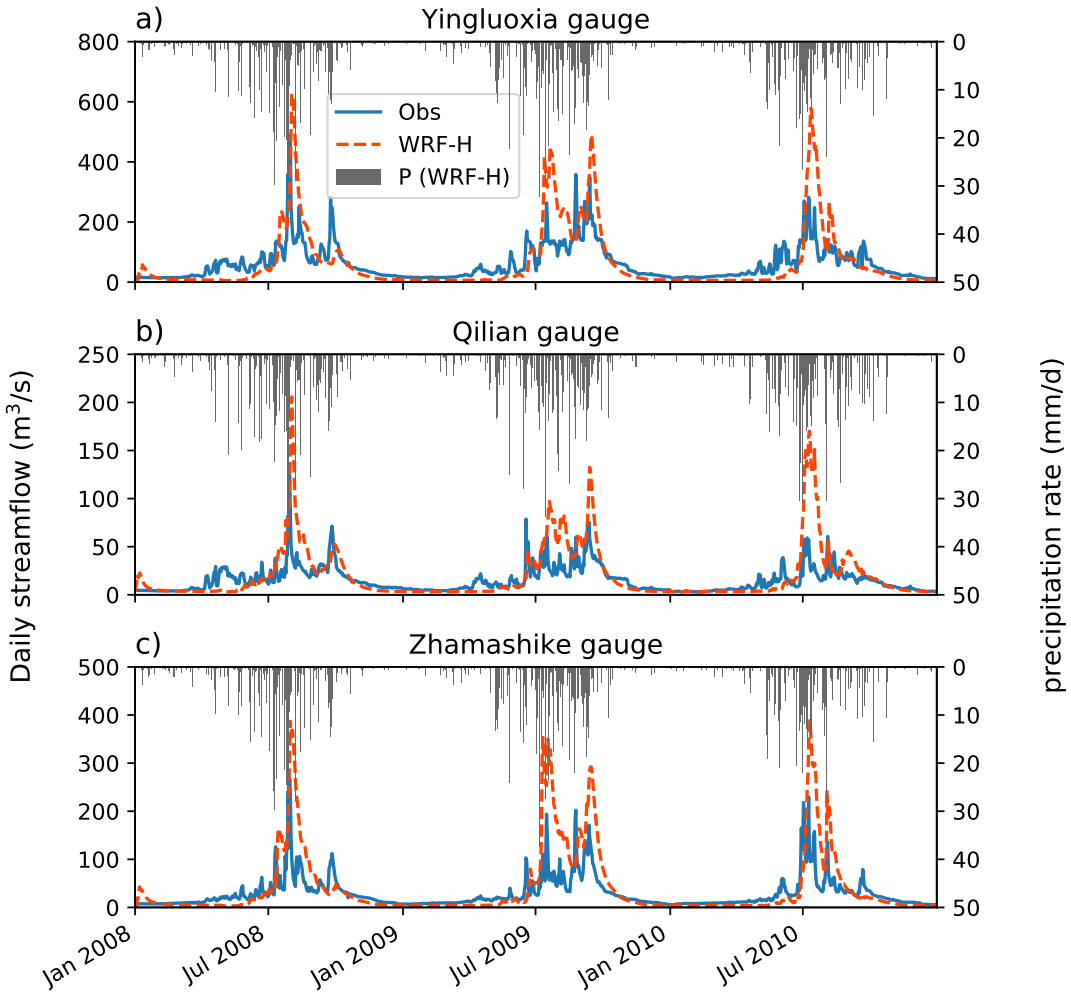

Figure 3.9: Daily time series of simulated hydrographs and precipitation rate from WRF-H at the gauges a) Yingluoxia, b) Qilian, and c) Zhamashike.

Compared to simulated streamflow from offline WRF-Hydro module (Figure 3.3), WRF-H shows a relatively limited ability in reproducing the daily streamflow. This limitation in the fully coupled modeling generally exists in many cases of different climatic basins (e.g., Arnault et al., 2016b; Kerandi et al., 2018; Senatore et al., 2015; Wagner et al., 2016; Rummler et al., 2019). These studies confirmed that the large biases of streamflow simulation in fully coupled modeling are related to precipitation estimation. Additionally, the simulated streamflow from fully coupled modeling is not much affected by light rain events, as the small streamflow peaks at the early rainy periods are much underestimated, which is a different model behavior in comparison to the offline simulation (Section 3.2). This could be related to differences in precipitation intensity and duration which can highly affect the amount of generated

runoff (Dourte et al., 2013; Kokkonen et al., 2004). Moreover, the inconsistency of time-step length in land surface modeling and hydrological modeling also has a large impact on streamflow simulation (Littlewood and Croke, 2013). In the offline calibration runs driven by meteorological data, the land surface model is called at an hourly interval, whereas in the fully coupled mode, the land surface model is called every WRF physics time-step (20s). In particular, the consideration of smaller time-step length in land surface modeling commonly induces more infiltration and less runoff (Senatore et al., 2015). Extensively calibrating the hydrological module by enabling various time-step and using modeled precipitation as the forcing data, as well as further investigating the transferability of the calibrated parameters could be further ways for improving the streamflow simulation in the fully coupled modeling.

3.6 Summary of chapter

In this chapter, two dynamical downscaling experiments with the regional atmospheric model WRF and its hydrological enhanced model WRF-Hydro are implemented in the study area of HRB, from 2008 to 2010. By comparing the modeling results of near-surface hydrometeorological variables with standard WRF model and observational data sets, the modeling skills of the fully coupled atmospheric-hydrological model, that is the coupled WRF-Hydro, are evaluated. Within the chosen model configuration, the coupled WRF-Hydro simulates similar variability of air temperature and precipitation with respect to the standard WRF model. Both the simulations show good agreement with the observational references, along with added values highlighted in convection permitting scale over the poorly gauged mountainous area. In general, simulated air temperature shows a slightly positive bias, and the precipitation is overestimated in the mountains with respect to the CMFD reference data set, while these deviation behaviors are comparable with previous downscaling studies over this region (e.g. Pan et al., 2012, 2014; Wang et al., 2017; Xiong and Yan, 2013; Zhang et al., 2018). Simulated soil water content is comparable with the microwave observation (θ_{CCI}) and in-situ measurements at daily scale. The simulated evapotranspiration from both models show comparable spatial patterns and seasonal variation as exhibited in FLUXNET MTE and GLEAM data sets, and are able to capture the magnitude and variation of observed daily evapotranspiration. The differences of the above analyzed variables relating to the lateral terrestrial water flow

description will be analyzed and discussed in the following chapters.

For the streamflow simulation, results from the offline WRF-Hydro simulation driven by observational based gridded data have shown a reasonable performance in reproducing the daily streamflow for 3 sub-catchments in the upper HRB. In the fully coupled simulation, coupled WRF-Hydro is able to capture the seasonal cycle and variability of observed hydrographs. However, reproducing the daily streamflow with the fully coupled model still remains a challenge, because the precipitation bias from atmospheric modeling is directly transferred into the hydrological modeling.

4 Joint atmospheric-terrestrial water balance and precipitation recycling

Based on model evaluation in Chapter 3, this chapter focus on the characteristics of water components in the joint atmospheric-terrestrial water cycle. Seasonal and interannual variability of simulated terrestrial and atmospheric water budget components over the upper HRB is presented here and compared with previous studies. To seek the effect of lateral terrestrial water flow on this joint regional water cycle, the inter-model comparisons of the water components between the coupled WRF-Hydro and standard WRF are explored and discussed in Section 4.3, notably for a wet period from June to August of 2009. And this effect between the land and atmosphere is further quantified with a precipitation recycling analysis described in Section 2.3.3. The water balance in the middle- and downstream of HRB is not presented, since the current model approach lacks the dominating eco-hydrological processes in this area (e.g. irrigation, underground water pumping, river water consumption by human and desert ecosystem, etc.), which is the focus of integrated multidisciplinary models (e.g. Li et al., 2018a,b; Xie et al., 2018).

4.1 Terrestrial water budget for the upper Heihe river basin

The monthly and interannual variation of terrestrial water budget components for the upper HRB as simulated in WRF-S and WRF-H are shown in Figure 4.1, and the seasonal characteristics are summarized in Table 4.1. Figure 4.2 features the variation of evapotranspiration closely related to the onset and offset of precipitation, which is typical for a semiarid-arid region. Runoff is mostly produced during the summer season, with the highest amount of nearly 4 mm/d in July. Runoff exhibits modest interannual differences since its generation is assuredly correlated with the variation

of precipitation and terrestrial water storage (TWS) change. In general, WRF-S and WRF-H show similar seasonal variation for all terrestrial water budget components, despite for the TWS in WRF-H which changes more dramatically than in WRF-S.

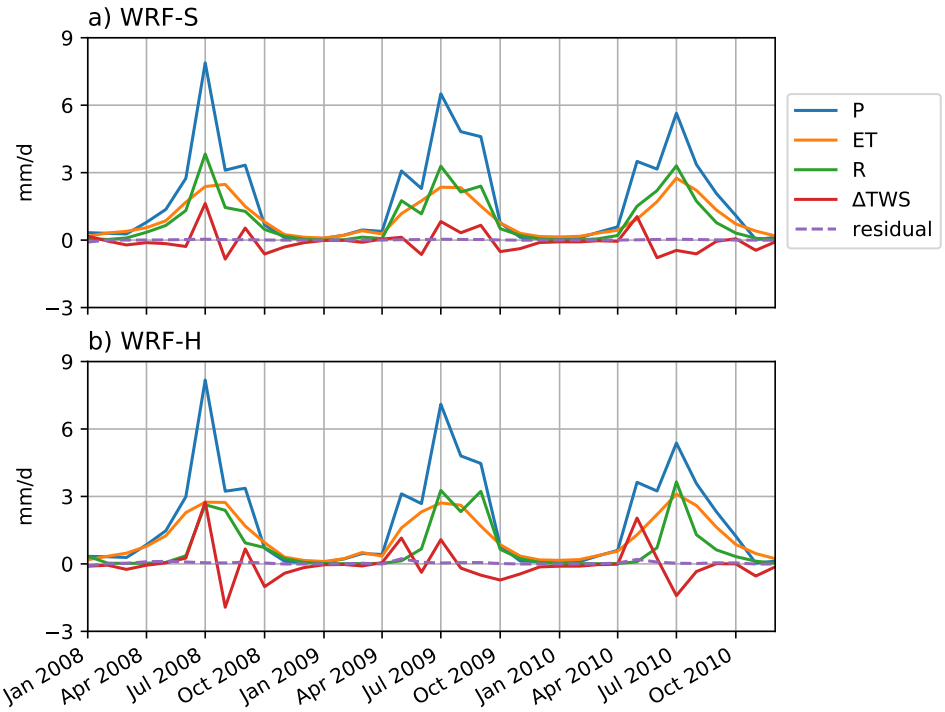

Figure 4.1: Monthly variation of terrestrial water budget components in the upper HRB as simulated in experiments of a) WRF-S and b) WRF-H.

Table 4.1: Seasonal terrestrial water budget for the upper HRB in period 2008 to 2010; units are mm·year^{-1}.

	WRF-S			WRF-H		
Season	**P**	**ET**	**R**	**P**	**ET**	**R**
Spring (MAM)	110.8	54.9	45.6	115	73.8	9.2
Summer (JJA)	405.7	201.4	209.5	422.4	238.4	173.1
Autumn (SON)	128.9	76.6	62.5	132.5	88.6	71.2
Winter (DJF)	13.6	15.7	6.37	13.9	17.8	6

The annual averaged terrestrial water balance is further calculated for two tributaries in the upper HRB (Figure 3.2), and the results are shown in Table 4.2. Regarding the water balance in the two tributaries, the east tributary has higher precipitation and evapotranspiration, and produces more runoff than the west tributary. Nonetheless,

the west tributary has a slightly higher runoff ratio with respect to the east tributary and whole upper HRB. Above characteristics are coherently simulated by both WRF-S and WRF-H experiments, and are consistent with previous research studies (e.g. Yang et al., 2015; Gao et al., 2016; Ruan et al., 2017). For the water budget differences, WRF-H prevalently simulates positive TWS changes whereas WRF-S simulates negative values, resulting in less total runoff by around 25% in WRF-H. Nevertheless, the runoff ratios of three catchments derived from WRF-H are more reasonable than those derived from WRF-S, matching to previous studies by various model approaches (e.g Gao et al., 2016; Ruan et al., 2017; Li et al., 2018a). The detail discussion on the differences of terrestrial water components are give in Section 4.3.

Table 4.2: Terrestrial water balance for the east, west tributaries and the upper HRB in period 2008 to 2010; units are mm·year^{-1}.

	Catchment	Area (km^2)	P	ET	R	R ratio	ΔTWS
WRF-S	East tributary	2,457	769	398	380.4	0.49	-9.4
	West tributary	4,585	643.4	308	351.6	0.54	-16.2
	Upper HRB	10,009	659	348.7	324.1	0.49	-13.8
WRF-H	East tributary	2,457	776.4	459.7	305.4	0.39	11.3
	West tributary	4,585	673	396.7	274.7	0.40	1.6
	Upper HRB	10,009	683.9	418.6	259.7	0.38	5.6

4.2 Atmospheric water budget for the upper Heihe river basin

Figure 4.2 displays the seasonal atmospheric water budget in the upper HRB as computed from WRF-S and WRF-H. The residual term is small to negligible (0.1%), confirming the benefit of atmospheric water budget online calculation with respect to an offline computation. The monthly atmospheric water storage (AWS) varies less than 0.3 mm/d in the summer season and nearly to zero during the winter season, which is fairly small comparing to other water component and therefore usually is neglected in regional water balance (Fersch and Kunstmann, 2014). The variation of atmospheric moisture convergence is in accordance with the variation of precipitation, reaching the peak in July and showing the lowest values in the winter season.

Computed moisture convergence values are mostly positive, indicating the horizontal net inflow converges at the mountainous area. Small and negative values of moisture convergence happen after the offset of precipitation, due to the slightly lagged evapotranspiration trigged by wet soils (Figure 4.1). WRF-S and WRF-H exhibit similar variabilities of atmospheric water components, and their differences are discussed in the next section.

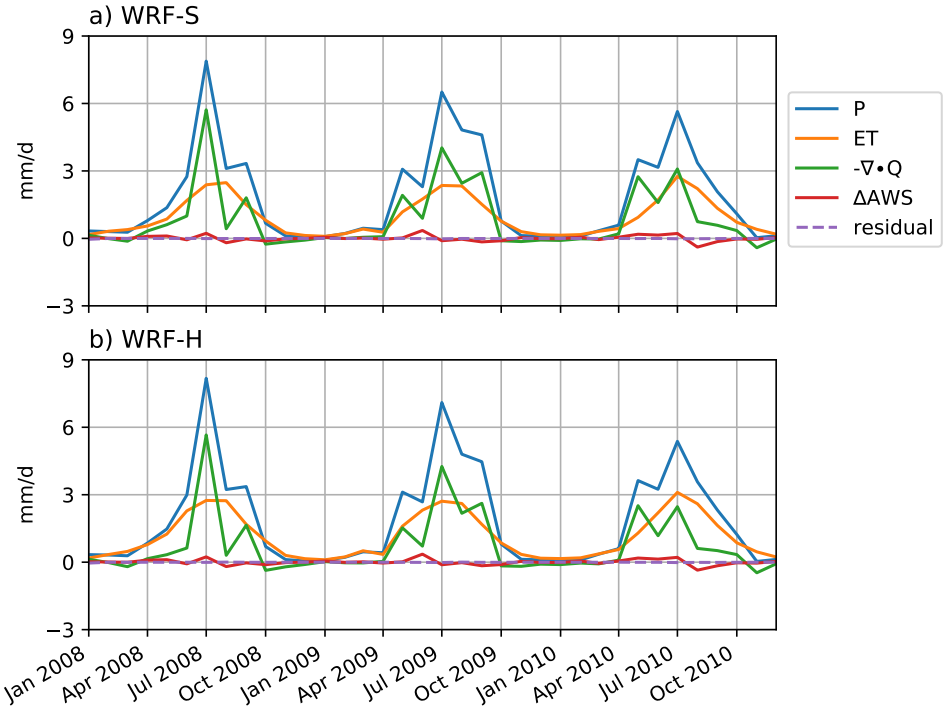

Figure 4.2: Monthly variation of atmospheric water budget components in the upper HRB as simulated in experiments of a) WRF-S and b) WRF-H.

4.3 Effect of lateral terrestrial water flow on the regional climate modeling

To detect the effects of the lateral terrestrial water flow in the fully coupled modeling, This section first compares the water components in joint atmospheric-terrestrial water balance, and then discusses the differences in regional land-atmosphere interactions.

4.3.1 Effect on joint atmospheric-terrestrial water cycle

Concerning the joint atmospheric-terrestrial water balance, the areal averaged water budget differences between WRF-H and WRF-S for the upper HRB are shown in Figure 4.3 for each simulated year. Among all the 3 years, noticeable changes induced by lateral terrestrial water flow are found in the terrestrial water budget (Figure 4.3a–d). The coherent increase of ET up to 0.6 mm/d covers the whole period, although the difference in precipitation is irregularity fluctuating. For each simulated year, Figure 4.3c shows similar differences for TWS change. The increase of TWS in WRF-H at the early wet season as well as the decrease afterwards are apparently faster than that in WRF-S. In phase opposition with the differences of TWS change, total runoff in WRF-H is decreased first (more that -1 mm/d) and subsequently slightly increased. These changes in the terrestrial water budget are related to the increase of the moisture content in the soil shown in Figure 3.6 and Figure 3.7. The faster increase of TWS in WRF-H during the early wet season is related to re-infiltration processes. Later on, the water exfiltrated from the soil caused by the subsurface routing accelerates the TWS decrease and increases the surface runoff in WRF-H. For the entire period, the total runoff amount is decreased by 20.7% in WRF-H.

In comparison to WRF-S, WRF-H slightly increases the near-surface specific humidity in the upper HRB, up to +0.3 g/kg (Figure 4.3h). In the atmospheric water budget (Figure 4.3e–h), differences in atmospheric water storage (AWS) change are negligible. The atmospheric moisture in- and outflow in the upper HRB are influenced by the ET increase at the lower surface boundary, resulting in a trend of atmospheric moisture convergence in WRF-H generally less than in WRF-S. Other regional climate modeling experiments in the semiarid region of China also found a decrease of moisture convergence caused by a local increase of ET, by considering e.g. groundwater recharge (Yuan et al., 2008) and an artificial interbasin water transfer scheme (Chen and Xie, 2010). In addition, since lateral terrestrial water flow in WRF-H is resolved in both in- and outside of the study area, and simulated ET is generally increased among the mountainous areas (Figure 3.8d), the atmospheric water budget is also affected by the atmospheric water transport outside of the analysis area (Figure 4.3g–h). In the dry winter period, the two experiments simulate similar atmospheric and terrestrial water budgets. The above differences in the atmospheric water budget indicate that the lateral terrestrial water flow does not only affect the local climate, but also influences the regional climate by changing the atmospheric

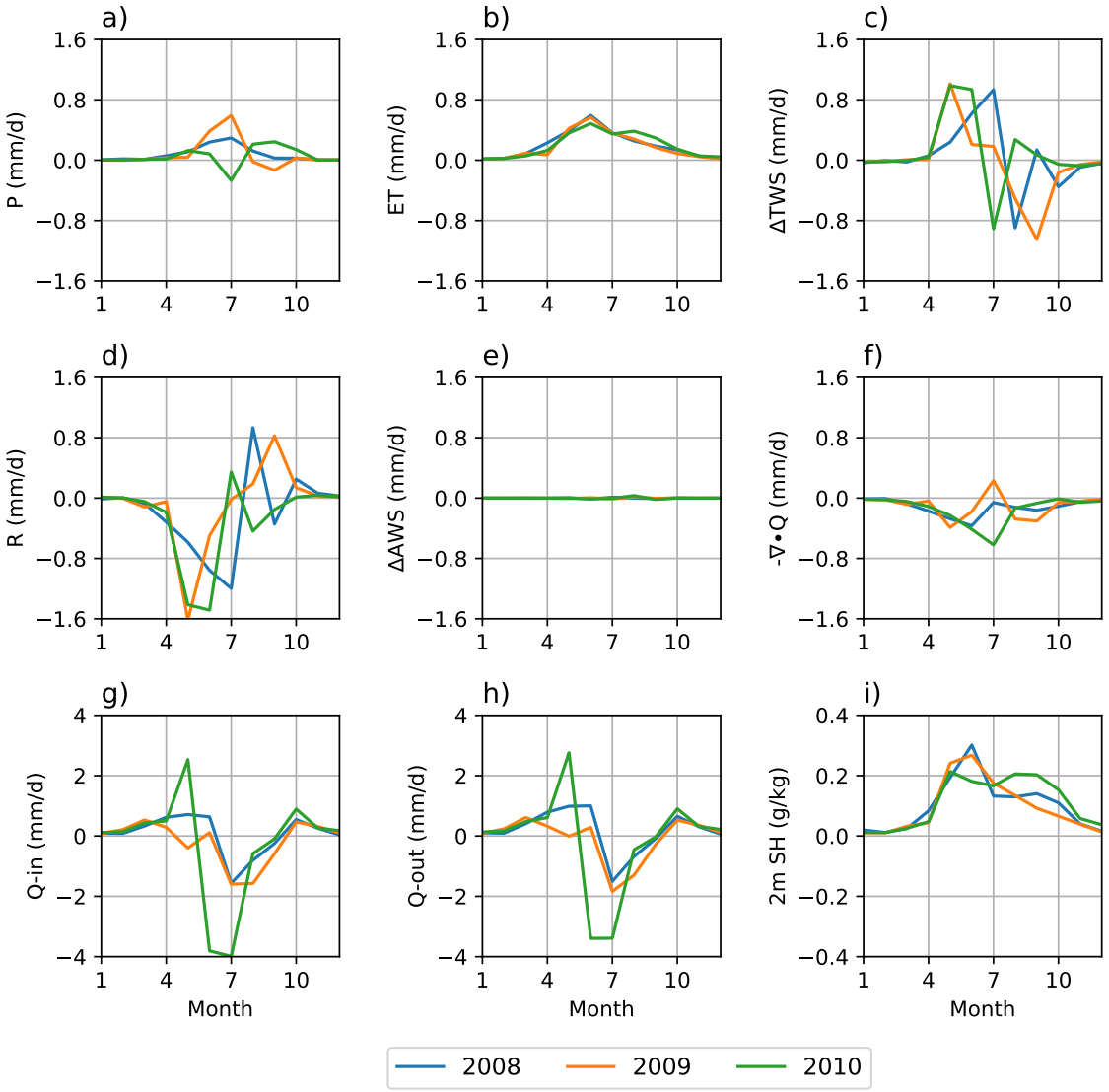

Figure 4.3: Differences (WRF-H minus WRF-S) of monthly averaged terrestrial-atmospheric water fluxes in the upper HRB in period 2008 to 2010: a) precipitation, b) evapotranspiration, c) change of terrestrial water storage, d) runoff, e) change of atmospheric water storage, f) atmospheric moisture convergence, g) inflow and h) outflow of atmospheric moisture, and i) 2-m specific humidity.

water transport.

To further explore differences between WRF-S and WRF-H, Figure 4.4 presents maps of water budget differences for the wet period from June to August 2008. Although precipitation differences exist all over the study area, the differential terrestrial water budget displays enhanced features mainly over the mountainous area. Influenced by lateral terrestrial water processes, TWS increases over most of the mountainous area

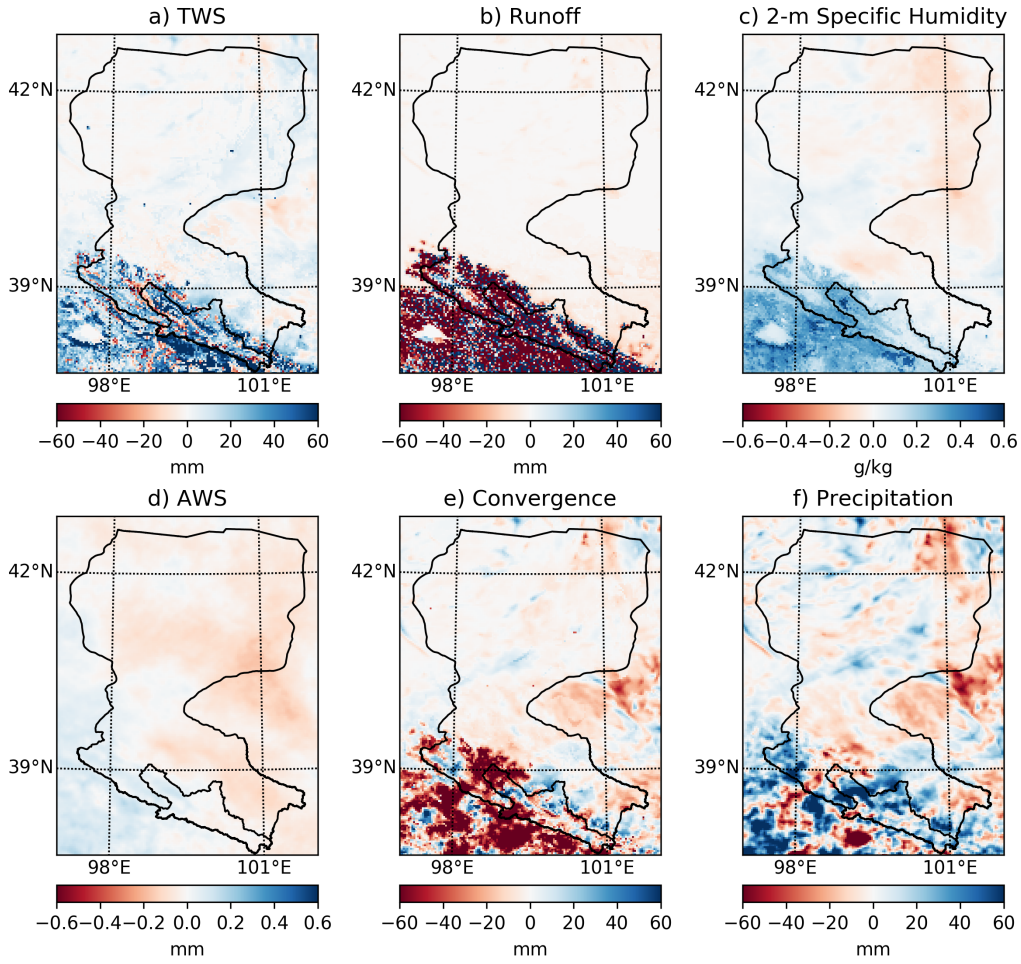

Figure 4.4: Spatial differences (WRF-H minus WRF-S) of water fluxes for the period JJA of 2008: a) mean terrestrial water storage, b) accumulated runoff, c) mean 2-m specific humidity, d) mean atmospheric water storage, e) atmospheric moisture convergence, f) accumulated precipitation.

and the total runoff decreases at non-sink areas (Figure 4.4a–b). The near-surface specific humidity increases about 0.25 g/kg in the mountains (Figure 4.4c), in relation with the distribution of ET differences, indicating the wetting effect in the mountainous area. Figure 4.4d shows that the differences of integrated water storage in the atmosphere are quite small with respect to the other terms of the water budgets. The decrease of moisture convergence tendency over the mountainous area confirms the feedback loop between terrestrial water circulation and the atmosphere. Furthermore, precipitation differences (Figure 4.4f) are largely related to the difference of atmospheric moisture convergence and divergence in the entire area (Figure 4.4e), as well as to the increase of ET in the mountainous area (Figure 3.8d).

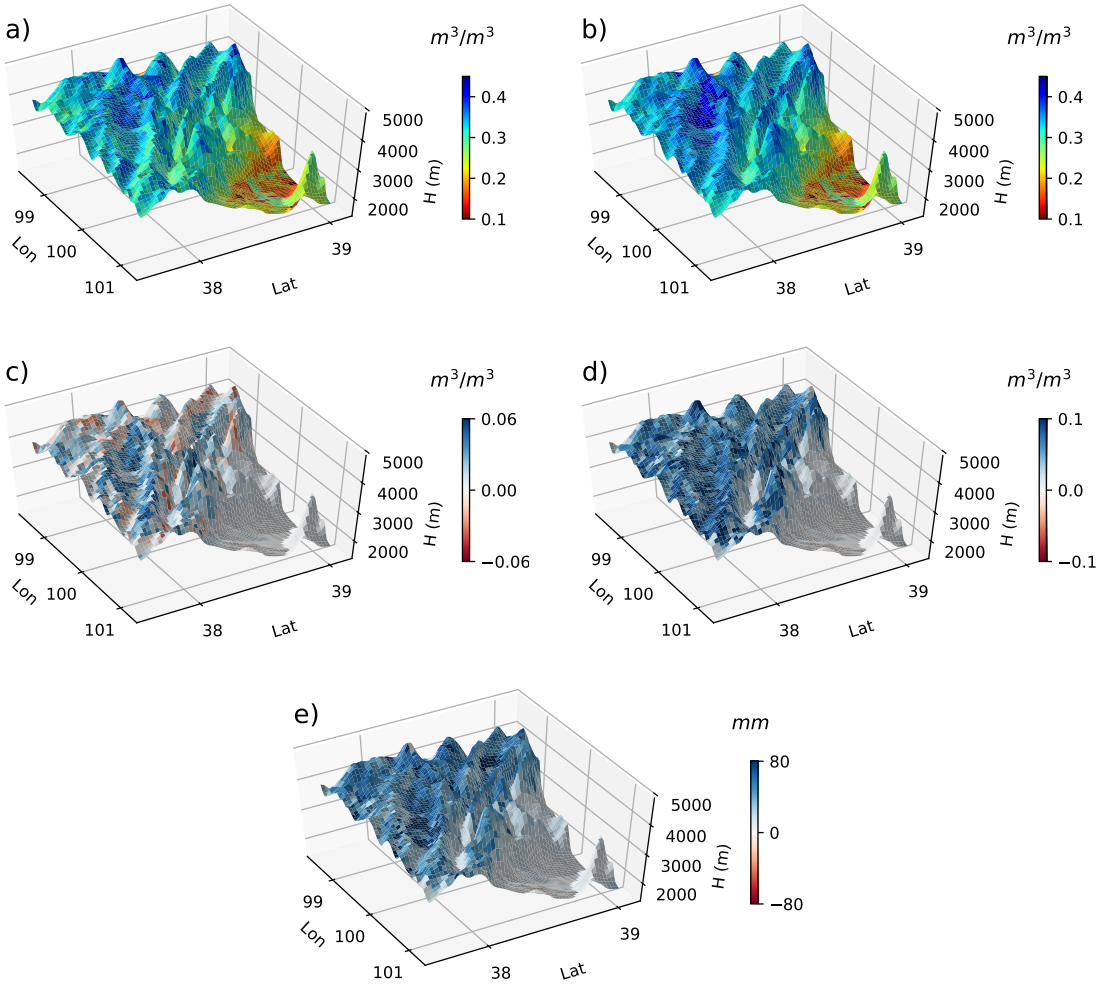

Figure 4.5: Effect of lateral flow on simulated soil moisture and evapotranspiration over the upper HRB for the period JJA of 2008: integrated 2-m soil moisture from a) WRF-S and b) WRF-H, and the differences (WRF-H minus WRF-S) for c) integrated 2-m soil moisture, d) soil moisture at root zone, and e) evapotranspiration

Figure 4.5a–c show the column integrated 2-m soil moisture of WRF-S, WRF-H and their differences over the mountainous area from June to August 2008. Figure 4.5a and 4.5b both show that the simulated soil moisture at mountains is generally higher than that at foothills or valleys, in relation with enhanced precipitation at mountain tops. As displayed in Figure 4.5c, WRF-H causes some wetter valleys and drier peaks, which is the effect of lateral subsurface water transport described by Ji et al. (2017). It is noted that this redistribution of integrated 2-m soil moisture is mainly related to the subsurface routing processed in the wetter bottom soil layer. Since this

effect is counterbalanced by the re-infiltration caused by the relatively high precipitation amount in the mountainous region, WRF-H also shows some wetter peaks in Figure 4.5c. Considering the close relationship between ET and root soil moisture (Greve et al., 2013; Seneviratne et al., 2010), soil moisture differences at root zone is also shown in Figure 4.5d. It is noted that the root soil moisture is based on vegetation description in the land surface modeling, and in this case it mainly considers one to three upper soil layers where re-infiltration processes are dominating. Therefore, the root soil moisture in WRF-H becomes much wetter than the integrated 2-m soil moisture. In the northern valleys and flat area, the differences of soil moisture are small. This is due to the lower precipitation resulting in low infiltration excess, as well as to the higher temperature resulting in higher potential ET in these areas (Figure 3.4b–c). Accordingly, lateral water flow re-infiltration processes have a reduced impact in these areas. Finally, as ET is soil moisture-limited in the arid-semiarid regions (Lu et al., 2011; Zhang and Shao, 2015), the spatial patterns of increased ET amount follow those of increased root soil moisture (Figure 4.5d–e), thus confirming the large impact of terrestrial water lateral redistribution on the hydrological cycle in mountainous areas.

4.3.2 Effect on land-atmosphere interactions

Lateral terrestrial water flow induced changes in land-atmosphere interactions are quantified with the recycling methods detailed in section 2.3.3. It is important to note that the estimated regional precipitation recycling rate depends on the specific method applied, and is sensitive to various factors including the shape, location and size of the domain of analysis, as well as the prevailing wind direction and orographic condition (Trenberth, 1999; Burde and Zangvil, 2001; Wang et al., 2018a). The bulk and E-tagging methods used in this study are aiming at investigating the changes of the land-atmosphere interactions induced by the consideration of the lateral terrestrial water flow, rather than quantifying uncertainty of estimated recycling rate caused by the well-mixed atmosphere and no return flow assumptions (Burde and Zangvil, 2001; Arnault et al., 2016a).

Figure 4.6 shows the monthly bulk recycling rate and precipitation efficiency for both HRB and the upper HRB. The calculated bulk recycling rate is up to 1.7% in summer and less than 0.5% in the winter time, generally around 1% (Figure 4.6a–b). These values are comparable with the small bulk recycling rates obtained in other

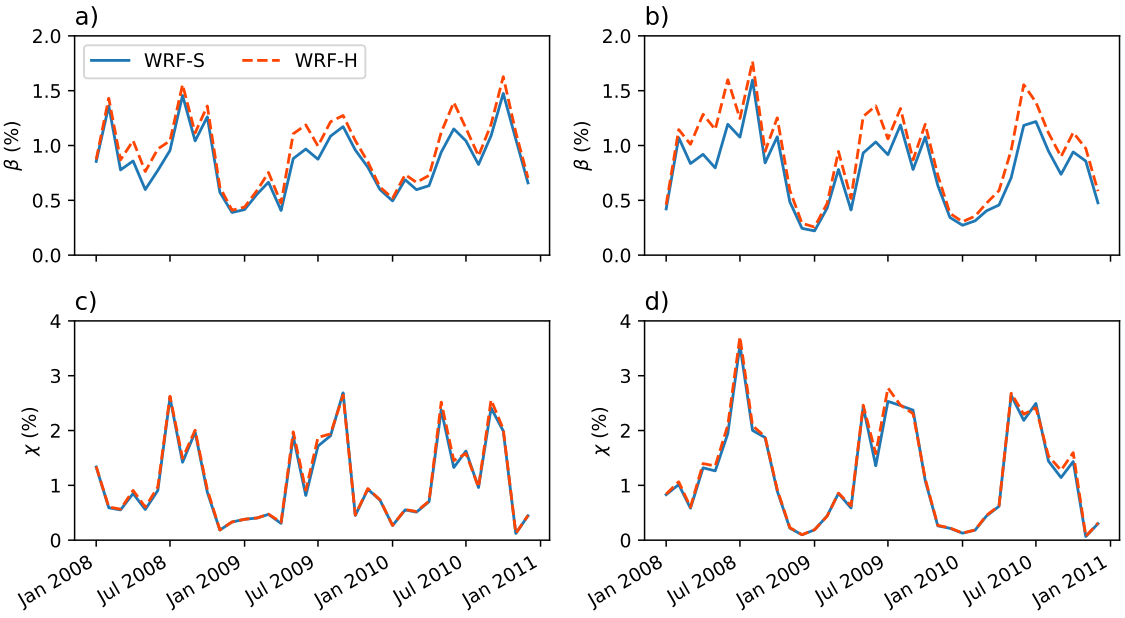

Figure 4.6: Precipitation recycling rate (a, b) and precipitation efficiency (c, d) for the HRB (a, c) and the upper HRB (b, d).

small scale semi-arid regions (e.g. Arnault et al., 2016a; Kerandi et al., 2018), and are consistent with a low bulk recycling rate for the arid region of China (Yuan et al., 2008). Results from the E-tagging method in Figure 4.7 confirm that a small amount of local precipitation originates from local ET in the upper HRB (ET_{tag}). In WRF-S, the amount of tagged precipitation (P_{tag}, precipitation originated from ET_{tag}) falling back in the source area is only 11.9 mm/year, as most of ET_{tag} is lifted in the atmosphere and flows out of the study area (Figure 4.7a). Both methods indicate that the precipitation which originates from the local ET slightly contributes to the total precipitation. The precipitation efficiency in Figure 4.6c–d ranges from 0.1% to 3.5%, and closely relates to the precipitation variation from dry to wet season. It implies that a small portion of overhead moisture influx (ET and moisture advection transport) converts to precipitation in the study area. The variation of precipitation efficiency is related to the dominant mid-latitude westerly regime, seasonal monsoon settlement in the lower atmosphere and the blocking effect of topography. Precipitation during the summertime in upper HRB is mainly related to the ascent of monsoonal moisture from southeast China by prevailing East Asian Monsoon (Wang et al., 2005; Li et al., 2015; Chen et al., 2018; Wang et al., 2018b). This effect is also revealed by the spatial pattern of tagged precipitation, as more tagged precipitation falls at the high mountain peaks around the northwestern part of the upper HRB in

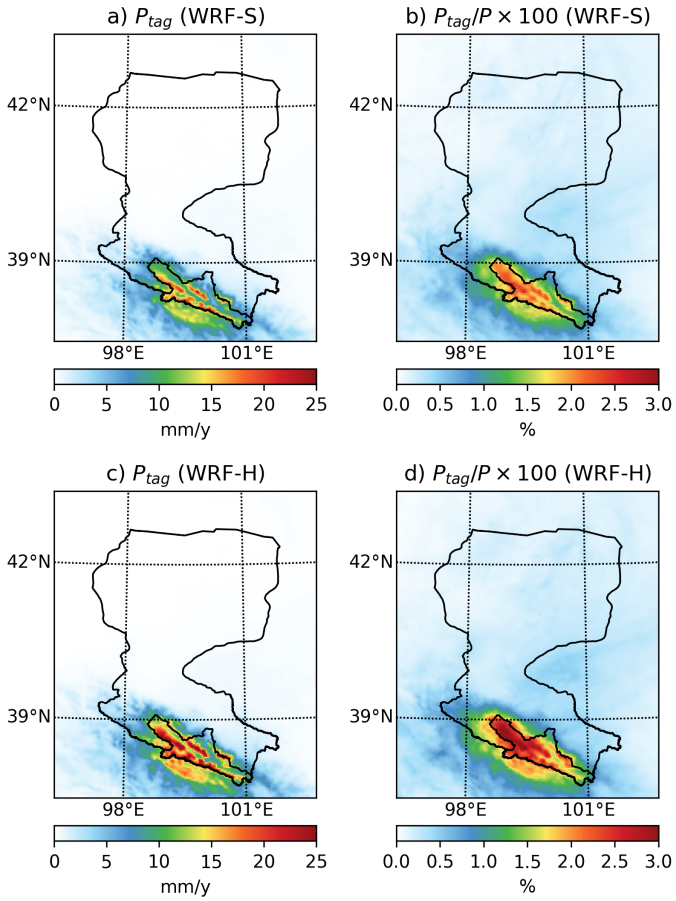

Figure 4.7: Annual total tagged precipitation (a, c) and the contribution of tagged precipitation to total precipitation (b, d) for WRF-S (a, b) and WRF-H (c, d) experiments.

comparison to the southeastern part and valley area (Figure 4.7a), resulting in higher tagged precipitation recycling in the northwest part of the upper HRB (Figure 4.7b).

With respect to the effect of lateral water flow, bulk recycling rates in WRF-H are literally higher than in WRF-S, reaching +0.4% in the rainy season, corresponding to an increase of 29%. Accordingly, there is 3.7 mm/year more tagged precipitation which falls back in WRF-H than in WRF-S. This suggests that the consideration of lateral terrestrial water flow induces a positive soil moisture-precipitation feedback in the study area, so that the induced increase of soil moisture and evapotranspiration potentially leads to an increase of local precipitation. A similar positive feedback was also found by considering a groundwater coupling (Yuan et al., 2008), and an irrigation scheme (Zhang et al., 2017) in semiarid regions of China. The precipitation efficiency does not show obvious differences between WRF-S and WRF-H

(Figure 4.6c–d). As the precipitation in the study area mostly comes from remote sources prescribed by the lateral atmospheric boundaries of the domain, the local feedback from the land surface to precipitation is accordingly small. Nevertheless, it is expected that the effect of resolving the lateral hydrological processes in RCMs would be enhanced in wetter regions with enhanced lateral terrestrial water flow, as well as in the mountainous area with higher precipitation recycling like the center Tibetan Plateau (Gao, 2017; Yao et al., 2013) and north-western India (Asharaf et al., 2012).

4.4 Summary of chapter

This chapter quantifies the joint atmospheric-terrestrial water budget for the upper HRB. Together with simulation performances showed in Chapter 3, the terrestrial water balance is captured by both WRF and coupled WRF-Hydro models. The simulated water balance and runoff ratios of two tributaries and the upper HRB are comparable with previous studies, while coupled WRF-Hydro simulates more reasonable runoff ratios in comparison to the standard WRF. By computing atmosphere moisture fluxes online at model time-step, the atmospheric water balance shows a negligible residuum. The monthly change of integrated atmosphere moisture is small, and atmosphere moisture transport is mostly characterized with moisture convergence in the upper HRB, strongly correlating with the precipitation variation.

By comparing model results between the coupled WRF-Hydro and the standard WRF model, the effect of lateral terrestrial water flow is quantified. Resolved lateral terrestrial water flow increases the soil water storage and evapotranspiration by overland flow re-infiltration processes, and subsequently redistributes the temporal runoff and decreases the annual total runoff. The terrestrial water flow-induced change of land surface conditions in mountainous area results in a slight wetting and cooling of the near-surface atmosphere, which affects the atmospheric moisture convergence through land-atmosphere interactions. The overall impact of lateral terrestrial water description on precipitation is minor, with a slight shift of spatial patterns of precipitation up to ± 5 % in the upper mountains.

Furthermore, by quantifying the land-atmosphere interactions with both the bulk recycling method and a three-dimensional E-tagging method, it is found that the contribution of local evapotranspiration to precipitation in this study area is relatively low,

indicating the limited impact of terrestrial water description on the regional precipitation as most of the precipitation is dominated by remote moisture flow. Nevertheless, the enrolled lateral terrestrial water flow description remarkably increases the recycling rate over the study area, demonstrating a clear positive feedback among lateral terrestrial water flow, soil moisture, evapotranspiration and precipitation.

5 Diurnal cycle of surface energy balance and land-atmosphere interactions

The diurnal cycle of the surface energy balance is an important indicator of land-atmosphere interactions and has noteworthy impact on climate change through the atmospheric boundary layer. Regional climate models (RCMs) are useful tools in energy flux research because of their ability in providing detailed spatial-temporal meteorological fields and their convenience in implementing sensitivity experiments to explore fundamental mechanism of weather and climate. WRF has shown its ability in reproducing the features of surface energy fluxes (e.g. Jousse et al., 2016; Erlandsen et al., 2017; Sun et al., 2017; Aas et al., 2015), and has been used in investigating the impact of land surface conditions on the surface energy balance, such as different LSMs (Smirnova et al., 2016), urban cover (Yang et al., 2012; Sarmiento et al., 2017), irrigation (Harding and Snyder, 2012). Since the land surface hydrological processes are enhanced by the WRF-Hydro model, it is relevant to evaluate the coupled model performance in simulating the diurnal surface fluxes.

This chapter evaluates the performance of the Noah-LSM conventionally used in the WRF modeling and the hydrologically enhanced Noah-LSM within the coupled WRF-Hydro modeling, for representing the diurnal cycle of atmospheric conditions and surface energy components in the study area. The following sections begin with the diurnal evaluation of the simulated hydrometeorological fields and surface energy flux measurements with available reference data sets. Then, the effect introduced by the lateral terrestrial water flow on the diurnal cycle of surface energy fluxes is shown. Finally, the spatial features of diurnal surface energy fluxes are explored.

5.1 Diurnal surface meteorological conditions

This section further evaluates the simulated surface meteorological variables against the reference data sets at the diurnal scale. Instantaneous values of 2-m air temperature, specific humidity, 10-m wind speed and precipitation rate from two experiment outputs are compared with 3 hourly CMFD reference data set. The calculated monthly correlation coefficients and the mean biases are shown in Figure 5.1.

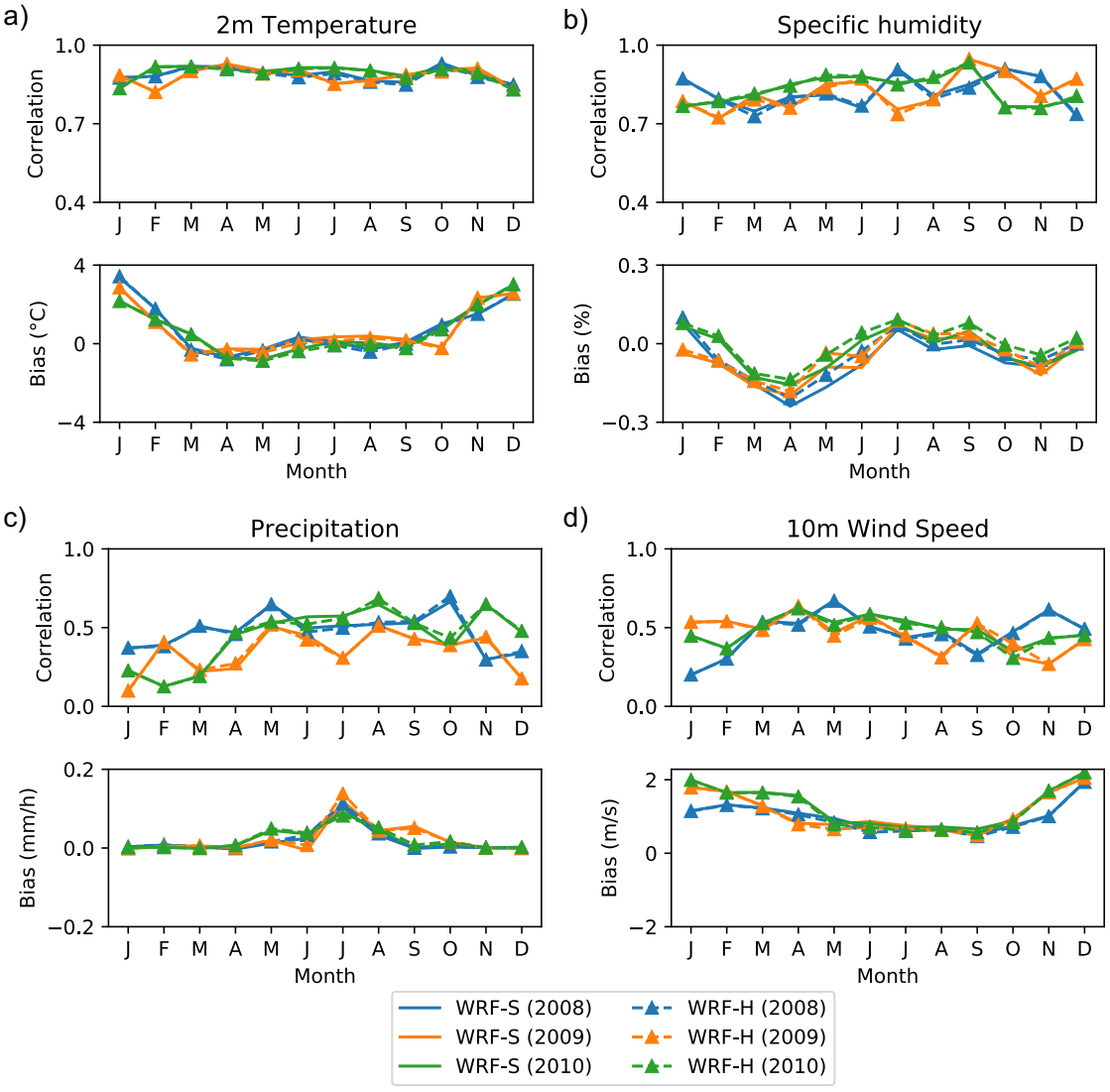

Figure 5.1: Monthly correlation and bias (WRF-S/WRF-H minus CMFD) for the diurnal 3-h values for the period 2008–2010: a) instantaneous 2-m air temperature, b) instantaneous specific humidity, c) precipitation rate and d) instantaneous 10-m wind speed.

The monthly correlation coefficients for 2-m air temperature all exceed 0.8 for both WRF-S and WRF-H experiments during the simulation period. The mean temperature biases of the simulations are mostly within ±1℃ from May to October and approximately reaching up to +3.5℃ at the winter season (Figure 5.1a). Figure 5.2a further shows the monthly-averaged time series of hourly observed and simulated 2-m air temperature at two in-situ stations. At the high-altitude Arou station, the two models well simulate the diurnal variation of temperature in the summertime as well as the daytime temperature in the winter season (October to March). However, both models overshoot the air temperature during the nighttime in the winter season, resulting in the smaller magnitude of diurnal variation than the observed temperature. At the Guantan station, air temperature at the noontime is slightly overestimated. Nevertheless, comparisons show that the diurnal variation of surface air temperature is well reproduced in the summertime, which confirms the small variation divergence with respect to hourly observed records (Figure 5.2b) and small biases and high correlation with respect to the gridded reference (Figure 5.1a).

The specific humidity also shows a close correlation with the CMFD reference data set (Figure 5.1b). The calculated correlation coefficients are above 0.7 and the mean biases are ranging from -20% to 10%.

For precipitation, the correlation coefficients are mostly between 0.1 and 0.6 (Figure 5.1c). Lower correlation is found in the dry season, whereas the mean biases are very small. The lower correlation coefficient obtained for the dry season is mainly due to the fact that the models could not well represent some short time and small precipitation events. In the summertime, the overestimation of precipitation shows positive biases of about +0.1 mm/h. Nevertheless, the moderate correlation coefficients around 0.5 suggest that the diurnal precipitation variation is reasonably well captured by the two modeling approaches.

The correlation of wind speed is mostly between 0.4 to 0.6, with no clear seasonal patterns (Figure 5.1d). The monthly biases are exclusively positive, ranging from 0.5 m/s during the summertime to nearly 2 m/s in December and January. This positive bias may be related to local conditions not well represented in the coarse reference data set. The surface pressure, which is not shown in the figure, displays a correlation above 0.95 for all months.

The above simulated surface meteorological fields are found to be in reasonable agreement with respect to the reference data sets, especially during the summertime. Air

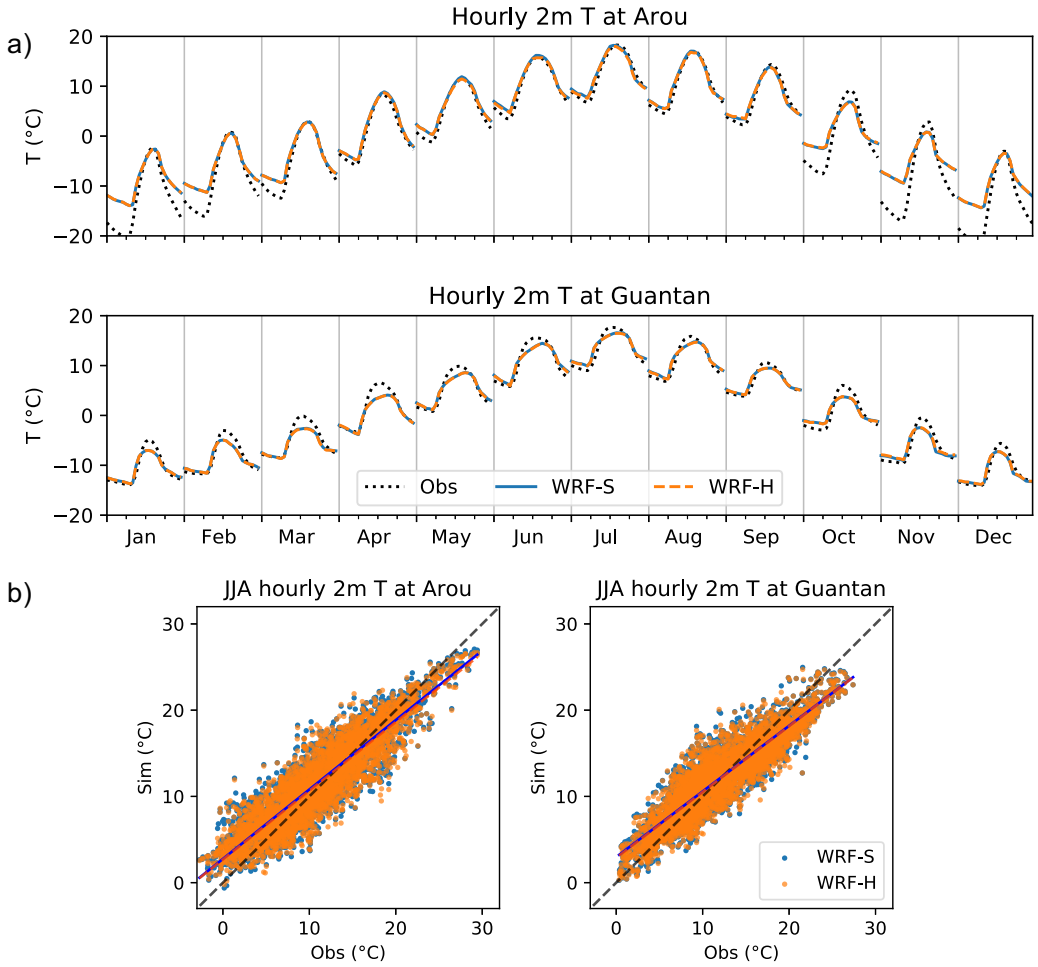

Figure 5.2: a) Monthly-averaged diurnal variations of 2-m air temperature from WRF-S, WRF-H, and station observation at Arou and Guantan stations in the period 2009–2010. The interval marks on the x-axis of each month are 0, 6, 12, 18 hour of the local time. b) Scatter plot of hourly 2-m air temperature of WRF-S and WRF-H versus observation at Arou and Guantan stations in the period JJA of 2008 and 2009.

temperature and wind speed correlation and biases in WRF-S and WRF-H are close in their values. Larger differences between the two models occur for specific humidity and precipitation, suggesting the diurnal variation of surface moisture fluxes are affected by lateral terrestrial water flow.

5.2 Analysis of the diurnal cycle of surface energy components

Diurnal variation of simulated surface energy components is evaluated with turbulent flux measurements from EC towers at Arou and Guantan stations in hourly scale. The turbulent fluxes (latent and sensible heat fluxes) measured by the EC towers are processed to 30-minute values with partial gaps primarily due to weather and sensor failures. The fluxes gaps within 4 hours are filled with the marginal distribution sampling method (Reichstein et al., 2005) and resampled at the hourly scale. Figure 5.3 and 5.4 show the hourly comparison of measured and simulated net radiation flux (Rn), latent heat flux (λE) and sensible heat flux (H) at Arou and Guantan stations, respectively. At Arou station, the hourly time series for July 2009 indicate that the observed magnitudes of Rn and λE are well captured by the models, with Rn around 700 W/m^2 and of λE less than 500 W/m^2, whereas the magnitude of H is overestimated. In Guantan station for the period June of 2010, the models simulate reasonable magnitude of λE and H, whereas they underestimate Rn during the noontime. Nevertheless, the observed interdaily variations of the energy fluxes caused by the cloudy and clear weather conditions are well reproduced in both WRF-S and WRF-H (Figure 5.3 and 5.4).

Figure 5.3 and 5.4 also display the diurnal variation of Rn, λE and H as hourly averaged values with ± 0.75 standard deviations over the considered one-month period (July 2009 and June 2010). The diurnal patterns of the surface energy fluxes are well captured in model simulations, with comparable averaged values and uniform increase and decrease tendencies related to solar rising and setting. The simulated hourly averaged Rn is fairly comparable with the observations, with mean values at noon ca. 500 W/m^2 at Arou station and >600 W/m^2 at Guantan station. However, the simulated λE and H are generally higher than those observed at both two station sites, with mean values of >50 W/m^2 for λE and >70 W/m^2 for H, respectively. This disparity between modeled and observed turbulent fluxes could partly be acknowledged by the uncertainties in EC measurement. The EC measured turbulent fluxes usually suffer from the energy balance closure problem, with a residual imbalance generally between 10% to 30% (Stoy et al., 2013; Foken, 2008), whereas the energy balance is closed in the model simulations. Specific to the two EC towers in Arou and Guantan stations, the residual in measured energy fluxes balance is found to be about

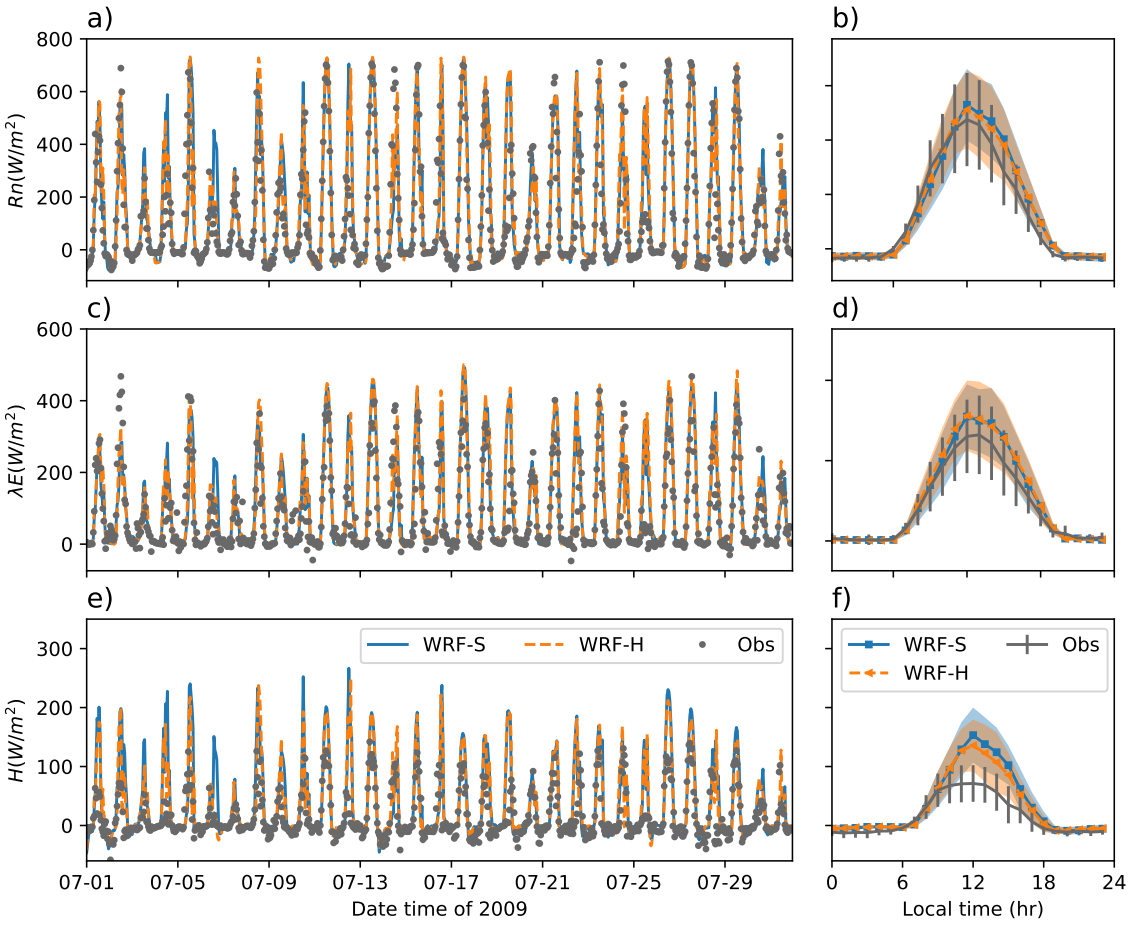

Figure 5.3: Hourly time series of a) net radiation flux (Rn), c) latent heat flux (λE) and e) sensible heat flux (H) at Arou EC station during July of 2009. (b, d, f) Diurnal variations of surface energy fluxes (Rn, λE, H), with mean values shown as symbols and shading representing ± 0.75 standard deviation.

16% and 21% in the summertime, respectively (Liu et al., 2011). The lack of energy balance closure generally suggests a possible underestimation of the λE and/or H (Twine et al., 2000; Liu et al., 2011; Ma et al., 2019). Additional uncertainties may arise from the comparison of measured turbulent fluxes to the 3-km model grid values, as the flux footprint of Arou and Guantan EC towers are primarily representative of an area with a radius of 250 m (Liu et al., 2011).

Figure 5.5 shows the areal averaged hourly precipitation, net radiation flux Rn, latent heat flux λE, sensible heat flux H and ground heat flux G in the upper HRB as a function of the day of the year, for exploring the diurnal cycle features of the surface energy fluxes. The diurnal cycle is shown from April to October of 2008, containing the onset and the retreat period of the East Asian summer monsoon. The

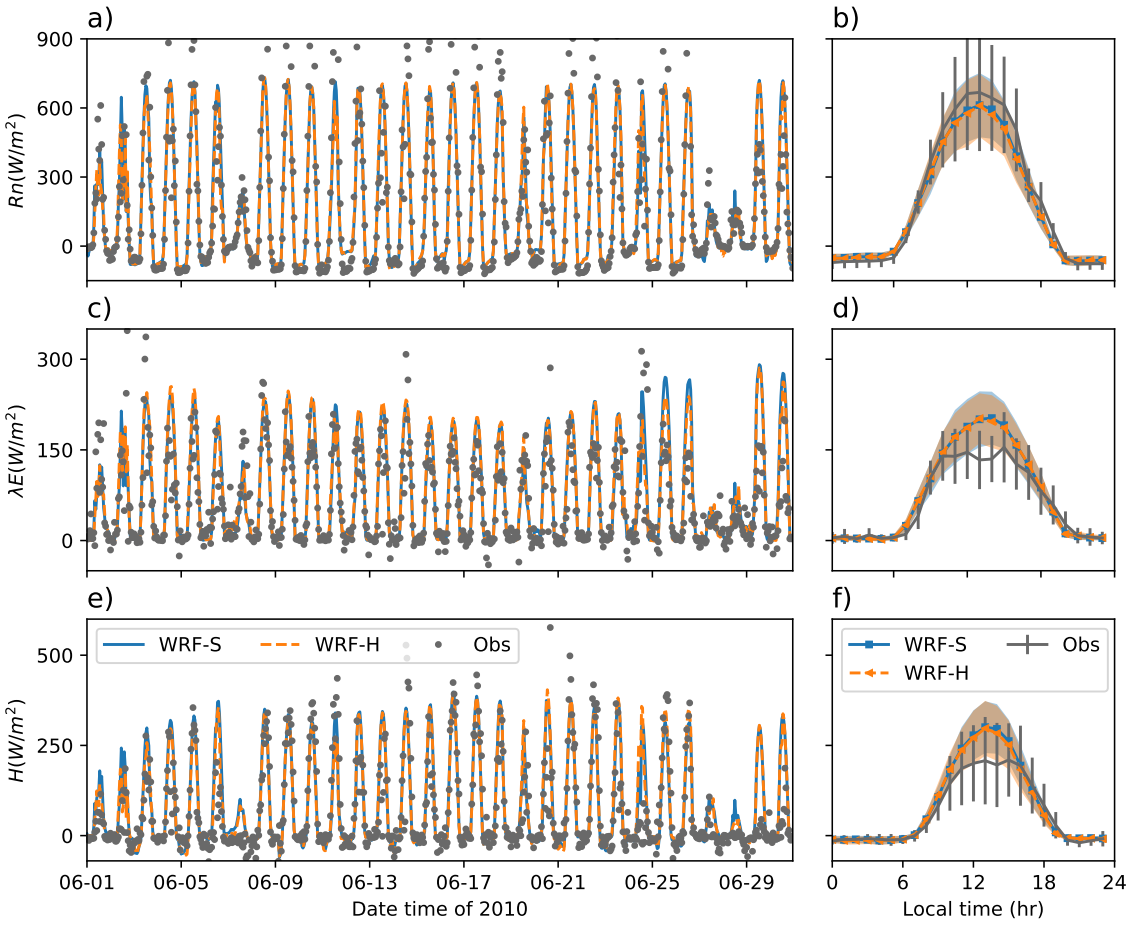

Figure 5.4: Hourly time series of a) net radiation flux Rn, c) latent heat flux λE and e) sensible heat flux H at Guantan EC station during June of 2010. (b, d, f) Diurnal variations of surface energy fluxes, with mean values shown as symbols and shading representing ±0.75 standard deviation.

monthly-averaged diurnal cycle of the above energy fluxes is additionally shown in Figure 5.6 for the rainy season months. According to Figure 5.5a, the simulated summer precipitation exhibits favorable occurrences in the late afternoon and early morning, with a minimum at noon, which is consistent with previously observed diurnal precipitation pattern in this area (e.g. Liu et al., 2017; Li and Yang, 2017; Li et al., 2019). A clear shift of diurnal shape and the magnitude of the surface fluxes is shown at the beginning of June due to the monsoon onset, with an observed increase of λE and decrease of H and G (Figure 5.5c–e). As shown in Figure 5.6 for the rainy season months, the mean nocturnal values of λE and H are stable and close to zero. Rn increases dramatically during the day and peaks at noontime. Visibly, G takes a lead of the increase in the morning and reaches its peak earlier than Rn, λE and H,

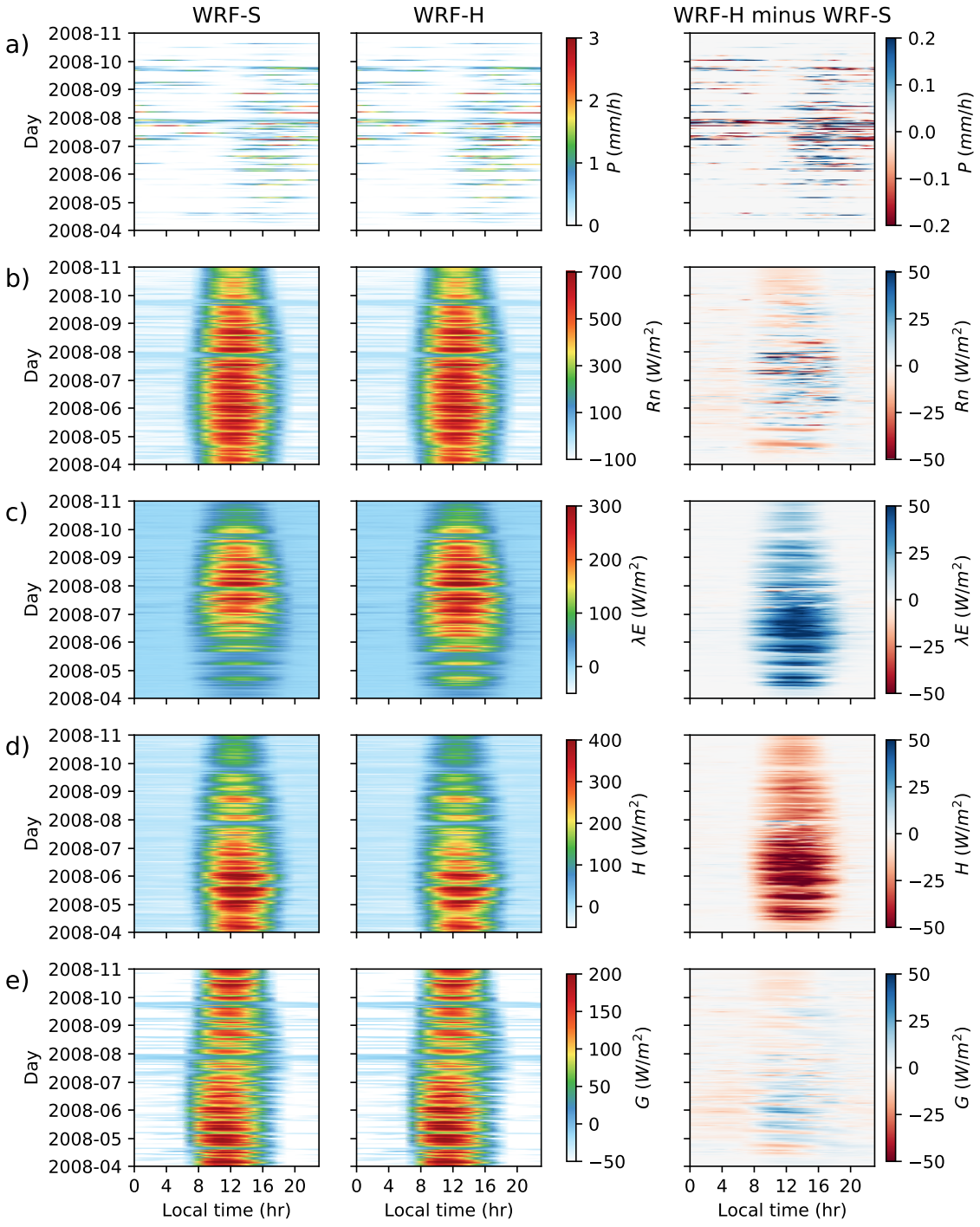

Figure 5.5: Local time – day Hovmöller diagram displaying the diurnal cycle of the areal averaged a) precipitation, b) net radiation flux Rn, c) latent heat flux λE, d) sensible heat flux H and e) ground heat flux G spatially averaged for the upper HRB from WRF-S (left column) and WRF-H (middle column), and their differences (middle column).

then it decreases gradually, with a stable and negative values at night. On average, the turbulent fluxes show distinct differences among the months. In both WRF-H and WRF-S, the monthly-averaged peak value of λE in July and August (>200 W/m^2) is generally higher than in June, although the monthly averaged Rn and H show their maximum values in June (Figure 5.6b–c). This change of the dominant turbulent flux suggests that λE in the study area is controlled by the water-limited condition rather than by radiation condition, which is characteristic for a semi-arid area. From September on, both Rn and λE are decreasing due to the reduction of available energy (Figure 5.5c–d). The above energy budget features are consistent with a prior measurement study in this area (Liu et al., 2011). Furthermore, Figure 5.5 highlights that the diurnal cycle of λE and H is actively controlled by Rn, as well as by the occurrence of precipitation events.

Regarding to the difference between WRF-H and WRF-S, Figure 5.5 shows that Rn and G in the two simulations slightly differ in their areal averaged values, which is due to the simulated weather condition differences between WRF-H and WRF-S. Accordingly, the monthly average diurnal cycles of Rn and G from the two models show small to negligible differences (Figure 5.6). This suggests that nearly the same amount of available energy ($Rn-G$) is simulated by the two models. Large differences are found in the turbulent fluxes between WRF-S and WRF-H. When the lateral terrestrial water is considered in WRF-H, λE in the daytime is notably higher than in WRF-S, and H is accordingly lower (Figure 5.5). The monthly averaged diurnal turbulent fluxes show differences in the peak values between WRF-S and WRF-H, reaching a maximum ca. 50 W/m^2 in June, and a minimum ca. 15 W/m^2 in September (Figure 5.6). Nevertheless, the peak time of the diurnal turbulent fluxes in the two simulations is not changed.

The above differences between WRF-S and WRF-H express that the laterally moved and re-infiltrated surface runoff modifies and redistributes the energy partition of available energy at the diurnal scale. At the EC tower points, the differences of the diurnal surface energy fluxes between WRF-H and WRF-S are concealed. Differences in the hourly values are related to differences in the simulated atmosphere conditions, although all the surface energy fluxes in WRF-S and WRF-H show similar diurnal mean values and standard deviation (Figure 5.3 and 5.4). The spatial distribution of the surface energy fluxes is shown in the next section.

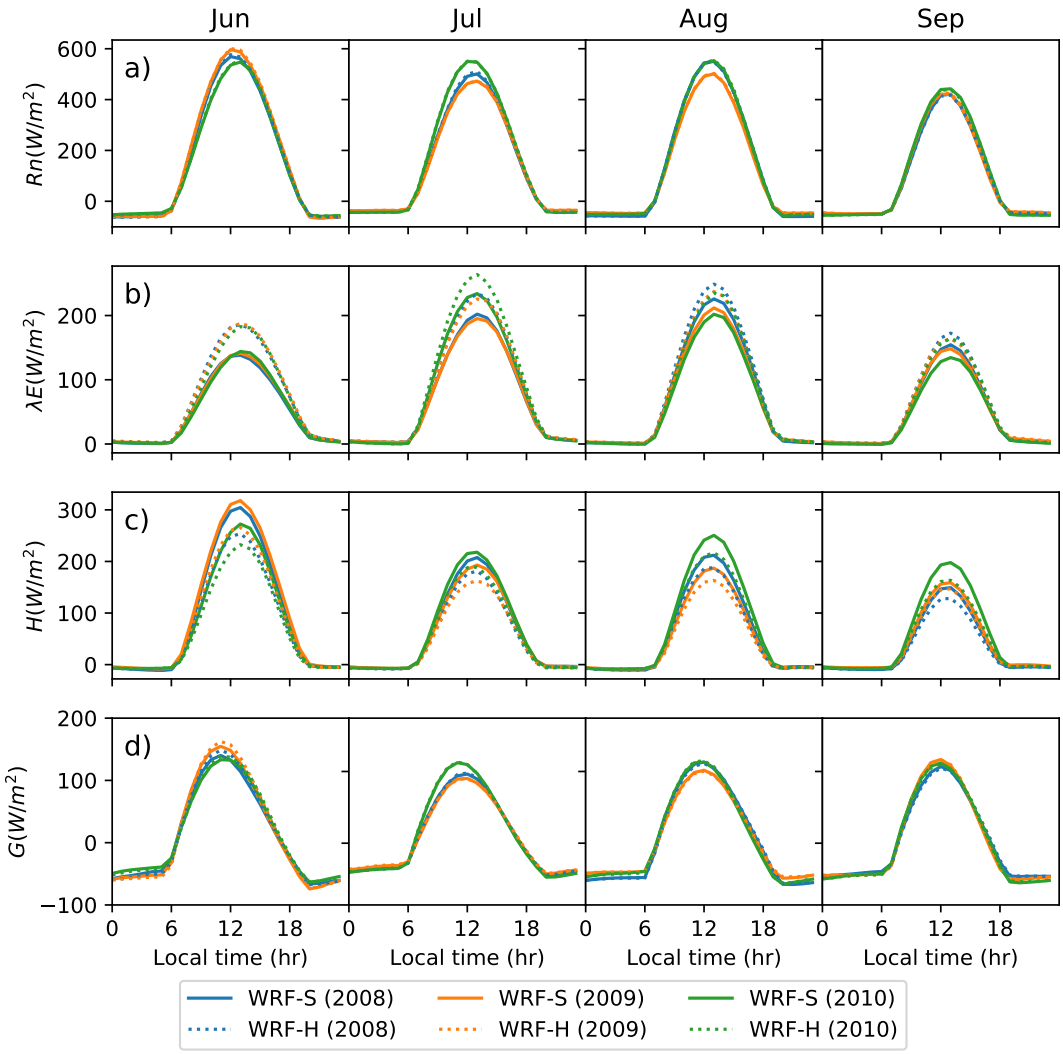

Figure 5.6: Monthly-averaged diurnal variations of a) net radiation flux Rn, b) latent heat flux λE, c) sensible heat flux H and d) ground heat flux G spatially averaged for the upper HRB simulated by WRF-S and WRF-H for the period JJAS of 2008, 2009 and 2010.

5.3 Diurnal spatial signatures of surface energy budgets

The spatial signatures of the diurnal cycle of surface energy budgets are suitable for understanding the effect of topography, vegetation and soil features captured in the coupled modeling (Xiang et al., 2017). Since prior sections showed that lateral terrestrial water flow influences the water budget and regional turbulent fluxes, it would be expected that the spatial variations of the diurnal energy fluxes are also

impacted to some extent. Figure 5.7 presents the spatial pattern of the mean diurnal peak values, as well as the peak times of surface energy fluxes for the wet period from June to August 2008 in the upper HRB and its surrounded area. Comparing Figure 5.7 with Figure 3.2, Rn in high mountain peaks is lower than it in the valley and the flat area, due to the high elevation snow cover (Minder et al., 2016; Yu et al., 2017). The diurnal peak time of Rn shows a slight spatial variability, close to local noontime. The peak values of λE and H exhibit a close relationship with vegetation type, with high values of λE in vegetation covered area (grassland and cropland shown in Figure 3.1a) among the high mountains. In addition, λE in the southeast part of the mountain area is generally higher than it in the northwest part due to the spatial variability of precipitation.

The above shown pattern of λE is consistent with the findings of Gao et al. (2016), that the highest actual evapotranspiration occurs around intermediate to higher elevation ecosystems in the study area. In comparison, the higher peak H is featured in the relative flat terrain in the middle HRB and in the valley area in the upper HRB. The peak times of λE and H notably depend on the description of vegetation types, with a clear delay towards the afternoon over barren area. The peak G show the high values at barren area and low values at the vegetated covered mountainous area, which is comparable with the spatial distribution of G estimated from multiple remote sensing data (Li et al., 2017b). The peak time of G displays a distinct relation with topography, with an apparent delay at the mountain tops with respect to the flat area.

Lateral terrestrial water flow parameterized in WRF-H shows a negligible impact on the spatial distribution of Rn and the peak values of G (Figure 5.7a, b, g), whereas it slight delays the peak time of G in mountain peaks (Figure 5.7h). The peak values of λE and H are notably modified by lateral terrestrial water flow, showing the increase of λE and decrease of H in the mountainous area. However, the differences of diurnal peak time are inconsiderable.

Above results show the significant effect of land heterogeneous surface on the spatial pattern of energy fluxes, primary the vegetation ecosystems. The lateral terrestrial water flow modifies the magnitude of diurnal spatial turbulent fluxes, and has limited impact on diurnal peak time appearance of surface energy fluxes in the study area.

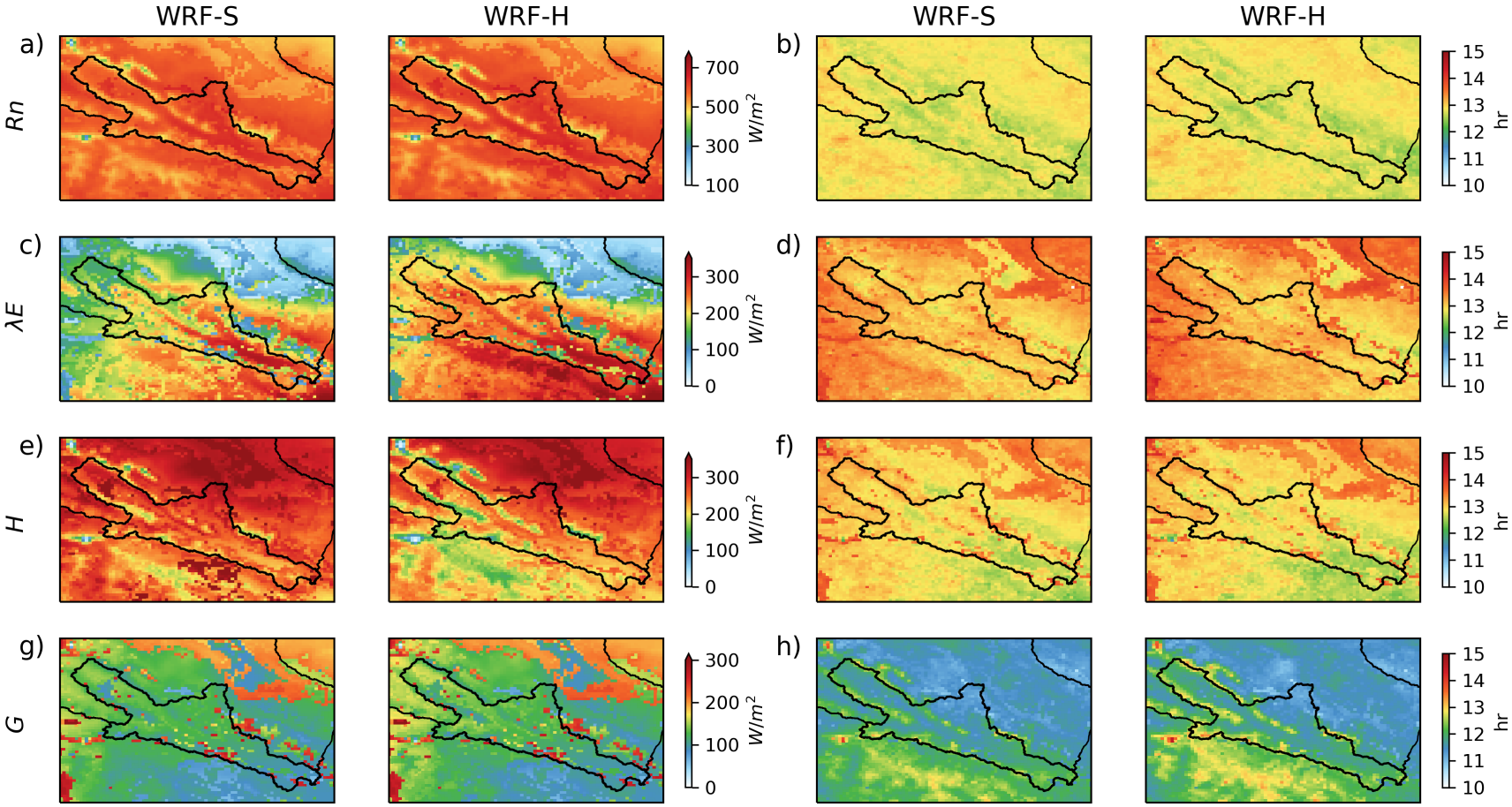

Figure 5.7: Spatial distribution of diurnal maximum value (a, c, e, g) and peak time (b, d, f, h) of net radiation flux Rn (a, b), latent heat flux λE (c, d), sensible heat flux H (e, f) and ground heat flux G (g, h) for the period June to August of 2008.

5.4 Summary of chapter

In this chapter, the diurnal variation of surface energy fluxes in the upper HRB is investigated by coupled WRF-Hydro and standard WRF model simulations. Impact of lateral terrestrial water flow on land-atmosphere interactions is evaluated by intercomparing the diurnal energy fluxes between coupled WRF-Hydro and WRF simulations. After assessing the models performances against observational data sets, the spatial distributed peak values and time of surface energy fluxes are presented to identify the diurnal spatial signatures and their potential link with land surface conditions.

In general, both WRF and coupled WRF-Hydro reasonably simulate the diurnal variation of surface meteorological fields including air temperature, specific humidity, precipitation and wind speed, in comparison to the reference data sets. The simulated hourly surface energy fluxes are comparable with EC tower observation during the summertime, indicating the equitable model ability on the representation of the diurnal energy fluxes magnitude and variation. The spatial patterns of diurnal surface energy fluxes are distinctly impacted by the land heterogeneous surface, in relation to the diversity of vegetation ecosystem. Both in spatial and temporal scale, the lateral terrestrial water flow-induced land condition change results a towards increase of diurnal latent heat flux and a decrease of diurnal sensible heat flux, although the net radiation and ground heat fluxes remain almost unchanged. Nevertheless, the lateral terrestrial water flow has a little impact on diurnal peak time appearance of surface energy fluxes.

6 Sensitivity of the land-atmosphere feedbacks with respect to the PBL scheme

Uncertainties in regional climate modeling are broadly related to model physics parameters (e.g. configuration setup, land surface parameters), internal model variabilities (e.g. initial, lateral and lower boundary conditions) and external forcing (Crétat et al., 2012; Klein et al., 2015; Laux et al., 2017). The planetary boundary layer (PBL) schemes depict unresolved turbulent vertical fluxes of momentum, heat and moisture from land surface throughout low atmosphere. Therefore, it is pivotal to atmosphere modeling applications. The represented PBL dynamics in atmospheric modeling through the turbulence parameterization, affects the simulated meteorological system. For example, the excessive turbulent mixing could lead to PBLs which are too warm, dry and thick, whereas low turbulent mixing usually leads to too cold, moist and shallow PBLs (Hu et al., 2010). By extensively evaluating and intercomparing the PBL schemes in the MM5 and WRF models (e.g. Braun and Tao, 2000; Jankov et al., 2005; Cohen et al., 2015; Shin and Dudhia, 2016), it is known that PBL schemes have a broad impact on the atmospheric modeling performance and land-atmosphere interactions.

Above chapters have showed the impact of lateral terrestrial water flow in the regional water balance and land-atmosphere interactions. It is important to identify whether these effects are sensitive to other model parameterizations, such as the PBL scheme. In this chapter, an ensemble of WRF and coupled WRF-Hydro simulations is further implemented by varying the PBL schemes for three continuous years, aiming at 1) showing uncertainties of model performance in hydrometeorological variables simulation, and in particular 2) investigating the sensitivity of quantified land-atmosphere interactions with respect to PBL scheme and lateral terrestrial water flow. The land-atmosphere interactions are quantified by land-precipitation feedback

processes, three-dimensional atmospheric moisture tracing method (E-tagging) and regional precipitation recycling analysis.

6.1 Experimental design of PBL parameterization

In order to ascertain whether the quantified land-atmosphere interactions characters are sensitive to the change of PBL parameterization, three different PBL schemes are considered for the turbulence parameterization. Besides the Asymmetric Convective Model version 2 (ACM2) PBL scheme already experimented in Chapter 2, two additional frequently used schemes Yonsei University (YSU) of Hong et al. (2006) and Mellor–Yamada–Janjic (MYJ) of Janjić (1994) are carried out in this chapter. Accordingly, there are 6 members in total, that is, a 3-member standard WRF PBL ensemble (WRFS-ENS) and 3-member coupled WRF-Hydro PBL ensemble (WRFH-ENS). It is noted that the model setup used in the new experiments is the same as the one described in Chapter 2, except for the PBL scheme.

The above three PBL schemes are chosen as they have already been extensively considered in turbulence parameterization uncertainty in WRF simulations (e.g. Hu et al., 2010; García-Díez et al., 2013; Gómez-Navarro et al., 2015) and coupled WRF-Hydro simulation (e.g. Arnault et al., 2018). The used PBL schemes differ in representing mixing on a local and non-local basis. The YSU scheme is a first-order scheme which uses non-local eddy diffusivity coefficient to explicit turbulent fluxes. The MYJ scheme is a local closure scheme of 1.5-order with a prognostic equation for the turbulent kinetic energy. ACM2 uses a combination of local downward mixing and non-local upward convective mixing. The detailed sensitivities of these PBL schemes in WRF modeling have been broadly evaluated and investigated (e.g. Xie et al., 2012; García-Díez et al., 2013; Cohen et al., 2015). In this chapter, it mainly focuses on the sensitivity of the quantified land-atmosphere interactions within the WRF and coupled WRF-Hydro models.

Figure 6.1 provides a schematic view of the ensemble members. When intercomparing the ensemble members, the horizontal comparison (orange line) indicates the model sensitivity related to PBL scheme, and the vertical comparison (blue line) expresses the sensitivity related to lateral terrestrial water flow.

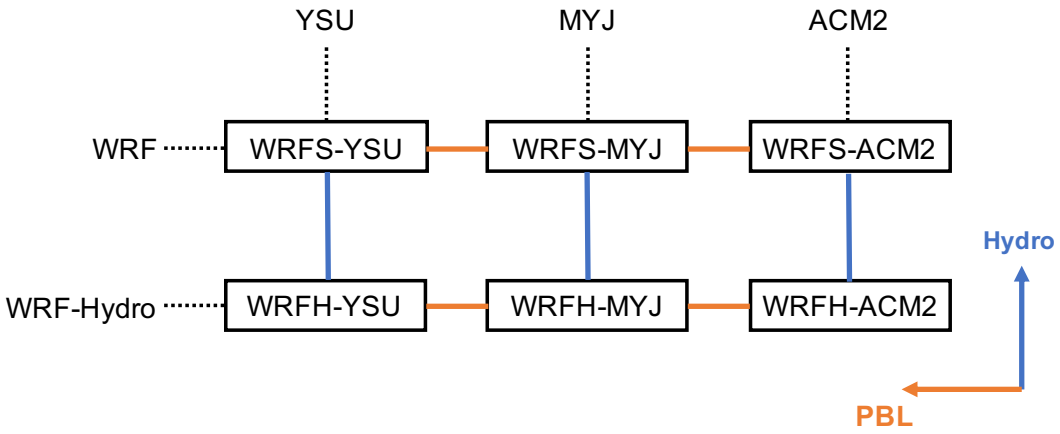

Figure 6.1: Schematic view of ensemble members described in section 6.1. The member is named by the used model [WRF standard (WRFS-) and coupled WRF-Hydro (WRFH-)] with the used PBL scheme.

6.2 Sensitivity of simulated hydrometeorological variables

The spatial pattern of the mean values of 2-m air temperature, precipitation, and evapotranspiration from the model ensemble WRFS-ENS and WRFH-ENS, as well as the differences are shown in Figure 6.2. Figure 6.3 shows the areal-averaged time series of these monthly averaged values in the upper HRB. For both WRFS-ENS and WRFH-ENS, the air temperature, precipitation, and evapotranspiration show a reasonable spatial pattern with respect to the reference data set (Figure 3.4a,e and Figure 3.8a), and comparable seasonal variations (Figure 6.3). Ensemble results show that the simulated hydrometeorological variables are sensitive to the different PBL schemes, i.e. the areal-averaged precipitation uncertainty can reach 0.5 mm/d in the rainy season. It is noted that the evapotranspiration is irrespectively increased by the lateral terrestrial water flow in WRFH-ENS. However, although the lateral terrestrial water flow is enrolled, WRFH-ENS does not show additional precipitation and temperature uncertainties with respect to WRFS-ENS.

Simulated daily streamflow from the WRFH-ENS ensemble is shown in Figure 6.4. Generally, the ensemble members simulate comparable temporal variation of streamflow, with an underestimation in dry season and overestimation in rainy season. In total, the simulated streamflow amount is overestimated by 20%–29% in Yingluoxia gauge for the three-year period, in which the MYJ PBL shows largest bias. The

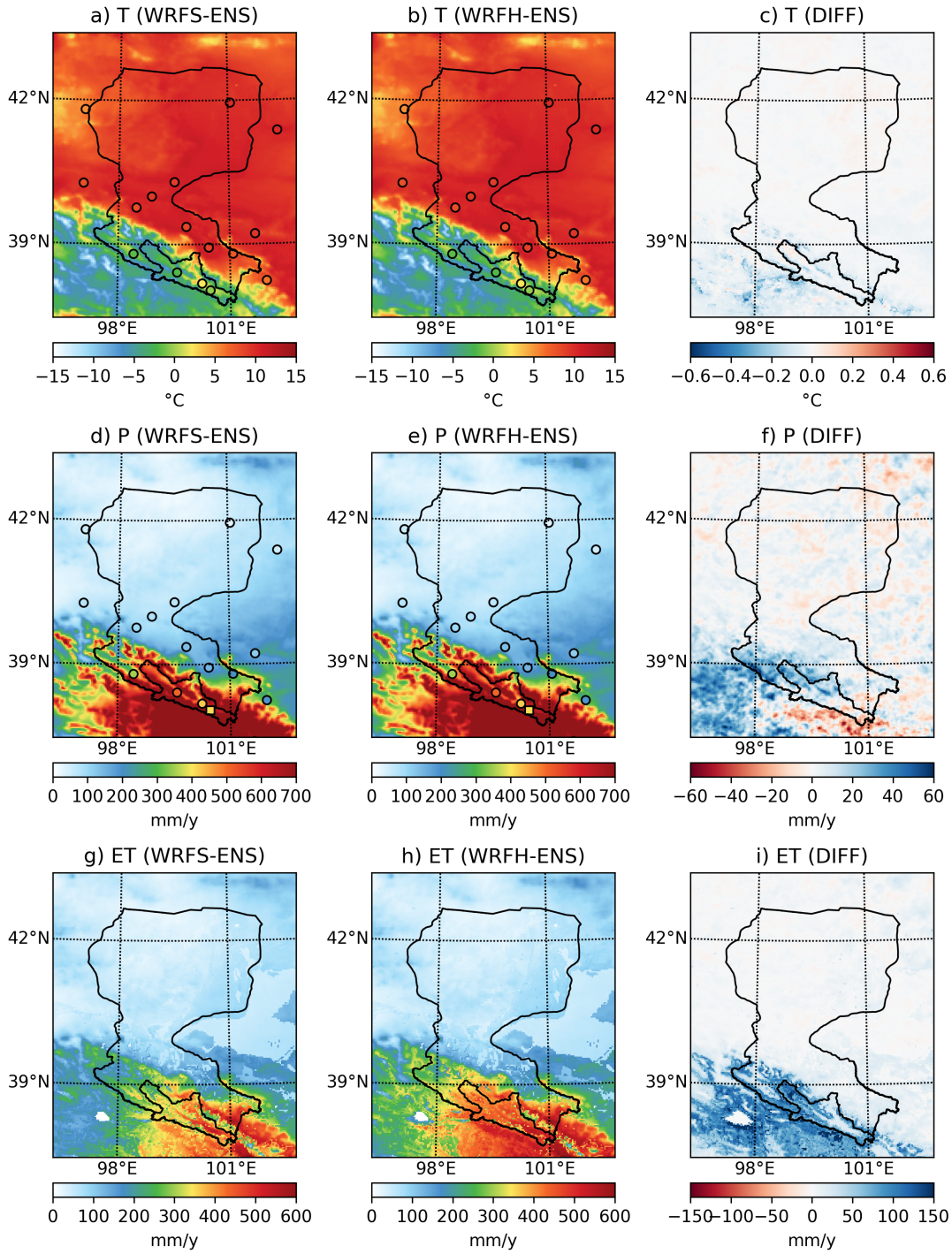

Figure 6.2: Annual mean 2-m air temperature map from a) WRFS-ENS, b) WRFH-ENS, and c) WRFH-ENS minus WRFS-ENS. (d–f) Same as (a–c), but for annual accumulated precipitation. (g–i) Same as (a–c), but for annual accumulated evapotranspiration (ET).

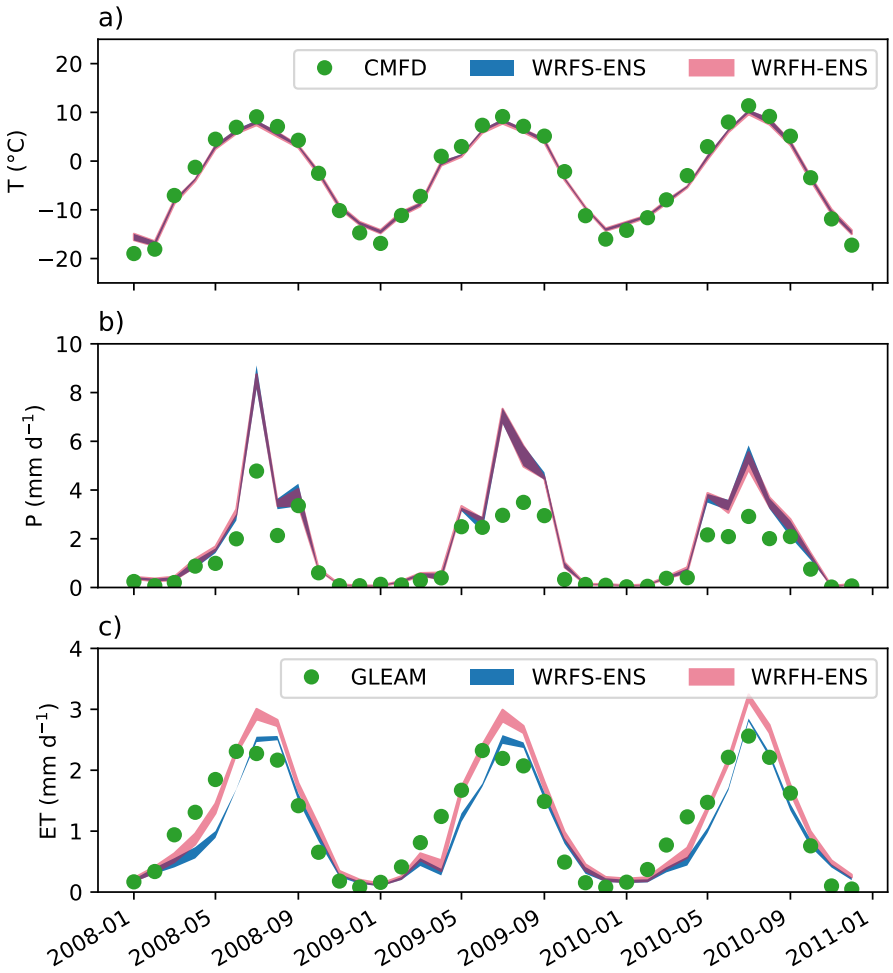

Figure 6.3: Monthly time series of a) 2-m air temperature, b) precipitation, and c) evapotranspiration from reference data set and PBLs ensemble (WRFS-ENS and WRFH-ENS), spatially averaged for the upper HRB.

sensitivity of simulated streamflow is related to the simulated precipitation in wet season, and the sensitivity of the streamflow recession curve and base flow is small. The streamflow peaks show the noticeable sensitivity to PBL schemes, with enhanced uncertainties of simulated precipitation rates during the precipitation events (Arnault et al., 2018; Rummler et al., 2019; Rasmussen et al., 2012).

6.3 Sensitivity of land-atmosphere feedbacks

In the following, the modeled soil-precipitation feedback processes are quantified. The atmospheric moisture tracing method as well as the related tagged precipitation

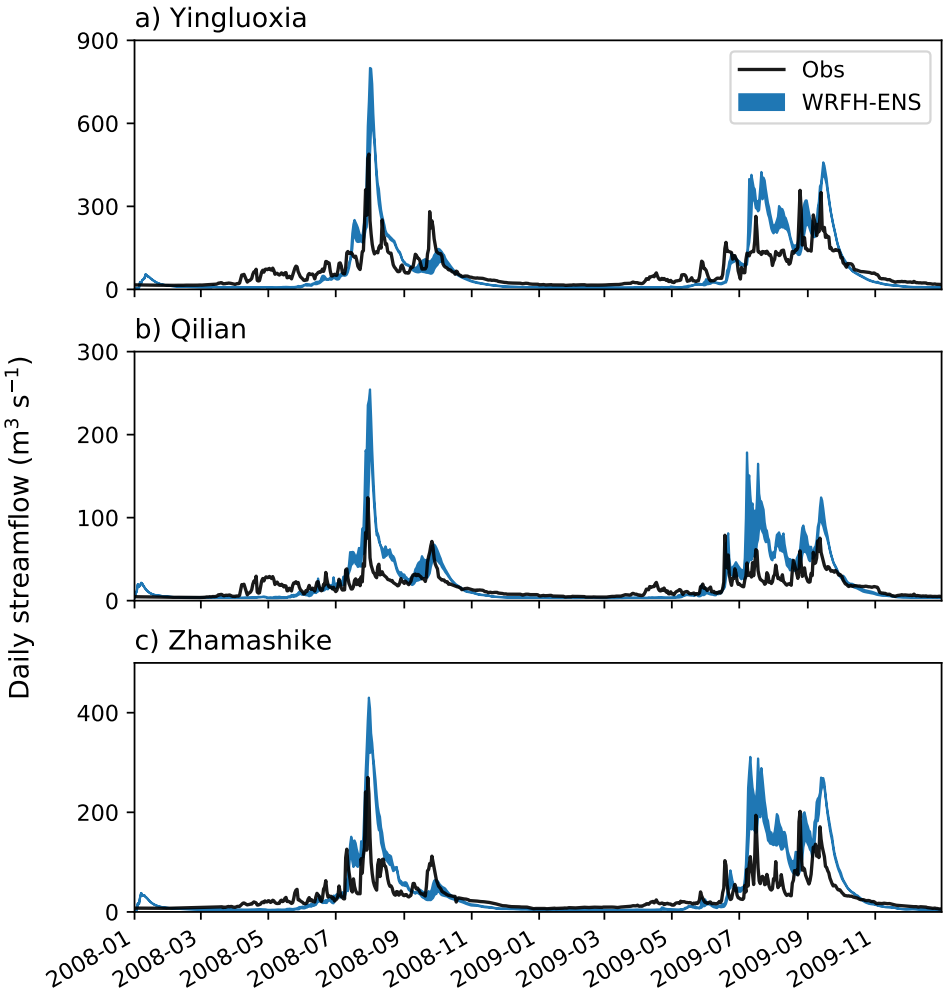

Figure 6.4: Range of daily time series of simulated hydrographs from WRFH-ENS at the gauges a) Yingluoxia, b) Qilian, c) Zhamashike.

recycling is discussed afterwards.

6.3.1 Quantitative analysis of soil-precipitation feedback processes

To quantify the roles of local ET and atmospheric moisture convergence on precipitation, the analysis framework proposed by Schär et al. (1999) and advanced by Asharaf et al. (2012) is used. From the definition of the precipitation efficiency described in Section 2.2, equation

$$P = \chi \cdot (Q_{in} + ET) \tag{6.1}$$

is used in order to express the conditions of control experiment over the analysis area. For the perturbation experiment, Equation 6.1 is written as

$$P' = \chi' \cdot (Q'_{in} + ET'), \tag{6.2}$$

where dashed variables stand for the conditions in the perturbation experiment. Subtracting Equation 6.1 from Equation 6.2, the precipitation difference ΔP can be written as:

$$\Delta P = P' - P = \chi' \cdot (Q'_{in} + ET') - \chi \cdot (Q_{in} + ET). \tag{6.3}$$

Rearranging the right-hand terms following Schär et al. (1999) and Asharaf et al. (2012), ΔP can be separated in to three terms:

$$\Delta P = \underbrace{\Delta\chi \cdot (ET + Q_{in})}_{Efficiency\ effect} + \underbrace{\chi \cdot \Delta ET}_{Surface\ effect} + \underbrace{\chi \cdot \Delta Q_{in}}_{Remote\ effect}. \tag{6.4}$$

On the right-hand of Equation 6.4, the first term depicts the indirect contribution through the impact of precipitation efficiency change, referred as the efficiency effect. The second and the third terms reflect the precipitation change by direct processes though the change of surface ET and incoming atmospheric moisture in the analysis area, which are respectively referred as the surface and remote effects. In this case, the coupled WRF-Hydro ensemble is considered as the perturbation experiment which enrolls the description of lateral terrestrial water flow. In this case, Equation 6.4 allows to distinguish between the direct and indirect effect of lateral terrestrial water flow on precipitation.

As the ensemble members simulate close amounts of precipitation in the dry season (Figure 6.3), this study focuses on the period from May to September of the three consecutive years to quantify the effects of precipitation change induced by lateral terrestrial water flow. Figure 6.5 displays the precipitation difference spatially averaged in the upper HRB between coupled WRF-Hydro and WRF ensembles, as well as the quantified effect terms for each of the 3 PBL schemes. The direct contribution of surface ET is small and positive throughout all the months and PBL schemes, confirming the low precipitation recycling and a positive soil-precipitation feedbacks. All the 3 PBL ensemble show that the remote effect reaches its largest value in July and varies noticeably among the months. This is related to the change of moisture influx,

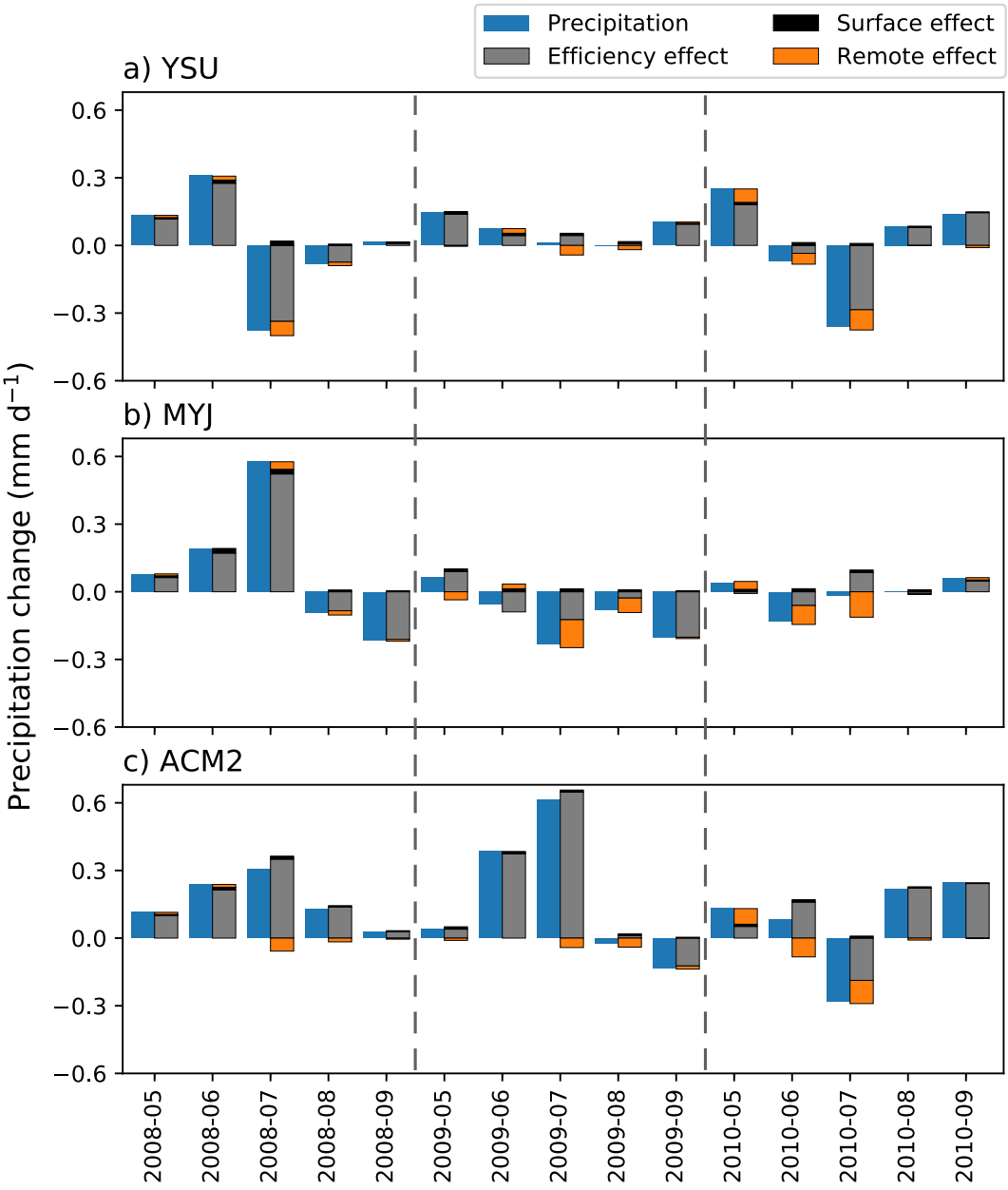

Figure 6.5: Monthly quantified changes of precipitation [WRFH-(PBL) minus WRFS-(PBL)] in wet season (MJJAS) in the upper HRB.

in relation with differences in the simulated atmospheric moisture convergence in the study area. As shown in Figure 6.5, the efficiency effect is the dominant contribution for the precipitation change, and it is mostly positive for the considered months. This efficiency effect can be explained by both the joint contribution of land surface and moisture flux convergence. The increased ET at land surface affects the atmospheric

stability through the thermodynamic processes and associated atmospheric responses (e.g. decreased PBL height, Schär et al., 1999), and the moisture flux convergence can also increase the moist static energy and atmospheric instability, and thereby promote moist convection (Asharaf et al., 2012; Wei et al., 2016). Therefore, the lateral terrestrial water flow has a small direct impact on precipitation, but a much larger indirect impact through the remote and efficiency effects.

6.3.2 Precipitation recycling on land-atmosphere interactions

The atmospheric moisture tracing method (E-tagging) is used for further investigating the sensitivity of land-atmosphere interactions in the ensemble simulations. The precipitation recycling is quantified by the E-tagging approach instead of the former bulk method. As the online moisture tracing method fully deals with three-dimensional atmospheric processes and directly computes the recycled moisture in the model, it is thought to be the closest way to assess the local recycling in regional climate model (Arnault et al., 2016a; Rios-Entenza and Miguez-Macho, 2014). The tagged recycling ratio (β) is introduced in this section:

$$\beta = P_{tag}/P, \tag{6.5}$$

where P_{tag} is the tagged precipitation falling back in the source area. It is noted that the tagged recycling ratio and bulk recycling rate are comparable and their disparity can be quantified (Arnault et al., 2016a), however it is out of the scope of this study.

Figure 6.6 shows the spatial pattern of tagged precipitation amount from the upper HRB and the tagged recycling from three WRF standard ensemble members. The E-tagging results show that a small portion of evaporated moisture falls back at the upper HRB, but the amount differs among three PBL schemes. MYJ PBL scheme has the largest tagged precipitation amount, around 15.5 mm/year evaporated moisture falling back at the source area, whereas the ACM2 has the lowest tagged precipitation amount of 11.9 mm/year. A similar PBL effect is also obtained with WRFH-ENS (not shown).

The sensitivity of monthly tagged recycling rates from 3 PBL schemes is shown in Figure 6.7. The range denotes the recycling values between WRFS- and WRFH-. The monthly recycling rates show highest value with the MYJ PBL scheme. This could be

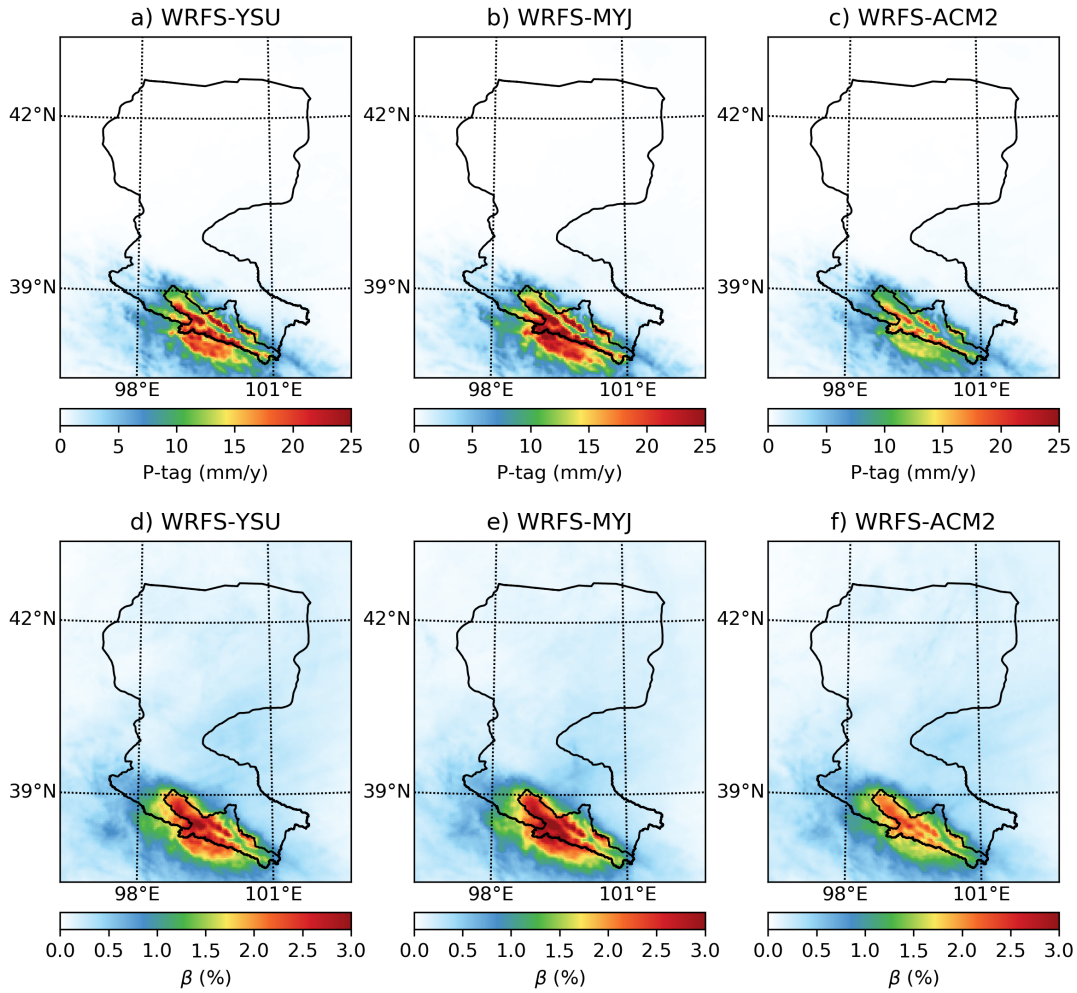

Figure 6.6: Spatial pattern of annual total tagged precipitation amount (a, b, c) and tagged precipitation recycling (d, e, f) from WRF standard experiments (WRFS-) with respect to 3 different PBL schemes.

explained by the local closure scheme difference. The local closure schemes (i.e MYJ) usually produce insufficient mixing in the convective boundary layer (Brown, 1996; Xie et al., 2012; Cohen et al., 2015), and a weaker vertical mixing would transfer less surface water vapor to higher atmosphere layers (Hu et al., 2010). The non-local schemes (i.e. YSU and ACM2) could transport more moisture away from the surface and deposit the moisture at higher atmosphere level (e.g. Hong and Pan, 1996; Srinivas et al., 2007; Hu et al., 2010), which would result in a relatively lower recycling moisture.

The above results show the sensitivity of PBL parameterization in regional climate simulation for describing the land-atmosphere interactions, and perhaps an optimal

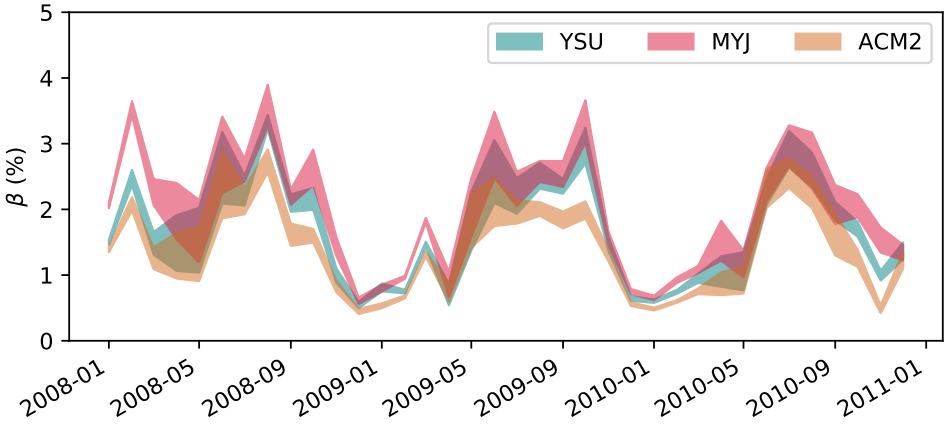

Figure 6.7: Sensitivity of tagged precipitation recycling with respect 3 different PBL schemes.

ensemble of PBL scheme could better represent the atmospheric uncertainty (Arnault et al., 2018). Nevertheless, although Figure 6.6 and 6.7 show the model result is relatively sensitive to the PBL schemes, the tagged recycling values simulated by all the model ensemble members show consistent variations and small values. Thus this ensemble result robustly indicates that the study area is characterized by low local recycling features.

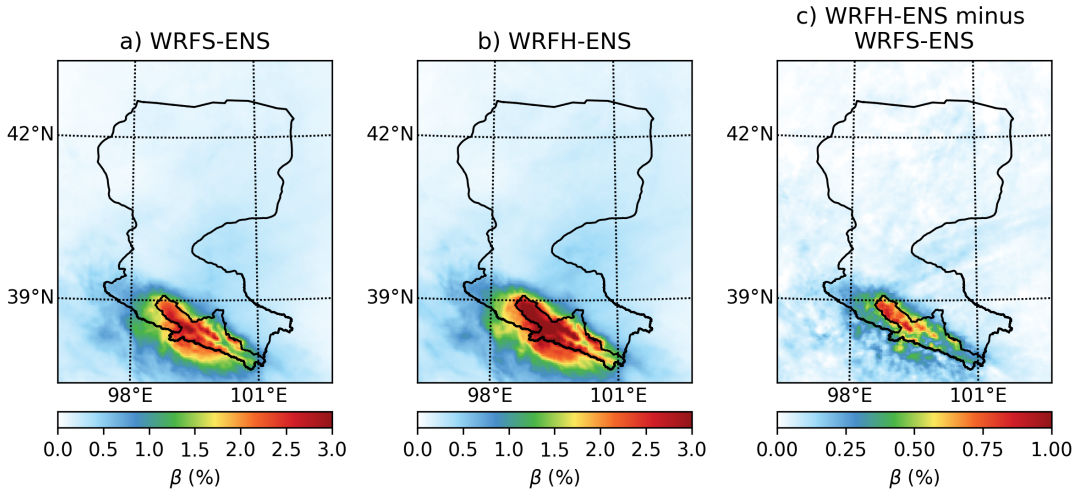

Figure 6.8: Spatial pattern of tagged precipitation recycling from a) WRFS-ENS, b) WRFH-ENS, and the c) difference (WRFH-ENS minus WRFS-ENS).

Differences of tagged recycling rates between WRFH-ENS and WRFS-ENS are shown as spatial maps and monthly time series in Figure 6.8 and 6.9, respectively. Spatial recycling ratio increases in the north western upper HRB, with an average increase

around 0.47% and up to 0.93% in mountain peaks. The monthly recycling rate values are irrespectively increased, up to 1.1% in the summer time. This ensemble result confirms the effect of lateral terrestrial water flow on land-atmosphere interactions discussed in chapter 4. In particular, it confirms the blocking effect of topography in a prevailing East Asian summer monsoon environment, as well as the positive soil-precipitation feedbacks in the study area.

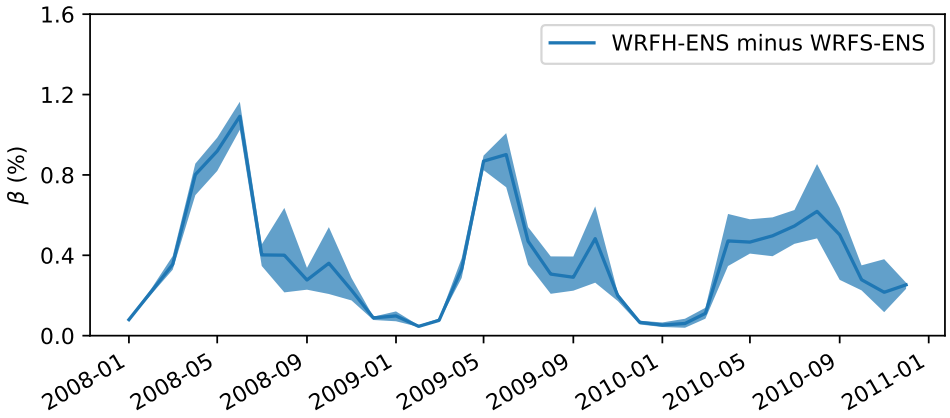

Figure 6.9: Sensitivity of tagged precipitation recycling with respect to the consideration of lateral terrestrial water flow, respective difference from WRFH- minus WRFS-.

6.4 Summary of chapter

This chapter addresses the model uncertainties to the PBL parameterization and representation of lateral terrestrial water flow in the upper HRB. For this purpose, the ensemble of standard WRF and coupled WRF-Hydro simulations is employed for the period 2008–2010, by the consideration of varying turbulence parameterization with three PBL schemes (YSU, MYJ, ACM2).

Similar spatial pattern and seasonal variation of 2-m air temperature, precipitation, and evapotranspiration are simulated by changing the PBL schemes and terrestrial water flow description. Monthly precipitation and evapotranspiration show modest sensitivity to PBL schemes. However, evapotranspiration is distinctly increased by lateral terrestrial water flow regardless of PBL parameterization. The simulated streamflow by coupled WRF-Hydro ensemble shows modest spread during the rainy season and little sensitivity during the recession period and dry season, illustrating

that the streamflow simulation depends on precipitation simulation in the coupled models.

Land-precipitation feedback analysis is used for understanding the precipitation change induced by lateral terrestrial water flow. The coupled WRF-Hydro ensemble simulation is considered as perturbation experiment, and the differences of precipitation are investigated to determine whether they result from the changes in local evapotranspiration (surface effect), external moisture sources (remote effect), or precipitation efficiency effect. This analysis reveals that both the efficiency effect and remote effect are important to the precipitation amounts. The surface effect in precipitation change is small but positive, indicating the positive land-precipitation feedback processes triggered by the lateral terrestrial water flow.

All the model ensemble members use the atmospheric moisture tracing method for quantifying the land-atmosphere interactions. Results show that the quantified recycled evapotranspiration and tagged recycling are modestly sensitive to the PBL parameterization, and the low recycling feature in the study area is confirmed by all model ensemble. Nevertheless, the lateral terrestrial water flow increases the precipitation recycling irrespective of the uncertainty in PBL parameterizations, which indicates the robustness of the finding that there is positive feedback loop through the land surface to the atmosphere in the case of the HRB.

7 Conclusions and outlook

7.1 Summary and conclusions

Lateral terrestrial water processes redistribute the spatial-temporal variability of moisture fluxes in land surface and exert an influence on atmospheric processes through land-atmosphere interactions. With this consideration, the dissertation uses the regional climate model coupled with hydrological lateral parameterization to investigate the joint atmospheric-terrestrial water balance and land-atmosphere interaction for the Heihe River basin, an inland basin characterized by complex terrain and arid to semiarid climate conditions. The fully coupled regional climate-hydrological model, that is the WRF-Hydro model, has been setup within the convection permitting scale at the 3-km resolution for three consecutive years for the period 2008-2010. In order to assess the impact of lateral terrestrial water flow on the simulated water cycle and land-atmosphere interactions, coupled modeling results were compared with the simulation results from standard WRF model. Additionally, this impact was further investigated by ensemble simulations considering its internal variability by varying turbulence parameterization options.

This study presented the remarkable contribution of lateral terrestrial water flow in regional climate modeling on the regional water balance and land-atmosphere interactions. For the study area of HRB, the terrestrial water flow-induced change of land surface conditions in mountainous area resulted in a slight wetting and cooling of the near-surface atmosphere, and further affected the atmospheric moisture convergence through land-atmosphere interactions. The overall impact on precipitation was minor, slightly shifting the precipitation spatial patterns.

Through the precipitation recycling and efficiency measures, the model ensemble

showed that the PBL parameterization modestly affected land-atmosphere interaction, confirming the positive land-precipitation feedback triggered by lateral terrestrial water flow. Nevertheless, it was found that the contribution of local evapotranspiration to precipitation in the study area was relatively low, as most of the precipitation was dominated by moisture advection outside of the analysis area.

The coupled WRF-Hydro showed abilities in the simulation of the observed daily streamflow in the study area. As coupled streamflow simulations do not rely on the direct observational forcing, the coupled WRF-Hydro could be considered as a promising tool in streamflow prediction. Still, reproducing the daily streamflow with the fully coupled model remains a challenge, because the precipitation bias from atmospheric modeling is directly transferred into the hydrological modeling.

7.2 Outlook

Although this study has demonstrated the feasible climate- and hydrological applications that can be prospered from the current coupled atmospheric-hydrological modeling approach, diverse perspectives should be further considered for future development within the coupled modeling framework.

For the aim of understanding the complexity of land-atmosphere interactions, the coupled atmospheric-hydrological modeling WRF-Hydro should be extensively applied in different regions, under diverse orography, climatic and hydrological condition, and further address the effect of lateral terrestrial water flow on atmospheric modeling. The effect needs to be exposed not only in short-term meteorological prediction, but also for the long-term land use change impact studies. In addition, for robust quantification of land-atmosphere feedback mechanisms, it will be necessary to use the larger model ensemble, considering various model internal uncertainties such as physics parameterization, land-surface parameters, initial and lateral boundary conditions. These could allow to systematically check whether the coupled modeling could improve the accuracy of the regional climate modeling performance and land-atmosphere interactions. In addition, since this coupled modeling approach enhances the representation of the terrestrial hydrology, WRF-Hydro model should be further conducted for multi-decade climate projections.

Detailed representation of terrestrial hydrological processes should be enrolled in the further development of the coupled modeling framework. Implementing the underground water feedback and channel water infiltration would allow us to further investigate the regional water balance in the arid area such as the lower HRB. The compartment of glacier water recharge and snow melting processes also need to be considered and improved, when the coupled modeling is implemented for water balance studies in high-alpine catchment (e.g. Alps, Tibet area). Besides, enrolling the anthropogenic water use intervention would extend the relevance of coupled modeling for water resources management.

The performance of streamflow simulation could be further improved by extensively calibrating the hydrological parameters. Direct parameter calibration in the coupled modeling run is only suitable for short-time applications. For long-term seasonal application, investigating the transferability of model parameters from offline to coupled modeling runs, as well as taking into account the inconsistency of model time-step, should be further ways for improving the streamflow simulation in the fully coupled modeling mode.

A Statistical measures

This appendix illustrates the following statistical measures used in this study for the simulated variables evaluation.

Percent bias

The Percent bias (PBIAS) gives the average tendency of the simulation to be larger or smaller than the observation. It is calculated as:

$$PBIAS = \frac{\sum_{t=1}^{n}(S_t - O_t)}{\sum_{t=1}^{n} O_t} \times 100\% \tag{A.1}$$

where S_t is the simulated values for being evaluated, O_t is the observed values, and n is the number of observed and simulated values. The calculated positive value indicates biases of overestimation, while negative value indicates underestimation.

RMSE

The RMSE (root mean square error) is a frequently used measure of the differences between simulated values and observed values. It is non-negative and calculated as:

$$RMSE = \sqrt{\frac{\sum_{t=1}^{n}(S_t - O_t)^2}{n}} \tag{A.2}$$

The RMSE value of 0 indicates a perfect fit to the observed data. Generally, a lower RMSE value is better than a higher one.

Nash-Sutcliffe efficiency

The Nash-Sutcliffe efficiency (NSE; Nash and Sutcliffe, 1970) coefficient is a commonly used criterion to quantitatively describe the accuracy of simulation values, especially for the streamflow. It is calculated as one minus the mean squared error of the simulation normalized by the variance of the observation:

$$NSE = 1 - \frac{\sum_{t=1}^{n}(Q_{sim}^{t} - Q_{obs}^{t})^2}{\sum_{t=1}^{n}(Q_{obs}^{t} - \overline{Q_{obs}})^2} \tag{A.3}$$

where Q_{sim}^{t} is the simulated value, Q_{obs}^{t} is the observed value, and $\overline{Q_{obs}}$ is the averaged observed value. The NSE coefficient ranges from - ∞ to 1, referring that the simulation results are from unacceptable to perfect skill. A coefficient between 0 and 1 generally indicates that the model has an acceptable performance in predictions. However, the NSE coefficient exhibits a strong sensitivity to the extreme peak values, which might yield sub-optimal results when the data set contains large outliers, therefore it provides little information on systematic model biases.

Kling-Gupta efficiency

The Kling-Gupta efficiency (KGE; Gupta et al., 2009) coefficient is another criterion for streamflow simulation evaluation. It overcomes the aforementioned disadvantages of NSE and considers different error types including the error in the mean, the variability and the dynamics (Pool et al., 2018). The KGE efficiency is calculated as:

$$KGE = 1 - \sqrt{(r-1)^2 + (\alpha - 1)^2 + (\beta - 1)^2} \tag{A.4}$$

where r is the Pearson correlation coefficient between simulated and observed values, α is the measure of relative variability in simulated and observed values ($\sigma_{sim}/\sigma_{obs}$), and β is the ratio between the averaged simulated and observed values ($\overline{Q_{sim}}/\overline{Q_{obs}}$). The KGE coefficient ranges from - ∞ to 1, referring the unacceptable model performance to the optimum matching between simulation and observation.

B Online computation of atmospheric water budget

The atmospheric water budget components are computed during the model run by summing up the entire water tendencies at each modeling time-step and in the vertical. In comparison to the atmospheric water budget calculated from hourly or sub-daily model outputs (e.g. Schär et al., 1999; Fitzmaurice, 2007; Kerandi et al., 2018), the calculation at model time-step captures all the simulated atmospheric fluctuations, so that it allows to fully satisfy the atmosphere budget constraint for each grid point and for any arbitrary shape of analysis area. This atmospheric budget online analysis has been reliably verified in Arnault (2013) and Arnault et al. (2016a), and is subsequently implemented in this WRF and coupled WRF-Hydro experiments.

Considering q_v $[kg \cdot kg^{-1}]$ as the mixing ratio of water vapor, q_H $[kg \cdot kg^{-1}]$ as the sum of the mixing ratio of hydrometeors, which includes cloud droplets (q_c), cloud ice (q_i), rain droplets (q_r), snowflakes (q_s) and graupel (q_g) (Hong and Lim, 2006), the atmospheric water vapor and hydrometeors fluxes resolved in the WRF model can be written as following equations:

$$\begin{aligned}\underbrace{(dz \cdot \rho_v)_t}_{a1} = \underbrace{dz \cdot \rho_d \cdot \mu^{-1} \cdot [-(U \cdot q_v)_x - (V \cdot q_v)_y]}_{a2} + \underbrace{dz \cdot \rho_d \cdot F^H_{q_v}}_{a3} \\ + \underbrace{dz \cdot \rho_d \cdot \mu^{-1} \cdot [-(\Omega \cdot q_v)_\eta]}_{a4} + \underbrace{dz \cdot \rho_d \cdot F^V_{q_v}}_{a5} + \underbrace{dz \cdot \rho_d \cdot C}_{a6}\end{aligned} \tag{B.1}$$

$$\begin{aligned}\underbrace{(dz \cdot \rho_H)_t}_{b1} = \underbrace{dz \cdot \rho_d \cdot \mu^{-1} \cdot [-(U \cdot q_H)_x - (V \cdot q_H)_y]}_{b2} + \underbrace{dz \cdot \rho_d \cdot F^H_{q_H}}_{b3} \\ + \underbrace{dz \cdot \rho_d \cdot \mu^{-1} \cdot [-(\Omega \cdot q_H)_\eta]}_{b4} + \underbrace{dz \cdot \rho_d \cdot F^V_{q_H}}_{b5} \underbrace{-dz \cdot \rho_d \cdot C}_{b6} \\ + \underbrace{dz \cdot \rho_d \cdot P_H}_{b7}\end{aligned} \tag{B.2}$$

Where dz $[m]$ is the height of each model level, and μ is the mass of the dry air per unit area within the atmospheric column of each model level; ρ_d $[kg \cdot m^{-3}]$ is the density of dry air, so that $\rho_v = \rho_d \cdot q_v$ and $\rho_H = \rho_d \cdot q_H$ are the density of water vapor and hydrometeors, respectively; subscripts x, y, η, t stand for the derivate operators of WRF coordinate system and the time operator; U, V, Ω are the contravariant vectors of the momentum in the coordinate system; $F^H_{q_v,q_H}$ and $F^V_{q_v,q_H}$ are the horizontal and vertical sub-grid scale transport; C stands for the phase changes in microphysics, and P_h indicates the fallout of hydrometeors. The Equations B.1 and B.2 demonstrate that the water vapor and hydrometeors tendencies $(a1, b1)$ are represented as the sum of the grid-resolved horizontal transport $(a2, b2)$, the subgrid-resolved horizontal transport $(a3, b3)$, grid-resolved vertical transport $(a4, b4)$, subgrid-resolved vertical transport $(a5, b5)$, phase changes $(a6, b6)$, and hydrometeors fallout $(b7)$. In addition, the grid-resolved horizontal transport terms $(a2, b2)$ are respectively decomposed into meridional and zonal water flux tendencies $(Q_u)_t$, $(Q_v)_t$ at grid cell faces based on U, V vectors.

Succeeding above atmospheric water transport resolved in each time-step, the atmospheric water tendencies $(a1, b1)$, and meridional and zonal water flux tendencies $(Q_u)_t$, $(Q_v)_t$ are vertically integrated and accumulated during the model run.

As for calculating the atmospheric water budget terms in Equation 2.2 and 2.3 for an given arbitrary area, the atmospheric moisture convergence $-\nabla \cdot \vec{Q}$ is calculated by summing up the accumulated atmospheric water tendencies $(a1, b1)$ for all the grid cells within the given area. The lateral inflow and outflow moisture is calculated by summing up the meridional and zonal water fluxes at lateral boundaries. The atmospheric water storage amount is simply computed by integrating the total atmospheric water vapor and hydrometeors from the surface to the model top (z_{top}):

$$W = \int_0^{z_{top}} \rho_d \cdot q_v \cdot dz + \int_0^{z_{top}} \rho_d \cdot q_H \cdot dz \tag{B.3}$$

C Algorithm of E-tagging

This appendix briefly introduce the online evaporated water tracing method, namely E-tagging, which is utilized for quantification of the land-atmosphere feedback in the thesis. This method investigates what happens to the evaporated water vapor after land surface evapotranspiration, until it falls as precipitation enrolling again in the regional water cycle. At the regional meteorological scale, the E-tagging method has been implemented in several RCMs, such as the climate high-resolution model (CHRM) by Sodemann et al. (2009), the MM5 model by Knoche and Kunstmann (2013) and Wei et al. (2015), and the WRF model by Arnault et al. (2016a) and Insua-Costa and Miguez-Macho (2018). As this evaporated water tracing is pure resolved in atmospheric physics, E-tagging is directly implemented in the coupled WRF-Hydro modeling in this study.

The E-tagging method is based on the assumption that the tagged moisture is fully mixed with the total atmospheric moisture in each atmosphere model layer. The basis of the E-tagging method is to duplicate the numerical formulations of all the atmospheric moisture processes for tagged moisture. As described in Insua-Costa and Miguez-Macho (2018), the moisture processes in the atmosphere is prognostic as:

$$\frac{\partial q_n}{\partial t} = \underbrace{-\mathbf{v}\cdot\nabla q_n}_{advection} + \underbrace{\nu_q\cdot\nabla^2 q_n}_{molecular\ \ diffusion} + \left(\frac{\partial q_n}{\partial t}\right)_{PBL} + \left(\frac{\partial q_n}{\partial t}\right)_{microphysics} + \left(\frac{\partial q_n}{\partial t}\right)_{convection} \tag{C.1}$$

where q_n denotes the mixing ratio of various moisture species described in Appendix B ($q_v, q_c, q_i, q_r, q_s, q_g$). ∇ is the vector operator, $\mathbf{v}$ $[m\cdot s^{-1}]$ is the covariant velocities in the horizontal and vertical directions, and ν $[m^2\cdot s^{-1}]$ is the kinematic viscosity. The right-hand of the equation illustrates the moisture tendencies due to moisture advection, molecular diffusion, parameterized turbulent transport (PBL), phase transitions (microphysics), and convection, respectively. In this study case, since the model grid

is resolved in the convection permitting scale, the E-tagging method is not conducted for the convection parameterization.

For implementing the E-tagging method in atmosphere model, a mask over the whole model domain is used for defining a moisture source area:

$$MASK = \begin{cases} 1 & \text{source area for moisture tagging} \\ 0 & \text{no tagging} \end{cases} \tag{C.2}$$

and the evapotranspiration entering into the atmosphere from the source area is set to the tagged evapotranspiration (ET_{tag}):

$$ET_{tag} = ET \cdot MASK \tag{C.3}$$

It is noted that the components of evapotranspiration in the WRF-Hydro model differ from those in the WRF model, as the ponded water evaporation is additionally included into the total evapotranspiration in the WRF-Hydro model(described in Section 2.2.2)

$$ET = \underbrace{E_{soil} + E_{transpiration} + E_{interception} + E_{snow}}_{from\ Noah-LSM} + \underbrace{E_{ponded\ water}}_{from\ WRF-Hydro} \tag{C.4}$$

For tracing the tagged water vapor through the atmosphere, new tagged moisture variables $q_{n,tag}$ $[kg \cdot kg^{-1}]$ including $q_{v,tag}$, $q_{c,tag}$, $q_{i,tag}$, $q_{r,tag}$, $q_{s,tag}$, $q_{g,tag}$, are defined corresponding to previous moisture species described in Appendix B. The first three terms on the right side of Equation C.1 which describes grid and sub-grid scale moisture transport, are analogously replicated in the model code as replacing q_n by $q_{n,tag}$, making sure the identical advection and turbulence diffusion are applied for tagged moisture species.

For phase transition of the tagged moisture, the tagged moisture species transformed from phase α to phase β, is proportionally calculated as:

$$C_{\alpha\to\beta,tag} = C_{\alpha\to\beta} \cdot \frac{q_{\alpha,tag}}{q_\alpha} \tag{C.5}$$

where $C_{\alpha\to\beta}$ refers to the rate of total moisture specie transformed from phase α to phase β, and $q_{\alpha,tag}/q_\alpha$ is the fraction of tagged moisture mass at phase α. All the moisture phase transition processes explicated in Figure 1 of Hong and Lim (2006) are elaborated in the similar manner. It is noted the ratio $q_{\alpha,tag}/q_\alpha$ should be carefully handled as following criteria to avoid susceptible numerical flaws in the advection scheme arisen by high tagged moisture gradients (Arnault et al., 2016a).

$$0 \leq \frac{q_{\alpha,tag}}{q_\alpha} \leq 1 \tag{C.6}$$

For the sedimentation processes of the tagged moisture, the tagged precipitating particles have the same advection strategy and sink velocity as the total precipitating particles. The precipitating particles reaching the land surface are written as the tagged precipitation (P_{tag}).

The tagged moisture species which leave the model domain at lateral boundaries are set to zero, which means the returning of the tagged water species from outside of the model lateral boundary is not taken into account. More details of implementing E-tagging into the WRF model are given in Knoche and Kunstmann (2013) and Insua-Costa and Miguez-Macho (2018).

Bibliography

Aas, K. S., Berntsen, T. K., Boike, J., Etzelmüller, B., Kristjánsson, J. E., Maturilli, M., Schuler, T. V., Stordal, F., and Westermann, S. (2015). A comparison between simulated and observed surface energy balance at the Svalbard Archipelago. *Journal of Applied Meteorology and Climatology*, 54(5):1102–1119.doi: 10.1175/JAMC-D-14-0080.1.

An, R., Zhang, L., Wang, Z., Quaye-Ballard, J. A., You, J., Shen, X., Gao, W., Huang, L. J., Zhao, Y., and Ke, Z. (2016). Validation of the ESA CCI soil moisture product in China. *International Journal of Applied Earth Observation and Geoinformation*, 48:28–36.doi: 10.1016/j.jag.2015.09.009.

Arnault, J. (2013). Large-scale dynamical influence of a gravity wave generated over the antarctic peninsula - regional modelling and budget analysis. *Tellus, Series A: Dynamic Meteorology and Oceanography*, 65(1).doi: 10.3402/tellusa.v65i0.20254.

Arnault, J., Knoche, R., Wei, J., and Kunstmann, H. (2016a). Evaporation tagging and atmospheric water budget analysis with WRF: A regional precipitation recycling study for West Africa. *Water Resources Research*, 52(3):1544–1567.doi: 10.1002/2015WR017704.

Arnault, J., Rummler, T., Baur, F., Lerch, S., Wagner, S., Fersch, B., Zhang, Z., Kerandi, N., Keil, C., and Kunstmann, H. (2018). Precipitation sensitivity to the uncertainty of terrestrial water flow in WRF-Hydro: An ensemble analysis for central Europe. *Journal of Hydrometeorology*, 19(6):1007–1025.doi: 10.1175/JHM-D-17-0042.1.

Arnault, J., Wagner, S., Rummler, T., Fersch, B., Bliefernicht, J., Andresen, S., and Kunstmann, H. (2016b). Role of runoff-infiltration partitioning and resolved overland flow on land-atmosphere feedbacks: A case study with the WRF-Hydro coupled modeling system for West Africa. *Journal of Hydrometeorology*, 17(5):1489–1516.doi: 10.1175/JHM-D-15-0089.1.

Arnault, J., Wei, J., Rummler, T., Fersch, B., Zhang, Z., Jung, G., Wagner, S., and Kunstmann, H. (2019). A Joint Soil-Vegetation-Atmospheric Water Tagging Procedure With WRF-Hydro: Implementation and Application to the Case of Precipitation Partitioning in the Upper Danube River Basin. *Water Resources Research*, 55(7):6217–6243.doi: 10.1029/2019WR024780.

Asharaf, S., Dobler, A., and Ahrens, B. (2012). Soil Moisture-Precipitation Feedback Processes in the Indian Summer Monsoon Season. *Journal of Hydrometeorology*, 13(5):1461–1474.doi: 10.1175/JHM-D-12-06.1.

Baldauf, M., Seifert, A., Förstner, J., Majewski, D., Raschendorfer, M., and Reinhardt, T. (2011). Operational Convective-Scale Numerical Weather Prediction with the COSMO Model: Description and Sensitivities. *Monthly Weather Review*, 139(12):3887–3905.doi: 10.1175/MWR-D-10-05013.1.

Barlage, M., Tewari, M., Chen, F., Miguez-Macho, G., Yang, Z. L., and Niu, G. Y. (2015). The effect of groundwater interaction in North American regional climate simulations with WRF/Noah-MP. *Climatic Change*, 129(3-4):485–498.doi: 10.1007/s10584-014-1308-8.

Boyle, D. P., Gupta, H. V., and Sorooshian, S. (2000). Toward improved calibration of hydrologic models: Combining the strengths of manual and automatic methods. *Water Resources Research*, 36(12):3663–3674.doi: 10.1029/2000WR900207.

Braun, S. A. and Tao, W.-K. (2000). Sensitivity of High-Resolution Simulations of Hurricane Bob (1991) to Planetary Boundary Layer Parameterizations. *Monthly Weather Review*, 128(12):3941–3961.doi: 10.1175/1520-0493(2000)129<3941:SOHRSO>2.0.CO;2.

Brown, A. R. (1996). Evaluation of parametrization schemes for the convective boundary layer using large-eddy simulation results. *Boundary-Layer Meteorology*, 81(2):167–200.doi: 10.1007/BF00119064.

Buermann, W., Dong, J., Zeng, X., Myneni, R. B., and Dickinson, R. E. (2001). Evaluation of the Utility of Satellite-Based Vegetation Leaf Area Index Data for Climate Simulations. *Journal of Climate*, 14(17):3536–3550.doi: 10.1175/1520-0442(2001)014<3536:EOTUOS>2.0.CO;2.

Burde, G. I. and Zangvil, A. (2001). The Estimation of Regional Precipitation Recycling. Part I: Review of Recycling Models. *Journal of Climate*, 14(12):2497–2508.doi: 10.1175/1520-0442(2001)014<2497:TEORPR>2.0.CO;2.

Butts, M., Drews, M., Larsen, M. A. D., Lerer, S., Rasmussen, S. H., Grooss, J., Overgaard, J., Refsgaard, J. C., Christensen, O. B., and Christensen, J. H. (2014). Embedding complex hydrology in the regional climate system-Dynamic coupling across different modelling domains. *Advances in Water Resources*, 74:166–184.doi: 10.1016/j.advwatres.2014.09.004.

Cao, Q., Yu, D., Georgescu, M., Han, Z., and Wu, J. (2015). Impacts of land use and land cover change on regional climate: a case study in the agro-pastoral transitional zone of China. *Environmental Research Letters*, 10(12):124025.doi: 10.1088/1748-9326/10/12/124025.

Chen, F. and Dudhia, J. (2001). Coupling an advanced land surface-hydrology model with the Penn State-NCAR MM5 modeling system. Part I: Model implementation and sensitivity. *Monthly Weather Review*, 129(4):569–585.doi: 10.1175/1520-0493(2001)129<0569:CAALSH>2.0.CO;2.

Chen, F., Mitchell, K., Schaake, J., Xue, Y., Pan, H.-L., Koren, V., Duan, Q. Y., Ek, M., and Betts, A. (1996). Modeling of land surface evaporation by four schemes and comparison with FIFE observations. *Journal of Geophysical Research*, 101(D3):7251–7268.doi: 10.1029/95JD02165.

Chen, F. and Xie, Z. (2010). Effects of interbasin water transfer on regional climate: A case study of the Middle Route of the South-to-North Water Transfer Project in China. *Journal of Geophysical Research*, 115(D11):D11112.doi: 10.1029/2009JD012611.

Chen, R., Han, C., Liu, J., Yang, Y., Liu, Z., Wang, L., and Kang, E. (2018). Maximum precipitation altitude on the northern flank of the Qilian Mountains, northwest China. *Hydrology Research*, 49(5):1696–1710.doi: 10.2166/nh.2018.121.

Cheng, G., Li, X., Zhao, W., Xu, Z., Feng, Q., Xiao, S., and Xiao, H. (2014). Integrated study of the water-ecosystem-economy in the Heihe River Basin. *National Science Review*, 1(3):413–428.doi: 10.1093/nsr/nwu017.

Chow, V. T., Maidment, D. R., and Mays, L. W. (1988). *Applied Hydrology*. Civil Engineering. McGraw-Hill.

Clark, M. P., Fan, Y., Lawrence, D. M., Adam, J. C., Bolster, D., Gochis, D. J., Hooper, R. P., Kumar, M., Leung, L. R., Mackay, D. S., Maxwell, R. M., Shen, C., Swenson, S. C., and Zeng, X. (2015). Improving the representation of hydrologic processes in Earth System Models. *Water Resources Research*, 51(8):5929–5956.doi: 10.1002/2015WR017096.

Cohen, A. E., Cavallo, S. M., Coniglio, M. C., and Brooks, H. E. (2015). A Review of Planetary Boundary Layer Parameterization Schemes and Their Sensitivity in Simulating Southeastern U.S. Cold Season Severe Weather Environments. *Weather and Forecasting*, 30(3):591–612.doi: 10.1175/WAF-D-14-00105.1.

Crétat, J., Pohl, B., Richard, Y., and Drobinski, P. (2012). Uncertainties in simulating regional climate of Southern Africa: sensitivity to physical parameterizations using WRF. *Climate Dynamics*, 38(3-4):613–634.doi: 10.1007/s00382-011-1055-8.

Deng, X., Shi, Q., Zhang, Q., Shi, C., and Yin, F. (2015). Impacts of land use and land cover changes on surface energy and water balance in the Heihe River Basin of China, 2000-2010. *Physics and Chemistry of the Earth*, 79-82:2–10.doi: 10.1016/j.pce.2015.01.002.

Dorigo, W. A., Gruber, A., De Jeu, R. A. M., Wagner, W., Stacke, T., Loew, A., Albergel, C., Brocca, L., Chung, D., Parinussa, R. M., and Kidd, R. (2015). Evaluation of the ESA CCI soil moisture product using ground-based observations. *Remote Sensing of Environment*, 162:380–395.doi: 10.1016/j.rse.2014.07.023.

Dourte, D., Shukla, S., Singh, P., and Haman, D. (2013). Rainfall Intensity-Duration-Frequency Relationships for Andhra Pradesh, India: Changing Rainfall Patterns and Implications for Runoff and Groundwater Recharge. *Journal of Hydrologic Engineering*, 18(3):324–330.doi: 10.1061/(ASCE)HE.1943-5584.0000625.

Dudhia, J. (1989). Numerical Study of Convection Observed during the Winter Monsoon Experiment Using a Mesoscale Two-Dimensional Model. *Journal of the Atmospheric Sciences*, 46(20):3077–3107.doi: 10.1175/1520-0469(1989)046<3077:NSOCOD>2.0.CO;2.

Dudhia, J. (2014). Overview of WRF physics. *University Corporation for Atmospheric Research, Boulder, CO*.

Ek, M. B., Mitchell, K. E., Lin, Y., Rogers, E., Grunmann, P., Koren, V., Gayno, G., and Tarpley, J. D. (2003). Implementation of Noah land surface

model advances in the National Centers for Environmental Prediction operational mesoscale Eta model. *Journal of Geophysical Research*, 108(D22):8851.doi: 10.1029/2002JD003296.

Eltahir, E. A. B. and Bras, R. L. (1996). Precipitation recycling. *Reviews of Geophysics*, 34(3):367–378.doi: 10.1029/96RG01927.

Erlandsen, H. B., Haddeland, I., Tallaksen, L. M., and Kristiansen, J. (2017). The Sensitivity of the Terrestrial Surface Energy and Water Balance Estimates in the WRF Model to Lower Surface Boundary Representations: A South Norway Case Study. *Journal of Hydrometeorology*, 18(1):265–284.doi: 10.1175/JHM-D-15-0146.1.

Fan, Y., Miguez-Macho, G., Weaver, C. P., Walko, R., and Robock, A. (2007). Incorporating water table dynamics in climate modeling: 1. Water table observations and equilibrium water table simulations. *Journal of Geophysical Research*, 112(D10).doi: 10.1029/2006JD008111.

Fersch, B. and Kunstmann, H. (2014). Atmospheric and terrestrial water budgets: Sensitivity and performance of configurations and global driving data for long term continental scale WRF simulations. *Climate Dynamics*, 42(9-10):2367–2396.doi: 10.1007/s00382-013-1915-5.

Fitzmaurice, J. A. (2007). *A critical Analysis of Bulk Precipitation Recycling Models*. type, Massachusetts Institute of Technology.

Foken, T. (2008). The energy balance closure problem: An overview. *Ecological Applications*, 18(6):1351–1367.doi: 10.1890/06-0922.1.

Gao, B., Qin, Y., Wang, Y., Yang, D., and Zheng, Y. (2016). Modeling ecohydrological processes and spatial patterns in the upper Heihe basin in China. *Forests*, 7(1):1–21.doi: 10.3390/f7010010.

Gao, Y. (2017). Studying precipitation recycling over the Tibetan Plateau using evaporation-tagging and back-trajectory analysis. *AGU Fall Meeting Abstracts*.

Gao, Y., Chen, F., Barlage, M., Liu, W., Cheng, G., Li, X., Yu, Y., Ran, Y., Li, H., Peng, H., and Ma, M. (2008). Enhancement of land surface information and its impact on atmospheric modeling in the Heihe River Basin, northwest China. *Journal of Geophysical Research*, 113(D20):D20S90.doi: 10.1029/2008JD010359.

Gao, Y., Cheng, G., Cui, W., Chen, F., David, G., and Yu, W. (2006). Coupling of enhanced land surface hydrology with atmospheric mesoscale model and its application in Heihe River Basin. *Advances in Earth Science, (in Chinese)*, 21(12):1283–1292.

Gao, Y., Lu, S., and Cheng, G. (2004). Simulation of rainfall-runoff and watershed convergence process in the upper reaches of Heihe River Basin, July 2002. *Science in China Series D*, 47(Supp.1):1–8.doi: 10.1360/04zd0001.

García-Díez, M., Fernández, J., Fita, L., and Yagüe, C. (2013). Seasonal dependence of WRF model biases and sensitivity to PBL schemes over Europe. *Quarterly Journal of the Royal Meteorological Society*, 139(671):501–514.doi: 10.1002/qj.1976.

Givati, A., Gochis, D., Rummler, T., and Kunstmann, H. (2016). Comparing one-way and two-way coupled hydrometeorological forecasting systems for flood forecasting in the Mediterranean region. *Hydrology*, 3(2):19.doi: 10.3390/hydrology3020019.

Gochis, D., Yu, W., and Yates, D. (2015). *The NCAR WRF-Hydro technical description and user's guide, version 3.0.*

Gómez-Navarro, J. J., Raible, C. C., and Dierer, S. (2015). Sensitivity of the WRF model to PBL parametrisations and nesting techniques: evaluation of wind storms over complex terrain. *Geoscientific Model Development*, 8(10):3349–3363.doi: 10.5194/gmd-8-3349-2015.

Graham, L. P., Hagemann, S., Jaun, S., and Beniston, M. (2007). On interpreting hydrological change from regional climate models. *Climatic Change*, 81(SUPPL. 1):97–122.doi: 10.1007/s10584-006-9217-0.

Greve, P., Warrach-Sagi, K., and Wulfmeyer, V. (2013). Evaluating soil water content in a WRF-Noah downscaling experiment. *Journal of Applied Meteorology and Climatology*, 52(10):2312–2327.doi: 10.1175/JAMC-D-12-0239.1.

Gupta, H. V., Kling, H., Yilmaz, K. K., and Martinez, G. F. (2009). Decomposition of the mean squared error and NSE performance criteria: Implications for improving hydrological modelling. *Journal of Hydrology*, 377(1-2):80–91.doi: 10.1016/j.jhydrol.2009.08.003.

Harding, K. J. and Snyder, P. K. (2012). Modeling the Atmospheric Response to Irrigation in the Great Plains. Part I: General Impacts on Precipitation and the

Energy Budget. *Journal of Hydrometeorology*, 13(6):1667–1686.doi: 10.1175/JHM-D-11-098.1.

He, J. and Yang, K. (2011). China Meteorological Forcing Dataset. *Cold and Arid Regions Science Data Center at Lanzhou*.doi: 10.3972/westdc.002.2014.db.

Hong, S. and Lim, J. (2006). The WRF single-moment 6-class microphysics scheme (WSM6). *Journal of the Korean Meteorological Society*, 42(2):129–151.

Hong, S.-Y., Noh, Y., and Dudhia, J. (2006). A New Vertical Diffusion Package with an Explicit Treatment of Entrainment Processes. *Monthly Weather Review*, 134(9):2318–2341.doi: 10.1175/MWR3199.1.

Hong, S.-Y. and Pan, H.-L. (1996). Nonlocal Boundary Layer Vertical Diffusion in a Medium-Range Forecast Model. *Monthly Weather Review*, 124(10):2322–2339.doi: 10.1175/1520-0493(1996)124<2322:NBLVDI>2.0.CO;2.

Hu, X.-M., Nielsen-Gammon, J. W., and Zhang, F. (2010). Evaluation of Three Planetary Boundary Layer Schemes in the WRF Model. *Journal of Applied Meteorology and Climatology*, 49(9):1831–1844.doi: 10.1175/2010JAMC2432.1.

Insua-Costa, D. and Miguez-Macho, G. (2018). A new moisture tagging capability in the Weather Research and Forecasting model: formulation, validation and application to the 2014 Great Lake-effect snowstorm. *Earth System Dynamics*, 9(1):167–185.doi: 10.5194/esd-9-167-2018.

Janjić, Z. I. (1994). The Step-Mountain Eta Coordinate Model: Further Developments of the Convection, Viscous Sublayer, and Turbulence Closure Schemes. *Monthly Weather Review*, 122(5):927–945.doi: 10.1175/1520-0493(1994)122<0927:TSMECM>2.0.CO;2.

Jankov, I., Gallus, W. A., Segal, M., Shaw, B., and Koch, S. E. (2005). The Impact of Different WRF Model Physical Parameterizations and Their Interactions on Warm Season MCS Rainfall. *Weather and Forecasting*, 20(6):1048–1060.doi: 10.1175/WAF888.1.

Ji, P., Yuan, X., and Liang, X. Z. (2017). Do Lateral Flows Matter for the Hyperresolution Land Surface Modeling? *Journal of Geophysical Research: Atmospheres*, 122(22):12,077–12,092.doi: 10.1002/2017JD027366.

Jousse, A., Hall, A., Sun, F., and Teixeira, J. (2016). Causes of WRF surface energy fluxes biases in a stratocumulus region. *Climate Dynamics*, 46(1-2):571–584.doi: 10.1007/s00382-015-2599-9.

Julien, P. Y., Saghafian, B., and Ogden, F. L. (1995). Raster-based hydrological modeling of spatially-varied surface runoff. *Journal of the American Water Resources Association*, 31(3):523–536.doi: 10.1111/j.1752-1688.1995.tb04039.x.

Jung, M., Reichstein, M., Margolis, H. A., Cescatti, A., Richardson, A. D., Arain, M. A., Arneth, A., Bernhofer, C., Bonal, D., Chen, J., Gianelle, D., Gobron, N., Kiely, G., Kutsch, W., Lasslop, G., Law, B. E., Lindroth, A., Merbold, L., Montagnani, L., Moors, E. J., Papale, D., Sottocornola, M., Vaccari, F., and Williams, C. (2011). Global patterns of land-atmosphere fluxes of carbon dioxide, latent heat, and sensible heat derived from eddy covariance, satellite, and meteorological observations. *Journal of Geophysical Research*, 116(3):G00J07.doi: 10.1029/2010JG001566.

Kerandi, N., Arnault, J., Laux, P., Wagner, S., Kitheka, J., and Kunstmann, H. (2018). Joint atmospheric-terrestrial water balances for East Africa: a WRF-Hydro case study for the upper Tana River basin. *Theoretical and Applied Climatology*, 131(3-4):1337–1355.doi: 10.1007/s00704-017-2050-8.

Kerandi, N. M. (2018). *Joint Atmospheric-Terrestrial Water Balance for the Tana River Basin of Kenya, East Africa by Coupled Atmospheric-Hydrological Modeling*. doctoralthesis, Universität Augsburg.

Klein, C., Heinzeller, D., Bliefernicht, J., and Kunstmann, H. (2015). Variability of West African monsoon patterns generated by a WRF multi-physics ensemble. *Climate Dynamics*, 45(9-10):2733–2755.doi: 10.1007/s00382-015-2505-5.

Knoche, H. R. and Kunstmann, H. (2013). Tracking atmospheric water pathways by direct evaporation tagging: A case study for West Africa. *Journal of Geophysical Research: Atmospheres*, 118(22):12,345–12,358.doi: 10.1002/2013JD019976.

Kokkonen, T., Koivusalo, H., Karvonen, T., Croke, B., and Jakeman, A. (2004). Exploring streamflow response to effective rainfall across event magnitude scale. *Hydrological Processes*, 18(8):1467–1486.doi: 10.1002/hyp.1423.

Koren, V., Schaake, J., Mitchell, K., Duan, Q.-Y., Chen, F., and Baker, J. M. (1999). A parameterization of snowpack and frozen ground intended for NCEP weather

and climate models. *Journal of Geophysical Research*, 104(D16):19569–19585.doi: 10.1029/1999JD900232.

Kunstmann, H. and Jung, G. (2007). Influence of soil-moisture and land use change on precipitation in the volta basin of West Africa. *International Journal of River Basin Management*, 5(1):9–16.doi: 10.1080/15715124.2007.9635301.

Laprise, R. (1992). The Euler Equations of Motion with Hydrostatic Pressure as an Independent Variable. *Monthly Weather Review*, 120(1):197–207.doi: 10.1175/1520-0493(1992)120<0197:TEEOMW>2.0.CO;2.

Larsen, M. A. D., Christensen, J. H., Drews, M., Butts, M. B., and Refsgaard, J. C. (2016). Local control on precipitation in a fully coupled climate-hydrology model. *Scientific Reports*, 6(1):22927.doi: 10.1038/srep22927.

Laux, P., Nguyen, P. N. B., Cullmann, J., Van, T. P., and Kunstmann, H. (2017). How many RCM ensemble members provide confidence in the impact of land-use land cover change? *International Journal of Climatology*, 37(4):2080–2100.doi: 10.1002/joc.4836.

Lehner, B., Verdin, K., and Jarvis, A. (2008). New Global Hydrography Derived From Spaceborne Elevation Data. *Eos, Transactions American Geophysical Union*, 89(10):93.doi: 10.1029/2008EO100001.

Li, L., Gochis, D. J., Sobolowski, S., and Mesquita, M. D. S. (2017a). Evaluating the present annual water budget of a Himalayan headwater river basin using a high-resolution atmosphere-hydrology model. *Journal of Geophysical Research: Atmospheres*, 122(9):4786–4807.doi: 10.1002/2016JD026279.

Li, L., Li, J., Chen, H., and Yu, R. (2019). Diurnal Variations of Summer Precipitation over the Qilian Mountains in Northwest China. *Journal of Meteorological Research*, 33(1):18–30.doi: 10.1007/s13351-019-8103-4.

Li, N., Jia, L., Lu, J., Menenti, M., and Zhou, J. (2017b). Regional surface soil heat flux estimate from multiple remote sensing data in a temperate and semiarid basin. *Journal of Applied Remote Sensing*, 11(1):016028.doi: 10.1117/1.JRS.11.016028.

Li, Q. and Yang, G. (2017). Temporal Distribution Characteristics of Alpine Precipitation and Their Vertical Differentiation: A Case Study from the Upper Shule River. *Water*, 9(4):284.doi: 10.3390/w9040284.

Li, X., Cheng, G., Ge, Y., Li, H., Han, F., Hu, X., Tian, W., Tian, Y., Pan, X., Nian, Y., Zhang, Y., Ran, Y., Zheng, Y., Gao, B., Yang, D., Zheng, C., Wang, X., Liu, S., and Cai, X. (2018a). Hydrological Cycle in the Heihe River Basin and Its Implication for Water Resource Management in Endorheic Basins. *Journal of Geophysical Research: Atmospheres*, 123(2):890–914.doi: 10.1002/2017JD027889.

Li, X., Cheng, G., Lin, H., Cai, X., Fang, M., Ge, Y., Hu, X., Chen, M., and Li, W. (2018b). Watershed System Model: The Essentials to Model Complex Human-Nature System at the River Basin Scale. *Journal of Geophysical Research: Atmospheres*, 123(6):3019–3034.doi: 10.1002/2017JD028154.

Li, X., Cheng, G., Liu, S., Xiao, Q., Ma, M., Jin, R., Che, T., Liu, Q., Wang, W., Qi, Y., Wen, J., Li, H., Zhu, G., Guo, J., Ran, Y., Wang, S., Zhu, Z., Zhou, J., Hu, X., and Xu, Z. (2013). Heihe watershed allied telemetry experimental research (HiWater) scientific objectives and experimental design. *Bulletin of the American Meteorological Society*, 94(8):1145–1160.doi: 10.1175/BAMS-D-12-00154.1.

Li, Z., Gao, Y., Wang, Y., Pan, Y., Li, J., Chen, A., Wang, T., Han, C., Song, Y., and W. H., T. (2015). Can monsoon moisture arrive in the Qilian Mountains in summer? *Quaternary International*, 358:113–125.doi: 10.1016/j.quaint.2014.08.046.

Lin, P., Rajib, M. A., Yang, Z. L., Somos-Valenzuela, M., Merwade, V., Maidment, D. R., Wang, Y., and Chen, L. (2018). Spatiotemporal evaluation of simulated evapotranspiration and streamflow over Texas using the WRF-Hydro-RAPID modeling framework. *Journal of the American Water Resources Association*, 54(1):40–54.doi: 10.1111/1752-1688.12585.

Littlewood, I. G. and Croke, B. F. W. (2013). Effects of data time-step on the accuracy of calibrated rainfall–streamflow model parameters: practical aspects of uncertainty reduction. *Hydrology Research*, 44(3):430.doi: 10.2166/nh.2012.099.

Liu, J., Jia, B., Xie, Z., and Shi, C. (2016). Ensemble simulation of land evapotranspiration in China based on a multi-forcing and multi-model approach. *Advances in Atmospheric Sciences*, 33(6):673–684.doi: 10.1007/s00376-016-5213-0.

Liu, S. M., Xu, Z. W., Wang, W. Z., Jia, Z. Z., Zhu, M. J., Bai, J., and Wang, J. M. (2011). A comparison of eddy-covariance and large aperture scintillometer measurements with respect to the energy balance closure problem. *Hydrology and Earth System Sciences*, 15(4):1291–1306.doi: 10.5194/hess-15-1291-2011.

Liu, X., Zhang, M., Wang, S., Wang, J., Zhao, P., and Zhou, P. (2017). Assessment of diurnal variation of summer precipitation over the Qilian Mountains based on an hourly merged dataset from 2008 to 2014. *Journal of Geographical Sciences*, 27(3):326–336.doi: 10.1007/s11442-017-1379-3.

Lu, N., Chen, S., Wilske, B., Sun, G., and Chen, J. (2011). Evapotranspiration and soil water relationships in a range of disturbed and undisturbed ecosystems in the semi-arid Inner Mongolia, China. *Journal of Plant Ecology*, 4(1-2):49–60.doi: 10.1093/jpe/rtq035.

Ma, N., Szilagyi, J., Zhang, Y., and Liu, W. (2019). Complementary-Relationship-Based Modeling of Terrestrial Evapotranspiration Across China During 1982–2012: Validations and Spatiotemporal Analyses. *Journal of Geophysical Research: Atmospheres*, 124(8):4326–4351.doi: 10.1029/2018JD029850.

Mahrt, L. and Ek, M. (1984). The Influence of Atmospheric Stability on Potential Evaporation. *Journal of Climate and Applied Meteorology*, 23(2):222–234.doi: 10.1175/1520-0450(1984)023<0222:TIOASO>2.0.CO;2.

Mahrt, L. and Pan, H. (1984). A two-layer model of soil hydrology. *Boundary-Layer Meteorology*, 29(1):1–20.doi: 10.1007/BF00119116.

Maidment, D. R. (2017). Conceptual framework for the national flood interoperability experiment. *Journal of the American Water Resources Association*, 53(2):245–257.doi: 10.1111/1752-1688.12474.

Martens, B., Miralles, D. G., Lievens, H., Van Der Schalie, R., De Jeu, R. A., Fernández-Prieto, D., Beck, H. E., Dorigo, W. A., and Verhoest, N. E. (2017). GLEAM v3: Satellite-based land evaporation and root-zone soil moisture. *Geoscientific Model Development*, 10(5):1903–1925.doi: 10.5194/gmd-10-1903-2017.

Maxwell, R. M., Chow, F. K., and Kollet, S. J. (2007). The groundwater-land-surface-atmosphere connection: Soil moisture effects on the atmospheric boundary layer in fully-coupled simulations. *Advances in Water Resources*, 30(12):2447–2466.doi: 10.1016/j.advwatres.2007.05.018.

Maxwell, R. M., Lundquist, J. K., Mirocha, J. D., Smith, S. G., Woodward, C. S., and Tompson, A. F. B. (2011). Development of a Coupled Groundwater-Atmosphere Model. *Monthly Weather Review*, 139(1):96–116.doi: 10.1175/2010MWR3392.1.

Meng, X., Lü, S., Zhang, T., Guo, J., Gao, Y., Bao, Y., Wen, L., Luo, S., and Liu, Y. (2009). Numerical simulations of the atmospheric and land conditions over the Jinta oasis in northwestern China with satellite-derived land surface parameters. *Journal of Geophysical Research*, 114(D6):D06114.doi: 10.1029/2008JD010360.

Milly, P. C. D., Dunne, K. A., and Vecchia, A. V. (2005). Global pattern of trends in streamflow and water availability in a changing climate. *Nature*, 438(7066):347–350.doi: 10.1038/nature04312.

Minder, J. R., Letcher, T. W., and Skiles, S. M. (2016). An evaluation of high-resolution regional climate model simulations of snow cover and albedo over the Rocky Mountains, with implications for the simulated snow-albedo feedback. *Journal of Geophysical Research: Atmospheres*, 121(15):9069–9088.doi: 10.1002/2016JD024995.

Mitchell, K. E., Lohmann, D., Houser, P. R., Wood, E. F., Schaake, J. C., Robock, A., Cosgrove, B. A., Sheffield, J., Duan, Q., Luo, L., Higgins, R. W., Pinker, R. T., Tarpley, J. D., Lettenmaier, D. P., Marshall, C. H., Entin, J. K., Pan, M., Shi, W., Koren, V., Meng, J., Ramsay, B. H., and Bailey, A. A. (2004). The multi-institution North American Land Data Assimilation System (NLDAS): Utilizing multiple GCIP products and partners in a continental distributed hydrological modeling system. *Journal of Geophysical Research*, 109(D7):D07S90.doi: 10.1029/2003JD003823.

Mlawer, E. J., Taubman, S. J., Brown, P. D., Iacono, M. J., and Clough, S. A. (1997). Radiative transfer for inhomogeneous atmospheres: RRTM, a validated correlated-k model for the longwave. *Journal of Geophysical Research*, 102(D14):16663–16682.doi: 10.1029/97JD00237.

Nash, J. and Sutcliffe, J. (1970). River flow forecasting through conceptual models part I — A discussion of principles. *Journal of Hydrology*, 10(3):282–290.doi: 10.1016/0022-1694(70)90255-6.

NCAR (2015). Advanced research WRF (ARW) version 3 modeling system user's guide, July 2015. *Mesoscale and Microscale Meteorology Division-National Center for Atmospheric Research (MMM-NCAR)*.

Ogden, F. L. (1997). CASC2D reference manual. *University of Connecticut. Storrs, CT.*.

Oleson, K. W., Niu, G.-Y., Yang, Z.-L., Lawrence, D. M., Thornton, P. E., Lawrence, P. J., Stöckli, R., Dickinson, R. E., Bonan, G. B., Levis, S., Dai, A., and Qian, T. (2008). Improvements to the Community Land Model and their impact on the hydrological cycle. *Journal of Geophysical Research*, 113(G01021).doi: 10.1029/2007JG000563.

Pan, H.-L. and Mahrt, L. (1987). Interaction between soil hydrology and boundary-layer development. *Boundary-Layer Meteorology*, 38(1-2):185–202.doi: 10.1007/BF00121563.

Pan, X., Li, X., Shi, X., Han, X., Luo, L., and Wang, L. (2012). Dynamic downscaling of near-surface air temperature at the basin scale using WRF-a case study in the Heihe River Basin, China. *Frontiers of Earth Science*, 6(3):314–323.doi: 10.1007/s11707-012-0306-2.

Pan, X., Li, X., Yang, K., He, J., Zhang, Y., and Han, X. (2014). Comparison of downscaled precipitation data over a mountainous watershed : A case study in the Heihe River Basin. *Journal of Hydrometeorology*, 15(4):1560–1574.doi: 10.1175/JHM-D-13-0202.1.

Pei, L., Moore, N., Zhong, S., Kendall, A. D., Gao, Z., and Hyndman, D. W. (2016). Effects of irrigation on summer precipitation over the United States. *Journal of Climate*, 29(10):3541–3558.doi: 10.1175/JCLI-D-15-0337.1.

Pleim, J. E. (2007). A combined local and nonlocal closure model for the atmospheric boundary layer. Part I: Model description and testing. *Journal of Applied Meteorology and Climatology*, 46(9):1383–1395.doi: 10.1175/JAM2539.1.

Pool, S., Vis, M., and Seibert, J. (2018). Evaluating model performance: towards a non-parametric variant of the Kling-Gupta efficiency. *Hydrological Sciences Journal*, 63(13-14):1941–1953.doi: 10.1080/02626667.2018.1552002.

Powers, J. G., Klemp, J. B., Skamarock, W. C., Davis, C. A., Dudhia, J., Gill, D. O., Coen, J. L., Gochis, D. J., Ahmadov, R., Peckham, S. E., Grell, G. A., Michalakes, J., Trahan, S., Benjamin, S. G., Alexander, C. R., Dimego, G. J., Wang, W., Schwartz, C. S., Romine, G. S., Liu, Z., Snyder, C., Chen, F., Barlage, M. J., Yu, W., and Duda, M. G. (2017). The weather research and forecasting model: Overview, system efforts, and future directions. *Bulletin of the American Meteorological Society*, 98(8):1717–1737.doi: 10.1175/BAMS-D-15-00308.1.

Prein, A. F., Langhans, W., Fosser, G., Ferrone, A., Ban, N., Goergen, K., Keller, M., Tölle, M., Gutjahr, O., Feser, F., Brisson, E., Kollet, S., Schmidli, J., Van Lipzig, N. P., and Leung, R. (2015). A review on regional convection-permitting climate modeling: Demonstrations, prospects, and challenges. *Reviews of Geophysics*, 53(2):323–361.doi: 10.1002/2014RG000475.

Rasmussen, S. H., Christensen, J. H., Drews, M., Gochis, D. J., and Refsgaard, J. C. (2012). Spatial-Scale Characteristics of Precipitation Simulated by Regional Climate Models and the Implications for Hydrological Modeling. *Journal of Hydrometeorology*.doi: 10.1175/jhm-d-12-07.1.

Reichstein, M., Falge, E., Baldocchi, D., Papale, D., Aubinet, M., Berbigier, P., Bernhofer, C., Buchmann, N., Gilmanov, T., Granier, A., Grunwald, T., Havrankova, K., Ilvesniemi, H., Janous, D., Knohl, A., Laurila, T., Lohila, A., Loustau, D., Matteucci, G., Meyers, T., Miglietta, F., Ourcival, J.-M., Pumpanen, J., Rambal, S., Rotenberg, E., Sanz, M., Tenhunen, J., Seufert, G., Vaccari, F., Vesala, T., Yakir, D., and Valentini, R. (2005). On the separation of net ecosystem exchange into assimilation and ecosystem respiration: review and improved algorithm. *Global Change Biology*, 11(9):1424–1439.doi: 10.1111/j.1365-2486.2005.001002.x.

Rios-Entenza, A. and Miguez-Macho, G. (2014). Moisture recycling and the maximum of precipitation in spring in the Iberian Peninsula. *Climate Dynamics*, 42(11-12):3207–3231.doi: 10.1007/s00382-013-1971-x.

Roberts, J. and Snelgrove, K. (2015). Atmospheric and Terrestrial Water Balances of Labrador's Churchill River Basin, as Simulated by the North American Regional Climate Change Assessment Program. *Atmosphere-Ocean*, 53(3):304–318.doi: 10.1080/07055900.2015.1029870.

Rodell, M., Houser, P. R., Jambor, U., Gottschalck, J., Mitchell, K., Meng, C.-J., Arsenault, K., Cosgrove, B., Radakovich, J., Bosilovich, M., Entin, J. K., Walker, J. P., Lohmann, D., and Toll, D. (2004). The Global Land Data Assimilation System. *Bulletin of the American Meteorological Society*, 85(3):381–394.doi: 10.1175/BAMS-85-3-381.

Ruan, H., Zou, S., Yang, D., Wang, Y., Yin, Z., Lu, Z., Li, F., and Xu, B. (2017). Runoff Simulation by SWAT Model Using High-Resolution Gridded Precipitation in the Upper Heihe River Basin, Northeastern Tibetan Plateau. *Water*, 9(11):866.doi: 10.3390/w9110866.

Rummler, T., Arnault, J., Gochis, D., and Kunstmann, H. (2019). Role of lateral terrestrial water flow on the regional water cycle in a complex terrain region: Investigation with a fully coupled model system. *Journal of Geophysical Research: Atmospheres*, 124(2):507–529.doi: 10.1029/2018JD029004.

Salas, F. R., Somos-Valenzuela, M. A., Dugger, A., Maidment, D. R., Gochis, D. J., David, C. H., Yu, W., Ding, D., Clark, E. P., and Noman, N. (2018). Towards real-time continental scale streamflow simulation in continuous and discrete space. *Journal of the American Water Resources Association*, 54(1):7–27.doi: 10.1111/1752-1688.12586.

Santanello, J. A., Kumar, S. V., Peters-Lidard, C. D., Harrison, K., and Zhou, S. (2013). Impact of Land Model Calibration on Coupled Land-Atmosphere Prediction. *Journal of Hydrometeorology*, 14(5):1373–1400.doi: 10.1175/JHM-D-12-0127.1.

Sarmiento, D. P., Davis, K. J., Deng, A., Lauvaux, T., Brewer, A., and Hardesty, M. (2017). A comprehensive assessment of land surface-atmosphere interactions in a WRF/Urban modeling system for Indianapolis, IN. *Elem Sci Anth*, 5.doi: 10.1525/elementa.132.

Schaake, J. C., Koren, V. I., Duan, Q.-Y., Mitchell, K., and Chen, F. (1996). Simple water balance model for estimating runoff at different spatial and temporal scales. *Journal of Geophysical Research*, 101(D3):7461–7475.doi: 10.1029/95JD02892.

Schär, C., Lüthi, D., Beyerle, U., and Heise, E. (1999). The soil-precipitation feedback: A process study with a regional climate model. *Journal of Climate*, 12(2-3):722–741.doi: 10.1175/1520-0442(1999)012<0722:TSPFAP>2.0.CO;2.

Senatore, A., Mendicino, G., Gochis, D. J., Yu, W., Yates, D. N., and Kunstmann, H. (2015). Fully coupled atmosphere-hydrology simulations for the central Mediterranean: Impact of enhanced hydrological parameterization for short and long time scales. *Journal of Advances in Modeling Earth Systems*, 7(4):1693–1715.doi: 10.1002/2015MS000510.

Seneviratne, S. I., Corti, T., Davin, E. L., Hirschi, M., Jaeger, E. B., Lehner, I., Orlowsky, B., and Teuling, A. J. (2010). Investigating soil moisture-climate interactions in a changing climate: A review. *Earth-Science Reviews*, 99(3-4):125–161.doi: 10.1016/j.earscirev.2010.02.004.

Shin, H. H. and Dudhia, J. (2016). Evaluation of PBL Parameterizations in WRF at Subkilometer Grid Spacings: Turbulence Statistics in the Dry Convective Boundary Layer. *Monthly Weather Review*, 144(3):1161–1177.doi: 10.1175/MWR-D-15-0208.1.

Shrestha, P., Sulis, M., Masbou, M., Kollet, S., and Simmer, C. (2014). A Scale-Consistent Terrestrial Systems Modeling Platform Based on COSMO, CLM, and ParFlow. *Monthly Weather Review*, 142(9):3466–3483.doi: 10.1175/MWR-D-14-00029.1.

Skamarock, W. C. and Klemp, J. B. (2008). A time-split nonhydrostatic atmospheric model for weather research and forecasting applications. *Journal of Computational Physics*, 227(7):3465–3485.doi: 10.1016/j.jcp.2007.01.037.

Skamarock, W. C., Klemp, J. B., Dudhia, J., Gill, D. O., Barker, D. M., Duda, M. G., Huang, X. Y., Wang, W., and Powers, J. G. (2008). A description of the advanced research WRF Version 3, NCAR technical note. *National Center for Atmospheric Research, Boulder, Colorado, USA*.doi: 10.5065/D68S4MVH.

Smirnova, T. G., Brown, J. M., Benjamin, S. G., and Kenyon, J. S. (2016). Modifications to the Rapid Update Cycle Land Surface Model (RUC LSM) Available in the Weather Research and Forecasting (WRF) Model. *Monthly Weather Review*, 144(5):1851–1865.doi: 10.1175/MWR-D-15-0198.1.

Sodemann, H., Wernli, H., and Schwierz, C. (2009). Sources of water vapour contributing to the Elbe flood in August 2002-A tagging study in a mesoscale model. *Quarterly Journal of the Royal Meteorological Society*, 135(638):205–223.doi: 10.1002/qj.374.

Srinivas, C. V., Venkatesan, R., and Bagavath Singh, A. (2007). Sensitivity of mesoscale simulations of land-sea breeze to boundary layer turbulence parameterization. *Atmospheric Environment*.doi: 10.1016/j.atmosenv.2006.11.027.

Stoy, P. C., Mauder, M., Foken, T., Marcolla, B., Boegh, E., Ibrom, A., Arain, M. A., Arneth, A., Aurela, M., Bernhofer, C., Cescatti, A., Dellwik, E., Duce, P., Gianelle, D., van Gorsel, E., Kiely, G., Knohl, A., Margolis, H., McCaughey, H., Merbold, L., Montagnani, L., Papale, D., Reichstein, M., Saunders, M., Serrano-Ortiz, P., Sottocornola, M., Spano, D., Vaccari, F., and Varlagin, A. (2013). A data-driven analysis of energy balance closure across FLUXNET research sites: The role of

landscape scale heterogeneity. *Agricultural and Forest Meteorology*, 171-172:137–152.doi: 10.1016/j.agrformet.2012.11.004.

Sun, X., Holmes, H. A., Osibanjo, O. O., Sun, Y., and Ivey, C. E. (2017). Evaluation of surface fluxes in the WRF model: Case study for farmland in rolling terrain. *Atmosphere*, 8(10):1–23.doi: 10.3390/atmos8100197.

Trenberth, K. E. (1999). Atmospheric moisture recycling: Role of advection and local evaporation. *Journal of Climate*, 12(5 II):1368–1381.doi: 10.1175/1520-0442(1999)012<1368:AMRROA>2.0.CO;2.

Twine, T., Kustas, W., Norman, J., Cook, D., Houser, P., Meyers, T., Prueger, J., Starks, P., and Wesely, M. (2000). Correcting eddy-covariance flux underestimates over a grassland. *Agricultural and Forest Meteorology*, 103(3):279–300.doi: 10.1016/S0168-1923(00)00123-4.

Van Der Ent, R. J. and Savenije, H. H. G. (2011). Length and time scales of atmospheric moisture recycling. *Atmospheric Chemistry and Physics*, 11(5):1853–1863.doi: 10.5194/acp-11-1853-2011.

Wagner, S., Fersch, B., Yuan, F., Yu, Z., and Kunstmann, H. (2016). Fully coupled atmospheric-hydrological modeling at regional and long-term scales: Development, application, and analysis of WRF-HMS. *Water Resources Research*, 52(4):3187–3211.doi: 10.1002/2015WR018185.

Wang, J., Feng, J., and Yan, Z. (2018a). Impact of Extensive Urbanization on Summertime Rainfall in the Beijing Region and the Role of Local Precipitation Recycling. *Journal of Geophysical Research: Atmospheres*, 123(7):3323–3340.doi: 10.1002/2017JD027725.

Wang, K., Jiang, H., and Zhao, H. (2005). Atmospheric water vapor transport from westerly and monsoon over the Northwest China. *Advances in Water Science*, 16(3):432–438.

Wang, X., Pang, G., Yang, M., Wan, G., and Liu, Z. (2018b). Precipitation changes in the Qilian Mountains associated with the shifts of regional atmospheric water vapour during 1960-2014. *International Journal of Climatology*, 38(12):4355–4368.doi: 10.1002/joc.5673.

Wang, Y., Yang, H., Yang, D., Qin, Y., Gao, B., and Cong, Z. (2017). Spatial Interpolation of Daily Precipitation in a High Mountainous Watershed Based on Gauge

Observations and a Regional Climate Model Simulation. *Journal of Hydrometeorology*, 18(3):845–862.doi: 10.1175/JHM-D-16-0089.1.

Wei, J., Knoche, H. R., and Kunstmann, H. (2015). Contribution of transpiration and evaporation to precipitation: An ET-Tagging study for the Poyang Lake region in Southeast China. *Journal of Geophysical Research: Atmospheres*, 120(14):6845–6864.doi: 10.1002/2014JD022975.

Wei, J., Su, H., and Yang, Z. L. (2016). Impact of moisture flux convergence and soil moisture on precipitation: a case study for the southern United States with implications for the globe. *Climate Dynamics*, 46(1-2):467–481.doi: 10.1007/s00382-015-2593-2.

Weisman, M. L., Skamarock, W. C., and Klemp, J. B. (1997). The Resolution Dependence of Explicitly Modeled Convective Systems. *Monthly Weather Review*, 125(4):527–548.doi: 10.1175/1520-0493(1997)125<0527:TRDOEM>2.0.CO;2.

Wen, X., Lu, S., and Jin, J. (2012). Integrating Remote Sensing Data with WRF for Improved Simulations of Oasis Effects on Local Weather Processes over an Arid Region in Northwestern China. *Journal of Hydrometeorology*, 13(2):573–587.doi: 10.1175/JHM-D-10-05001.1.

Wigmosta, M. S. and Lettenmaier, D. P. (1999). A comparison of simplified methods for routing topographically driven subsurface flow. *Water Resources Research*, 35(1):255–264.doi: 10.1029/1998WR900017.

Xia, Y., Mitchell, K., Ek, M., Cosgrove, B., Sheffield, J., Luo, L., Alonge, C., Wei, H., Meng, J., Livneh, B., Duan, Q., and Lohmann, D. (2012a). Continental-scale water and energy flux analysis and validation for North American Land Data Assimilation System project phase 2 (NLDAS-2): 2. Validation of model-simulated streamflow. *Journal of Geophysical Research*, 117:D03110.doi: 10.1029/2011JD016051.

Xia, Y., Mitchell, K., Ek, M., Sheffield, J., Cosgrove, B., Wood, E., Luo, L., Alonge, C., Wei, H., Meng, J., Livneh, B., Lettenmaier, D., Koren, V., Duan, Q., Mo, K., Fan, Y., and Mocko, D. (2012b). Continental-scale water and energy flux analysis and validation for the North American Land Data Assimilation System project phase 2 (NLDAS-2): 1. Intercomparison and application of model products. *Journal of Geophysical Research*, 117:D03109.doi: 10.1029/2011JD016048.

Xiang, T., Vivoni, E. R., and Gochis, D. J. (2018). Influence of initial soil moisture and vegetation conditions on monsoon precipitation events in northwest México. *Atmósfera*, 31(1):25–45.doi: 10.20937/ATM.2018.31.01.03.

Xiang, T., Vivoni, E. R., Gochis, D. J., and Mascaro, G. (2017). On the diurnal cycle of surface energy fluxes in the North American monsoon region using the WRF-Hydro modeling system. *Journal of Geophysical Research: Atmospheres*, 122(17):9024–9049.doi: 10.1002/2017JD026472.

Xie, B., Fung, J. C. H., Chan, A., and Lau, A. (2012). Evaluation of nonlocal and local planetary boundary layer schemes in the WRF model. *Journal of Geophysical Research: Atmospheres*, 117(D12):n/a–n/a.doi: 10.1029/2011JD017080.

Xie, Z., Liu, S., Zeng, Y., Gao, J., Qin, P., Jia, B., Xie, J., Liu, B., Li, R., Wang, Y., and Wang, L. (2018). A High-Resolution Land Model With Groundwater Lateral Flow, Water Use, and Soil Freeze-Thaw Front Dynamics and its Applications in an Endorheic Basin. *Journal of Geophysical Research: Atmospheres*, 123(14):7204–7222.doi: 10.1029/2018JD028369.

Xiong, Z. and Yan, X. D. (2013). Building a high-resolution regional climate model for the Heihe River Basin and simulating precipitation over this region. *Chinese Science Bulletin*, 58(36):4670–4678.doi: 10.1007/s11434-013-5971-3.

Xue, M., Droegemeier, K. K., and Wong, V. (2000). The Advanced Regional Prediction System (ARPS) - A multi-scale nonhydrostatic atmospheric simulation and prediction model. Part I: Model dynamics and verification. *Meteorology and Atmospheric Physics*, 75(3-4):161–193.doi: 10.1007/s007030070003.

Yang, B., Zhang, Y., and Qian, Y. (2012). Simulation of urban climate with high-resolution WRF model: A case study in Nanjing, China. *Asia-Pacific Journal of Atmospheric Sciences*, 48(3):227–241.doi: 10.1007/s13143-012-0023-5.

Yang, D., Gao, B., Jiao, Y., Lei, H., Zhang, Y., Yang, H., and Cong, Z. (2015). A distributed scheme developed for eco-hydrological modeling in the upper Heihe River. *Science China Earth Sciences*, 58(1):36–45.doi: 10.1007/s11430-014-5029-7.

Yang, K., He, J., Tang, W., Qin, J., and Cheng, C. C. (2010). On downward shortwave and longwave radiations over high altitude regions: Observation and modeling in the Tibetan Plateau. *Agricultural and Forest Meteorology*, 150(1):38–46.doi: 10.1016/j.agrformet.2009.08.004.

Yang, X., Yong, B., Ren, L., Zhang, Y., and Long, D. (2017a). Multi-scale validation of GLEAM evapotranspiration products over China via ChinaFLUX ET measurements. *International Journal of Remote Sensing*, 38(20):5688–5709.doi: 10.1080/01431161.2017.1346400.

Yang, Y., Tang, J., Xiong, Z., and Dong, X. (2017b). Evaluation of High-Resolution Gridded Precipitation Data in Arid and Semiarid Regions: Heihe River Basin, Northwest China. *Journal of Hydrometeorology*, 18(12):3075–3101.doi: 10.1175/JHM-D-16-0252.1.

Yao, T., Masson-Delmotte, V., Gao, J., Yu, W., Yang, X., Risi, C., Sturm, C., Werner, M., Zhao, H., He, Y., Ren, W., Tian, L., Shi, C., and Hou, S. (2013). A review of climatic controls on δ 18 O in precipitation over the Tibetan Plateau: Observations and simulations. *Reviews of Geophysics*, 51(4):525–548.doi: 10.1002/rog.20023.

Yeh, P. J.-F. and Famiglietti, J. S. (2008). Regional terrestrial water storage change and evapotranspiration from terrestrial and atmospheric water balance computations. *Journal of Geophysical Research*, 113(D9):D09108.doi: 10.1029/2007JD009045.

Yu, L., Liu, T., Bu, K., Yang, J., Chang, L., and Zhang, S. (2017). Influence of snow cover changes on surface radiation and heat balance based on the WRF model. *Theoretical and Applied Climatology*, 130(1-2):205–215.doi: 10.1007/s00704-016-1856-0.

Yu, Z., Pollard, D., and Cheng, L. (2006). On continental-scale hydrologic simulations with a coupled hydrologic model. *Journal of Hydrology*, 331(1-2):110–124.doi: 10.1016/j.jhydrol.2006.05.021.

Yuan, X., Xie, Z., Zheng, J., Tian, X., and Yang, Z. (2008). Effects of water table dynamics on regional climate: A case study over east Asian monsoon area. *Journal of Geophysical Research*, 113(D21):D21112.doi: 10.1029/2008JD010180.

Yucel, I., Onen, A., Yilmaz, K., and Gochis, D. (2015). Calibration and evaluation of a flood forecasting system: Utility of numerical weather prediction model, data assimilation and satellite-based rainfall. *Journal of Hydrology*, 523:49–66.doi: 10.1016/j.jhydrol.2015.01.042.

Zhang, P. and Shao, M. (2015). Spatio-temporal variability of surface soil water content and its influencing factors in a desert area, China. *Hydrological Sciences Journal*, 60(1):96–110.doi: 10.1080/02626667.2013.875178.

Zhang, X., Xiong, Z., and Tang, Q. (2017). Modeled effects of irrigation on surface climate in the Heihe River Basin, Northwest China. *Journal of Geophysical Research: Atmospheres*, 122(15):7881–7895.doi: 10.1002/2017JD026732.

Zhang, X., Xiong, Z., Zheng, J., and Ge, Q. (2018). High-resolution precipitation data derived from dynamical downscaling using the WRF model for the Heihe River Basin, northwest China. *Theoretical and Applied Climatology*, 131(3-4):1249–1259.doi: 10.1007/s00704-017-2052-6.

Zhang, Z., Arnault, J., Wagner, S., Laux, P., and Kunstmann, H. (2019). Impact of Lateral Terrestrial Water Flow on Land-Atmosphere Interactions in the Heihe River Basin in China: Fully Coupled Modeling and Precipitation Recycling Analysis. *Journal of Geophysical Research: Atmospheres*, 124(15):8401–8423.doi: 10.1029/2018JD030174.

Zheng, D., Van Der Velde, R., Su, Z., Wen, J., and Wang, X. (2017). Assessment of Noah land surface model with various runoff parameterizations over a Tibetan river. *Journal of Geophysical Research: Atmospheres*, 122(3):1488–1504.doi: 10.1002/2016JD025572.

Zheng, D., Van der Velde, R., Su, Z., Wen, J., Wang, X., Booij, M. J., Hoekstra, A. Y., Lv, S., Zhang, Y., and Ek, M. B. (2016). Impacts of Noah model physics on catchment-scale runoff simulations. *Journal of Geophysical Research: Atmospheres*, 121(2):807–832.doi: 10.1002/2015JD023695.